Experimental Investigation of Enhanced Particle Transport due to Magnetic Perturbations on ASDEX Upgrade

Nils Leuthold

München 2020

Experimental Investigation of Enhanced Particle Transport due to Magnetic Perturbations on ASDEX Upgrade

Nils Leuthold

Dissertation
an der Fakultät der Physik
der Ludwig–Maximilians–Universität
München

vorgelegt von
Nils Leuthold
aus Münchberg

München, den 11.05.2020

Erstgutachter: Prof. Dr. Hartmut Zohm
Zweitgutachter: Prof. Dr. Harald Lesch
Tag der mündlichen Prüfung: 17.06.2020

Zusammenfassung

Am "Axisymmetric Divertor Experiment Upgrade" Tokamak in Garching wird an Kernfusion zum Zweck der Energiegewinnung geforscht. Nachdem in einem Tokamak Deuterium auf mehrere keV aufgeheizt wird, kann dieses aufgrund der einsetzenden Ionisierung als Plasma beschrieben werden. Magnetfelder werden dabei genutzt, um das Plasma in einer Vakuumkammer so einzuschließen, dass es thermisch isoliert ist gegenüber den Wänden der Kammer. Das Szenario, welches für zukünftige Kernkraftwerke basierend auf Kernfusion vorgesehen ist, ist die sogenannte H-Mode. In diesem Szenario wird eine Transportbarriere (ETB) am Rand des Plasmas geformt, was dort einen starken Druckgradienten zur Folge hat. Aufgrund dieses Druckgradienten in der ETB treten sogenannte "edge localized modes" (ELMs) während der H-Mode auf. Sie äußern sich als periodisch auftretende Instabilitäten, welche Energie und Teilchen aus dem Plasma heraus in Richtung der Gefäßwände schleudern. Man vermutet, dass die daraus resultierende Wärmelast auf den Wänden in zukünftigen Kernfusionsreaktoren zu untragbar hoher Erosion führt. Eine Methode zur Abschwächung und sogar Unterdrückung von ELMs ist die Überlagerung des einschließenden Magnetfelds mit einem radial gerichteten magnetischen Störfeld. Die Funktionsfähigkeit dieser Methode wurde bereits an mehreren Tokamaks demonstriert. Jedoch wurde dabei beobachtet, dass die Abschwächung oder Unterdrückung der ELMs von einer Erhöhung des auswärts gerichteten Transports von Teilchen und Energie — dem sogenannten "pump-out" Effekt — begleitet wird. Dies wiederum beeinflusst die Dichte und Temperatur des Plasmas. Die experimentelle Untersuchung des physikalischen Prozesses verantwortlich für den erhöhten Transport verursacht durch das magnetische Störfeld ist das Thema dieser Arbeit.

Um die Erhöhung des Transportes radial zu lokalisieren, wurde die Amplitude des magnetischen Störfeldes moduliert. Das Minimum der Phase der gemessenen Dichtemodulation liegt in der ETB, was darauf hinweist, dass der Ursprungsort des "pump-out" Effekts in der ETB liegt. Die Propagation der Dichtemodulation in Richtung des Plasmazentrums kann als Konsequenz der Dichtemodulation am Rand verstanden werden. Indem man magnetische Flussflächen, welche resonant zum angelegten Störfeld sind, in radiale Richtung verschiebt, wird deren Position relativ zum Ort verschwindenden radialen elektrischen Feldes E_r variiert. Ein messbarer Effekt aufgrund des Überlapps von resonanter Fläche und E_r Nulldurchgang auf die Stärke des "pump-out" Effekts wird nicht beobachtet. Die Beobachtung toroidal asymmetrischer breitbandiger Dichtefluktuationen und deren Verbindung zum Dichteprofil in der Randschicht sowie zu Dichtefluktuationen am Divertor lässt den Schluss zu, dass turbulenter Transport eine wichtige Rolle für den "pump-out" Effekt spielt. Messungen deuten an, dass die zugrunde liegende Instabilität in Ionenrichtung rotiert. Wenn die Amplitude des magnetischen Störfeldes einen kritischen Wert erreicht, dann kann eine quasi-kohärente Mode in der ETB während ELM Unterdrückung beobachtet werden. Wir beobachten, dass diese Mode den Teilchentransport erhöhen kann und dadurch eine mögliche Rolle im Aufrechterhalten der ELM Unterdrückung einnimmt.

Abstract

At the Axisymmetric Divertor Experiment Upgrade tokamak located in Garching, research on nuclear fusion as a source of energy is conducted. After heating deuterium up to several keV, it can be described as a plasma due to the consequent ionization. Magnetic fields are used to confine the plasma in a vacuum chamber such that the thermal isolation from the vessel wall is provided. The operational regime foreseen for future fusion power plants is the H-mode. In this regime, an edge transport barrier (ETB) is formed, which gives rise to a strong pressure gradient. During the H-mode, the so-called edge localized modes (ELMs) are present as a consequence of the pressure gradient in the ETB. ELMs manifest themselves as periodic bursts of particles and energy expelled from the confined plasma onto the plasma facing components. The resulting heat loads on plasma facing components are expected to lead to unacceptably high erosion in future tokamaks. One method for mitigating or completely suppressing ELMs is the superposition of the confining magnetic field with a small radial magnetic perturbation (MP) field. The viability of this method has been demonstrated on several of today's tokamaks. However, it is also observed that the mitigation and suppression of ELMs can be accompanied by an increase of the outward directed particle and energy transport influencing the plasma density and temperature dubbed the 'pump-out' effect. The experimental investigation of the physical mechanism behind the increased outward transport by magnetic perturbations is the topic of this thesis.

The radial localization of increased transport is investigated during a plasma discharge, in which the amplitude of the applied MP field was modulated. The phase of the measured electron density modulation at different radial coordinates indicates an origin of the increased transport in the ETB region, where a strong pressure gradient is present. The propagation of the density modulation towards the core of the plasma is found to be a mere reaction of the plasma to the modulated edge density. By moving magnetic surfaces resonant to the applied MP field in radial direction during a discharge, a possible influence of the relative position of resonant surfaces and the zero-crossing of the radial electric field is tested. During such scans, no dependence of the electron density is observed indicating that effects relating to this resonance do not dominate the 'pump-out' effect. Observations of an toroidal asymmetry in broadband density fluctuations and their connection to the density profile outside the plasma as well as to density fluctuations at the divertor indicate that turbulent transport causes radial particle transport. Measurements suggest that the underlying instability to be rotating in the ion direction. When a threshold in the MP field amplitude is reached, a quasi-coherent mode can be observed in the ETB region during ELM suppression. The experiments indicate that this mode increases radial particle transport further and, thereby, plays a possible role for the plasma to stay in the ELM suppression regime.

Contents

Chapter 1

Nuclear Fusion in a Tokamak

While the research on nuclear fusion dates back to the early 1940s, power plants based on nuclear fusion providing net electricity have not been realized yet. The physics principle behind nuclear fusion is the transition from light elements with a low binding energy per nucleon to a heavier element with higher binding energy per nucleon. The binding energy as shown in figure 1.1 is the missing energy of a nucleus as compared to the sum of the rest energies of its protons and neutrons. The fusion of particles with a lower mass number than iron releases the difference in binding energies. In the case of nuclear fusion in the laboratory, the most prominent reactions use deuterium and tritium as their fuel, which are both isotopes of hydrogen, and produce helium as well as neutrons.

$$ {}^{2}_{1}\mathrm{D} + {}^{2}_{1}\mathrm{D} \longrightarrow {}^{3}_{2}\mathrm{He}\ (0.82\,\mathrm{MeV}) + {}^{1}_{0}\mathrm{n}\ (2.45\,\mathrm{MeV}) $$

$$ {}^{2}_{1}\mathrm{D} + {}^{3}_{1}\mathrm{T} \longrightarrow {}^{4}_{2}\mathrm{He}\ (3.5\,\mathrm{MeV}) + {}^{1}_{0}\mathrm{n}\ (14.1\,\mathrm{MeV}) $$

While the natural occurrence of the isotope deuterium is 0.015 % and it can be extracted out of the sea water, tritium is radioactive with a half-life of 12.3 years and, hence, does practically not exist in nature. However, it can be produced by reactions of lithium with neutrons (called tritium breeding).

$$ {}^{6}_{3}\mathrm{Li} + {}^{1}_{0}\mathrm{n} \longrightarrow {}^{4}_{2}\mathrm{He} + {}^{3}_{1}\mathrm{T} $$

Despite the need to breed tritium and the downside of tritium being radioactive, D-T reactions are the foreseen method for energy production in future fusion reactor. The first reason is the significantly higher energy yield as compared to the D-D reaction. This results from the larger discrepancy of binding energy between the educts and products in the case of the D-T reaction as compared to the D-D reaction. The released energy is distributed between the helium and neutron according to the conservation of energy and momentum and is provided in the form of kinetic energy. The second reason to prefer D-T reactions over D-D reactions is the higher fusion cross-section at lower temperatures (see figure 1.2). Still, very high temperatures in the range of keV are necessary. For

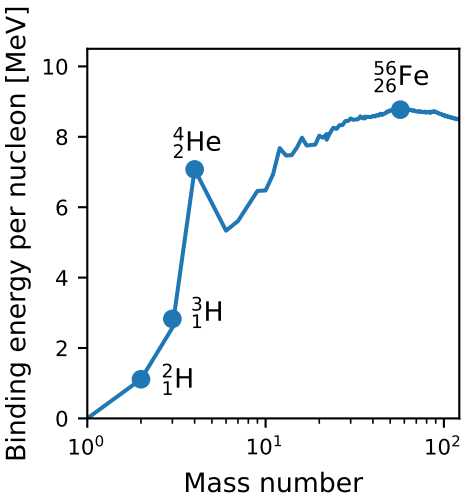

Figure 1.1: Binding energy per nucleon as a function of the mass number of all stables elements up to a mass number of 50 and the unstable tritium $^{3}_{1}$H.

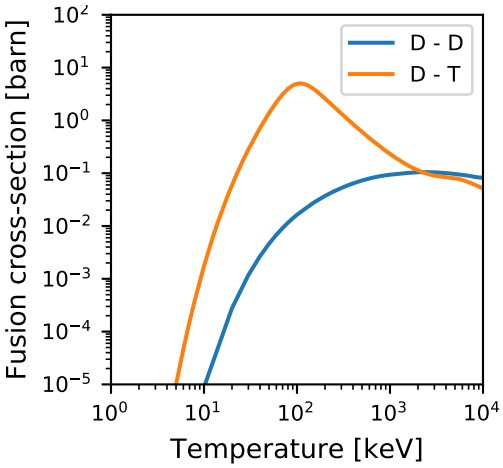

Figure 1.2: Fusion cross-section of the deuterium-deuterium (D-D) and deuterium-tritium (D-T) fusion reactions as a function of the temperature of the educt species, assuming their velocities have a Maxwellian distribution. Data is taken from [1].

comparison, 1 eV corresponds to approximately 11 606.7 K. The necessity of such a high temperature leads to problems with the confinement of the fuel. Not only will the fuel cool down when it is in contact with the wall of its confinement system, but it will also erode the wall. However, one can take advantage of the fact that deuterium and hydrogen at this temperature are in the state of a plasma and, therefore, can be confined in magnetic fields. In a magnetically confined plasma, the neutrons produced by fusion reactions can escape, while the charged alpha particles are confined in the plasma. Consequently, the neutrons can be used to generate steam and produce energy, while the helium heats up the plasma by transferring its kinetic energy to the plasma by collisions. When the heating power by the helium ash of the fusion reaction is sufficiently high to maintain the fusion reaction without external heating, it is referred to as ignition. The condition for an ignited plasma was given by Lawson [2]. It defines a minimum of the product of electron density n_e and energy confinement time τ_E as a function of temperature necessary for ignition as derived from the balance of the heating power created by the fusion reactions and the power loss by bremsstrahlung radiation as well as heat conduction and convection. This temperature dependent threshold is shown in figure 1.3 for D-T and D-D fusion reactions. The Lawson criterion includes the fusion cross-section and emphasizes again the advantage of D-T over D-D due to the two orders of magnitude lower $n_e\tau_E$ needed for ignition. For D-T, the minimum of $n_e\tau_E$ is in the temperature range of 18 to 35 keV or roughly 200 to 400 million Kelvin. Taking into consideration the dilution effects due to the helium ash and depending on its confinement, the operational temperature of a tokamak is at around 10 to 20 keV.

Since the density achievable in a tokamak has an empirical upper limit [3, 4], the energy confinement time has to be maximized. The energy confinement time scales with

the magnetic field in a tokamak and the size of the machine [6]. Scaling laws for the fusion power [7, 8] open up two different routes for future fusion power plants: towards stronger magnetic field or larger size of the machine. However, the strength of the magnetic fields are strongly limited by the state-of-art magnet technology. Consequently, the international fusion reactor project ITER [9, 10] is designed following the route towards larger size and its goal is to prove the feasibility of nuclear fusion as a source of economic energy.

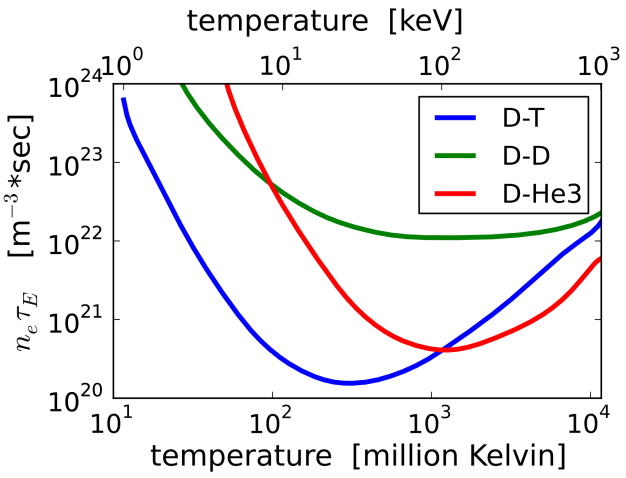

Figure 1.3: Lawson criterion: lower threshold of the product of electron density n_e and energy confinement time τ_E as a function of temperature and fusion reaction necessary for ignition. Taken from [5].

1.1 The Divertor Tokamak

The tokamak (Russian abbreviation for 'toroidal chamber with magnetic coils') is a suitable design for magnetic confinement and was developed in the 1950s in the Soviet Union. The illustration in figure 1.4 shows a schematic arrangement of the tokamak. Since the device is symmetric in toroidal direction, often a cylindrical coordinate system (R, ϕ, z) is used (see figure 1.5). Creating the magnetic field in a toroidal configuration (a torus) allows for magnetic field lines which do not end on a wall, but are closed in themselves. Here, external toroidal field coils (blue) create a magnetic field in toroidal direction B_ϕ (blue arrow), which is proportional to R^{-1}. Hence, the toroidal magnetic field is stronger on the inner side of the device than on the outer side and one refers to them as the High Field Side (HFS) and Low Field Side (LFS), respectively. In a purely toroidal magnetic field, the curvature, ∇B and ExB drifts lead to a fast movement of the plasma towards the vessel wall. This effect can be strongly reduced by introducing a magnetic field component in poloidal direction (three green arrows). This poloidal field component is not generated by external coils, but by a toroidal current in the plasma (single green arrow). In order to drive this current, a loop voltage is induced in the plasma by a solenoid placed in the central gap of the vessel (green coils). This inductive current drive has the disadvantage

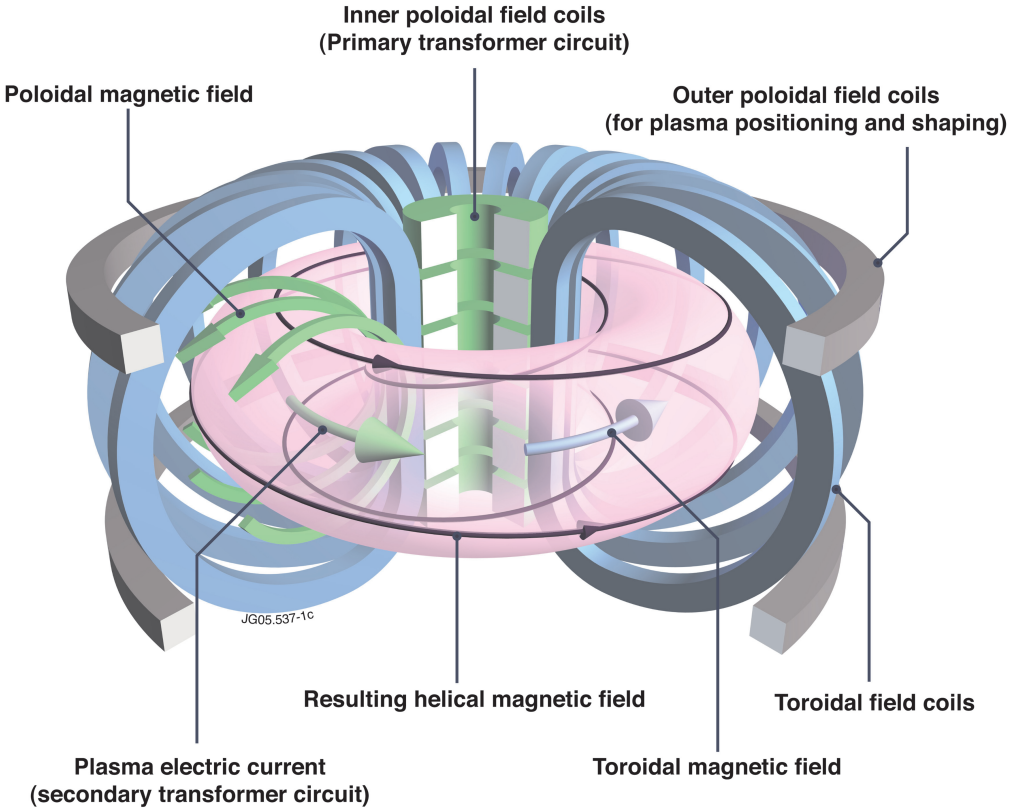

Figure 1.4: Illustration of the main magnetic field coils of a tokamak and the magnetic field they produce. Taken from [11].

that in order to maintain the loop voltage necessary for a constant plasma current, also a time-varying magnetic flux $\frac{d\Psi}{dt}$ has to be maintained, which implies an increasing or decreasing current in the solenoid. Since this is only possible for a finite time, a tokamak with inductive current drive can just be run in pulsed operation.

In the superposition of toroidal and poloidal fields, the magnetic field lines are helically wound and span nested surfaces These are surfaces on which the poloidal $\Psi = \int_{S_{pol}} \boldsymbol{B} d\boldsymbol{S}$ and toroidal $\Phi = \int_{S_{tor}} \boldsymbol{B} d\boldsymbol{S}$ magnetic fluxes are constant. They are defined as the magnetic flux through a surface S with a normal vector in poloidal and toroidal direction, respectively. The helicity of a flux surface can be described by the safety factor q. It is defined as the number of toroidal transits per poloidal transit of a magnetic field line on a certain surface and can be described as $q = \frac{d\Phi}{d\Psi}$.

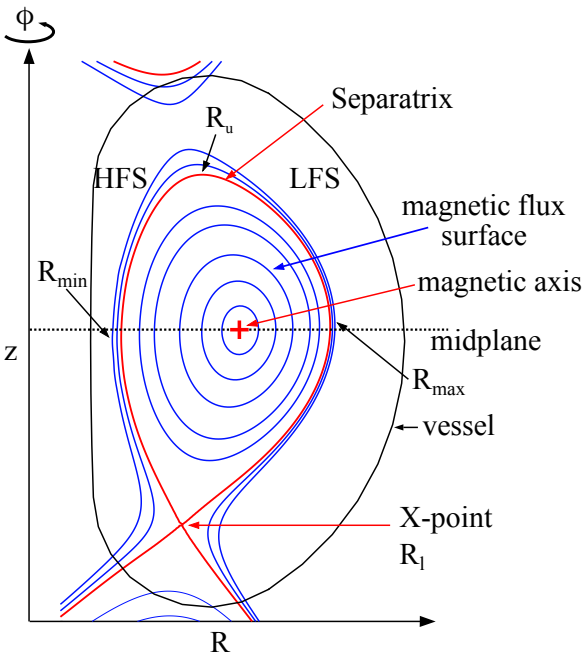

Figure 1.5: Poloidal cross-section of the magnetic field configuration of a tokamak.

Figure 1.5 shows the cross-section through such magnetic flux surfaces in a divertor configuration. The magnetic axis is defined as the point where the magnetic flux surfaces converge to a single line, which means that there the poloidal magnetic field is vanishing. The horizontal plane intersecting with the magnetic axis is called the midplane. In this divertor configuration, additional magnetic field coils are used to create the so-called X-line (X-point in the poloidal cross-section), on which the total poloidal magnetic field is null. A configuration in which the X-line is in front of the lower divertor at the bottom of the vessel is, hence, called a lower-single-null (LSN) configuration. The surface which includes the X-point is called the last closed flux surface (LCFS), which separates the confined region with closed flux surfaces from the so-called scrape-off layer (SOL) with open surfaces. In a divertor configuration, the LCFS is also a separatrix, which separates the distinct topological regions of the confined main plasma, open field lines of the SOL, and the so-called 'private flux region' around the divertor coil. In the scrape-off layer, the magnetic field lines end on a wall component, the divertor plates. These plates serve as a dump for particle and energy losses. The points where the separatrix hits the divertor plates are referred to as the strike points. The region below the X-point, just between the strike points on the inner and outer divertor is called the private flux region. The major radius R and minor radius a of a tokamak are defined as $R = {}^{(R_{max}+R_{min})}/_{2}$ and $a = {}^{(R_{max}-R_{min})}/_{2}$. One important shape parameter in this thesis is the plasma triangularity δ, which is the mean of the upper triangularity δ_u and lower triangularity δ_l defined as $\delta_u = {}^{(R-R_u)}/_{a}$ and $\delta_l = {}^{(R-R_l)}/_{a}$. Here, the quantities R_{min} and R_{max} refer to points on the

LCFS at which the radial coordinate is minimized or maximized, respectively. R_u and R_l refer to the radial coordinates of the highest and lowest points on the LCFS, respectively.

Particles in the magnetic field gyrate around the magnetic field lines. The stationary mass flow velocity $\boldsymbol{u}$ on a flux surface can be described by two components with respect to the magnetic field lines:

1. **Parallel** to the magnetic field lines, plasma can stream freely with a velocity $\boldsymbol{u}_\parallel$
2. **Perpendicular** to the magnetic field lines, the plasma ion and electron fluids experience a drift with a velocity of $\boldsymbol{u}_\perp = \frac{\boldsymbol{E}\times\boldsymbol{B}}{B^2} - \frac{\boldsymbol{\nabla} p_\mathrm{j}\times\boldsymbol{B}}{q_\mathrm{j} n_\mathrm{j} B^2}$, which is composed by the ExB and diamagnetic drifts with the radial electric field $\boldsymbol{E}$, the pressure radial pressure gradient $\boldsymbol{\nabla} p$, the charge q_j and density n_j of the particle species j. Since the ExB drift direction and velocity is the same for ions and electrons, it can be considered as a background flow.

From the force balance $\boldsymbol{\nabla} p = \boldsymbol{j}\times\boldsymbol{B}$ between the plasma pressure and the magnetic pressure it follows inherently that the plasma pressure p is constant on a magnetic flux surface. This can be seen if both sides of the force balance equation are multiplied by the magnetic field $\boldsymbol{B}$, then it follows $\boldsymbol{\nabla} p \cdot \boldsymbol{B} = 0$. Furthermore, due to the significantly higher particle and heat transport along magnetic field lines as compared to perpendicular to them, also the density n and temperature T are usually assumed to be constant on the magnetic flux surfaces. Consequently, it is useful to define a flux-surface coordinate in order to map measurements taken from diagnostics located at different positions in the lab frame onto a 1-dimensional radial grid. It also allows for mapping of the measurements on the radial real space coordinate R[m] at the midplane. Since the poloidal and toroidal flux, Ψ and Φ, are constant on a flux surface but vary across them, they can be used as radial coordinates. However, due to the integral in their definitions, an arbitrary constant can be added to each. Hence, it is common to define new coordinates based on either the poloidal or toroidal flux and normalize them in such a way that the resulting coordinate is 0 on the magnetic axis and 1 at the separatrix. Since this thesis focuses on the edge of the plasma and the toroidal flux is constant outside the separatrix, the normalized poloidal flux radius ρ_pol defined as

$$\rho_\mathrm{pol} = \sqrt{\frac{\Psi - \Psi_\mathrm{axis}}{\Psi_\mathrm{sep} - \Psi_\mathrm{axis}}} \tag{1.1}$$

with subscripts 'axis' referring to the corresponding value at the magnetic axis and 'sep' at the separatrix will be used.

Transport in a Tokamak

Particles, energy (or heat) and momentum are not perfectly confined in a tokamak. The confinement time, which is crucial for the fusion energy gain, depends on these losses caused by radial transport across the magnetic flux surfaces [12, 13]. In an axisymmetric toroidal configuration with rotational transform (such as the tokamak), particle orbits are

confined as long as there are no collisions. However, collisions between particles lead to diffusive transport, which — in combination with the tokamak geometry — is referred to as neoclassical transport. Furthermore, turbulent (or anomalous) transport arises in a tokamak due to small-scale fluctuations of plasma quantities such as density, temperature, magnetic field and potential. Their spatial scale is usually described by their wavelength in perpendicular direction times the effective ion gyro-radius $k_\perp \rho_\mathrm{s}$ with $\rho_\mathrm{s} = \sqrt{m_\mathrm{i} T_\mathrm{e}}/eB$ and is in the order of approximately 0.1 to 1. For the case of density fluctuations, the frequency of such fluctuations is in the kHz range and their amplitude can get as large as a few percent of its corresponding mean background value. While fluctuations are observed in the whole plasma, their amplitude tends to increase towards the plasma edge. Assuming an electro-static case, i. e. ignoring electro-magnetic effects, the radial displacement of an electron is defined by the fluctuation of the radial component of the ExB velocity $\tilde{v}_\mathrm{ExB,r}$, i. e. by fluctuations of the potential. The electro-static particle flux associated with the fluctuations of density and potential can be described as

$$< \Gamma >=< \tilde{n}\tilde{v}_\mathrm{ExB,r} > \tag{1.2}$$

with $<>$ being the averaging in time and space, and $< \tilde{n} >=< \tilde{v}_\mathrm{ExB,r} >= 0$. Hence, the occurrence of of net radial transport depends on the correlation between density and potential fluctuations.

In a simplified picture, turbulent eddies convect plasma over a radial distance L_c with a characteristic time of one pass around the eddy, t_c. Vortex flows that remain correlated in radius L_c for a time t_c will lead, according to a random walk picture, to diffusion with a diffusion coefficient of $D_\mathrm{turb} = L_\mathrm{c}^2/2t_\mathrm{c}$. The turbulent structures move poloidally along with the background ExB flow and maintain their structure. As proposed in various models [14, 15]., As illustrated in figure 1.6, sheared ExB flows can elongate turbulent eddies in poloidal direction or tear them apart (as illustrated in 1.6). Consequently, the radial correlation length of the turbulent eddies decreases and, thereby, turbulent transport is reduced. The turbulence itself develops in a plasma when micro-instabilities are growing to a point where non-linear effects start to play a role leading to a saturated quasi-stationary state.

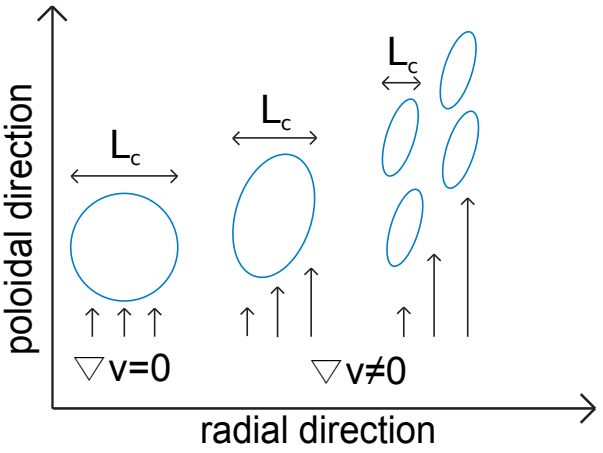

Figure 1.6: Illustration of a shear flow reducing the radial correlation length of turbulent structures.

1.2 The H-mode and Edge-Localized Modes (ELMs)

In the early 1980s, it was discovered at the tokamak ASDEX located in Garching, that with the injection of a sufficient amount of heating power, a sudden transition from a low-confinement (L-mode) to high-confinement (H-mode) regime takes place [16, 17]. The terminology comes from the fact that the energy confinement time increases in the H-mode approximately by a factor of 2 as compared to the L-mode. Therefore, the H-mode is the foreseen operational regime of a future fusion reactor. This confinement increase originates from a reduction of turbulent transport in a narrow region just inside the separatrix which is consequently dubbed the 'edge transport barrier' (ETB). Consequently, during the transition from the L-mode to the H-mode regime, the pressure profile steepens up in the ETB region as it can be seen in figure 1.7. The ETB region is, therefore, often also referred to as the steep-gradient region. It appears as the logarithmic core profile is just lifted up by the turbulence suppression in the edge; hence, the ETB region is also referred to as the H-mode pedestal. In this thesis, the term pedestal top refers to the inner border of the pedestal, the pedestal foot to the outer border and the distance between them is the pedestal width. While the L- to H-mode transition is not fully understood yet, there is evidence that the turbulence is suppressed by sheared ExB flows and the associated radial electric field E_r [18, 19, 20, 21, 22, 23]. An illustration of the E_r profiles in L-mode and H-mode is given in figure 1.8. In both, L- and H-mode, the radial electric field has a minimum in negative direction near the separatrix in the confined region, the so-called E_r well. The depth of the well is its minimum value and the width of the well can be defined as the full width at half minimum in radial direction. In ASDEX Upgrade, the depth of the E_r well in L-mode is typically less negative then $-15\,\mathrm{kV/m}$ and in H-mode the well becomes deeper [24, 21]. Towards the core region, the radial electric field typically increases and the location where it changes its sign is called the E_r zero crossing or reversal point. The L-H transition is a

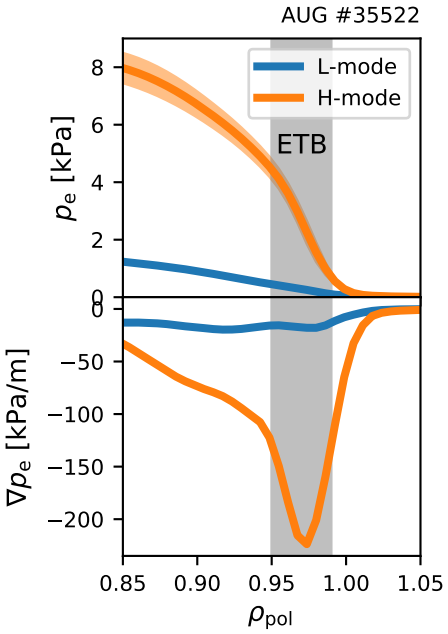

Figure 1.7: Comparison of the electron pressure (gradient) between L- and H-mode.

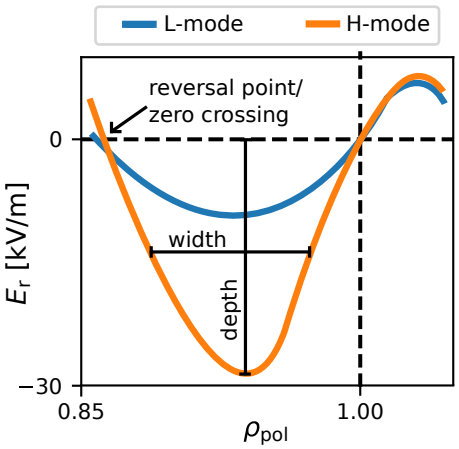

Figure 1.8: Illustration of the radial electric field in L-mode and H-mode.

self-organizing phenomenon, since the ensuing pressure gradients deepen the E_r well and sheared ExB flows further.

In the H-mode regime, where turbulent transport is suppressed in the ETB, a strong pressure gradient builds up, which in turn acts as a free source of energy which drives a magneto-hydrodynamic instability typically present in the H-mode: the edge-localized mode (ELM) [25, 26]. This instability expels particles and energy in a repetitive manner out of the plasma causing a transient reduction of density, temperature and stored energy (see figure 1.9). These particles and energy crossing the separatrix are then guided by the open field lines in the scrape-off layer of a divertor tokamak onto the divertor. There, ELMs can be detected e. g. by shunt current measurements in the outer divertor I_{div}, which are sensitive to the plasma temperature in front of the divertor tile. Due to their accompanying heat loads and repetitive nature, ELMs can be observed in this signal as sharp bursts occurring with a certain frequency and amplitude. After an ELM is triggered and the pedestal pressure drops, the pedestal pressure begins to recover again and at some point another ELM is triggered. Their repetition frequency is usually in the range of few Hz up to kHz. The largest type of ELMs in terms of expelled energy (up to about 35 % of the stored energy in ASDEX Upgrade) are the so-called Type-I ELMs. Today's most accepted model to describe the linear stability of Type-I ELMs is the peeling-ballooning model [27, 28, 29]. Figure 1.10 shows a schematic sketch illustrating this model. It is based on two instabilities: the ballooning instability/mode and the peeling instability/mode. The ballooning mode is driven by the pressure gradient and stabilized by the current density. In contrast, the peeling mode is driven by the current density and stabilized by the pressure gradient. In between the stability boundaries of the peeling and the ballooning mode is a gap of the stable region towards infinite current density and pressure gradient. This gap, however, is closed by coupling of the peeling and ballooning modes: an instability driven by both plasma current density and pressure gradient. It is thought to be responsible for the destabilization of Type-I ELMs.

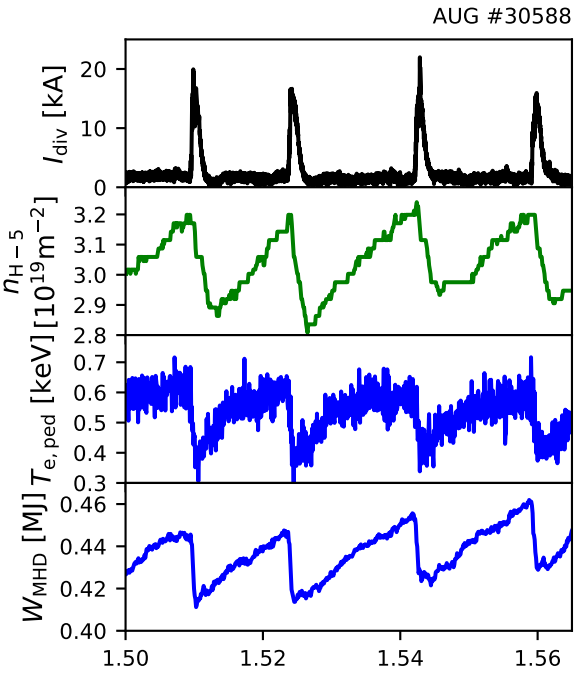

Figure 1.9: Time traces of the divertor shunt current I_{div}, the line-integrated electron density close to the pedestal top $n_{\mathrm{H-5}}$, the electron temperature close to the pedestal top and $T_{\mathrm{e,ped}}$ and the stored energy W_{MHD}.

While Type-I ELMs flush out impurities (such as the helium ash), the consequence of Type-I ELMs are large transient heat loads on the divertor plates. In present devices, these heat loads are not detrimental, but will be — according to proposed scalings [30, 31] — in

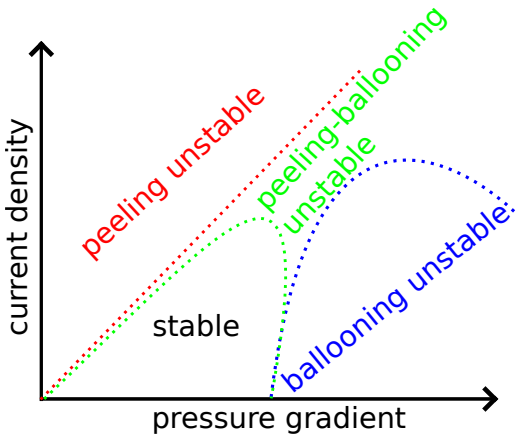

Figure 1.10: Schematic sketch of a linear peeling-ballooning stability diagram.

future fusion devices like ITER. Different H-mode regimes of small or naturally stabilized ELMs are have been identified [25], however, these regimes typically have lower confinement and are in need of another mechanism for flushing out impurities. Hence, it is important to discover and develop operating regimes with good confinement and impurity transport, while avoiding or at least mitigating ELMs. One method, which has been proven to mitigate and even suppress ELMs, while at the same time providing outward transport of impurities, is the application of radial magnetic perturbations fields [32, 33, 34, 35, 36, 37]. However, radial magnetic perturbation fields can also lead to an undesirable increase of outward particle and heat transport, thus reducing the confinement and performance of the plasma — the 'pump-out' effect [35, 38, 39]. ELM suppression by magnetic perturbations and the pump-out effect are investigated experimentally in this thesis.

1.3 Scope of this Thesis

In chapter 2 the ASDEX Upgrade tokamak as well as its magnetic perturbation coil system and relevant diagnostics are introduced. Therein, also the codes for solving the magnetic equilibrium of discharges performed in ASDEX Upgrade are briefly described. Chapter 3 gives a description of the different plasma scenarios used in this thesis and characterizes the pump-out effect in these scenarios. The goal of this thesis is to give further insight on the density pump-out effect and explore its underlying mechanisms. In specific, three well defined questions regarding the density pump-out effect will be answered in this thesis:

Chapter 4 In which radial region do the radial magnetic perturbations modify the particle transport?

Chapter 5 Does the exact position of rational surfaces at the pedestal top, which are resonant to the radial magnetic perturbation field, play a crucial role for the enhanced outward transport of particles during ELM mitigation?

Chapter 6 Are radial magnetic perturbations able to alter the turbulent transport in the region of the edge transport barrier during ELM suppression and can this lead to increased outward particle transport?

With the answers to these questions, this thesis is supposed to provide a firm base for further experimental studies as well as for theoretical investigations of the pump-out effect. Furthermore, a new hypothesis for the suppression of edge-localized modes is suggested, which is based on turbulent transport.

Chapter 2

The ASDEX Upgrade Tokamak

All the experimental work in this thesis has been executed at the Axially Symmetric Divertor Experiment Upgrade (ASDEX Upgrade or AUG), a divertor tokamak located at the Max-Planck-Institute for Plasma Physics in Garching, Germany. In the context of existing tokamaks and such in construction, AUG is seen as a middle-sized tokamak with its major radius R of about 1.65 m, its minor radius r of roughly 0.5 m and a plasma volume V of roughly 11 – 14 m-3 (dependent on the shape of the plasma). In contrast to many other fusion devices using carbon, the plasma facing components in AUG are either massive tungsten tiles or graphite tiles coated with a thin tungsten layer ($\sim$ 10 μm), which allows for a low impurity content in the plasma. Figure 2.1 illustrates the poloidal cross-section of AUG. A toroidal field B_ϕ of up to 3.1 T can be generated by a set of 16 copper field coils (green). With the copper solenoid (orange) used as a transformer in the center of AUG, a plasma current I_p of 0.4 – 1.6 MA can be driven. For the plasma discharges used in this thesis, the toroidal magnetic field is always directed clockwise as seen from above the torus, while the plasma current is in counter-clockwise direction. Another 12 copper field coils (magenta) are used to create a vertical magnetic field in order to control the shape and position of the plasma. A passive stabilization loop (PSL, yellow) is used to slow down the growth rate of vertical plasma instabilities. The divertor coils (cyan) are used to produce the poloidal field null (X-line) necessary for a divertor configuration. Since ASDEX Upgrade is not designed for the use of tritium, only deuterium discharges

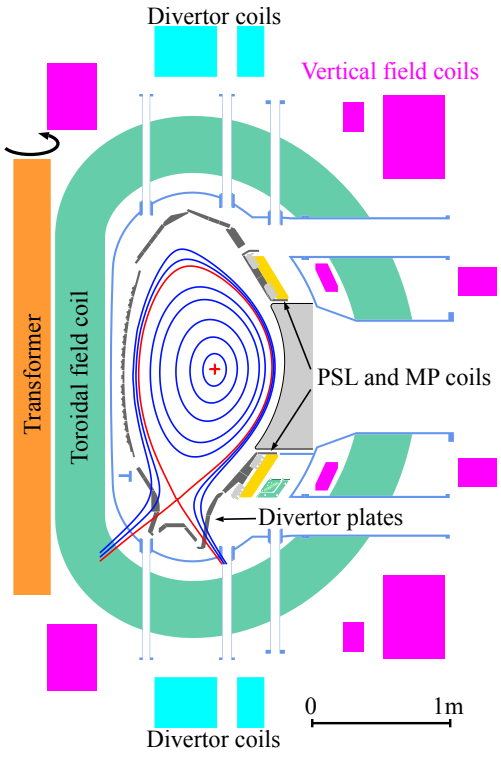

Figure 2.1: Poloidal cross-section of ASDEX Upgrade.

are investigated. In the following, the hash-tag ('#') is used to denote specific discharges performed in ASDEX Upgrade (e. g. #34548).

ASDEX Upgrade has been upgrated with a set of in-vessel magnetic perturbation coils [40, 41, 42], which are widely used for the investigation of the mitigation and suppression of edge-localized modes, as described in the following.

2.1 Magnetic Perturbation (MP) Coil System

The magnetic perturbation coil system of ASDEX Upgrade consists of 16 saddle coils. Eight coils are mounted above the midplane and eight below the midplane on the LFS (see rectangles in figure 2.2). Each coil is wound with five turns and the maximum current in these is limited by the Lorentz force acting on the conductor, produced by the tokamak toroidal and poloidal fields. For discharges with $B_\phi < 2\,\mathrm{T}$ and $I_\mathrm{p} \leq 0.8\,\mathrm{MA}$ the limit is 1.3 kA in each coil. Otherwise, the MP coil currents are limited to 1.0 kA. The coils create magnetic fields B_r mainly in the radial direction, pointing inward or outward depending on the polarity of the coil current. The maximum field at the plasma surface in front of each coil is approximately 10^{-3} of the toroidal magnetic field, or 2 – 3 mT. It decays fast in the radial direction. Depending on the plasma shape, the separatrix is approximately 10 – 30 cm away from the coil center. Each coil has its own power supply allowing for complex, dynamic perturbation patterns. The radial perturbation field leads to a corrugation of the plasma surface as indicated in figure 2.2 by the 3-dimensional color coded displacement.

2.1.1 MP Control Parameters

The only control parameters of the MP coils are the currents in each coil. However, depending on the pattern of the current across all 16 coils, a variety of the different MP fields can be produced. The resulting field is then described in terms of its toroidal mode number n, the differential phase angle $\Delta\phi$, spatial orientation in toroidal direction ϕ_0 and the effective MP coil current amplitude A_eff. The toroidal mode number n is the period of the pattern of the perturbation field in toroidal direction. With its eight coils in each row, the MP coil system at AUG allows for $n = 1, 2, 3$ or 4. In figure 2.2 the blue and red coils are powered with 1.3 kA in opposite directions. The grey coils are not powered. One can see that the pattern [1.3 kA, 0 kA, −1.3 kA, 0 kA] repeats two times in toroidal direction, i. e. $n = 2$. In this case, the maximum amplitude of the perturbation field is reached in front of each powered coil limited by the previously mentioned force limit. Nevertheless, an even higher amplitude can be reached by powering every grey coil in figure 2.2 with the same current as the coil to its left (or right). This way, the field amplitude of the two neighboring coils with equal polarity add up and the maximum field amplitude is reached in the middle between those two coils. This is illustrated in figure 2.3, where the current in each coil is plotted as a function of the toroidal angle of the coil center (blue dots) for the upper (top plot) and lower row of coils (bottom plot). The fit to the data (blue line) shows a maximum between two coils which is referred to as the effective MP coil current I_eff. The toroidal orientation ϕ_0 can be defined as the angle between the first maximum of the fit ϕ_max and the center of the first coil ϕ_Bu1 minus half the differential phase angle $\Delta\phi$. The differential phase angle $\Delta\phi$ is defined as the phase offset of the upper coil row with respect to the lower coil row. Note, that the angles are measured not as geometrical toroidal angles of the full torus, but as phase angles of the perturbation. The full toroidal circumference, therefore, corresponds to a phase angle of $2\pi n$. In the case of figure 2.3, the offset is +45 °

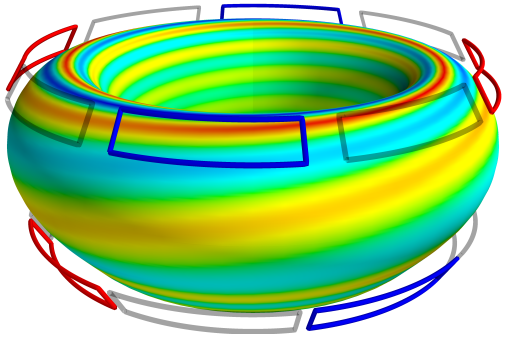

Figure 2.2: Illustration of the separatrix displacement due to a $n = 2$ perturbation field as calculated by VMEC. The color code shows the displacement and current direction of the surface and MP coils, respectively. The grey coils are not powered.

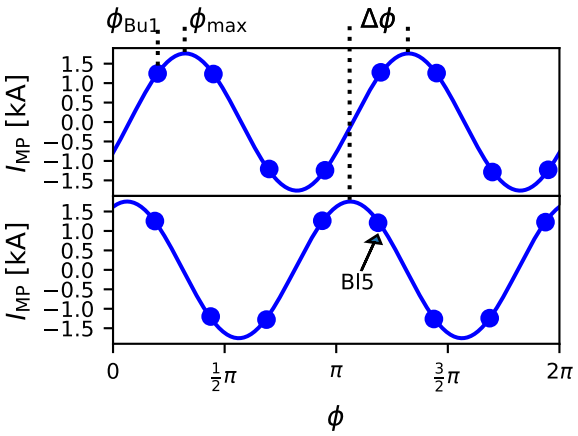

Figure 2.3: Current in the upper (top) and lower (bottom) MP coils as a function of the coils central toroidal angle (blue dots) as well as a sinusoidal fit. The coils in the upper and lower row of coils are dubbed *Bu1..8* and *Bl1..8*, respectively.

in the lab frame but $n \cdot +45\,^\circ = +90\,^\circ$ in the perturbation frame, i. e. $\Delta\phi = +90\,^\circ$. Here, ϕ_0 was set to zero. Since the requirement of the case with maximum possible perturbation field amplitude at $n = 2$ is an equivalent and maximum current in two neighboring coils each, this implies that ϕ_0 as well as $\Delta\phi$ in such a configuration have to be equal to the angle between two neighboring coils ($0.25\,\pi$). Due to the availability of eight coils in toroidal direction, only four possible toroidal orientations of such an $n = 2$ perturbation field with maximum amplitude exist for each one of the possible variants of $\Delta\phi$. Due to the finite number of coils in toroidal direction, spatial aliasing is not negligible. Its consequence is a leakage of power from the main component into side-bands, which reduces the effective MP coil current amplitude A_{eff} of the main component further.

2.1.2 Poloidal Mode Spectrum

Since there are just two rows of box shaped coils distributed over the whole poloidal circumference, the poloidal mode spectrum is rather broad, but can be modified by the differential phase angle $\Delta\phi$. The poloidal mode number spectrum for the perturbation presented in figure 2.3 with $\Delta\phi = +90\,^\circ$ is shown in the left plot of figure 2.4, while the right side shows the case of $\Delta\phi = -90\,^\circ$. In both cases, several m branches exist. The poloidal mode spectrum influences the resonance between the perturbation field structure and the magnetic field lines of the confining field, which is of particular importance. The external magnetic perturbation is in resonance with the confining magnetic field at a certain magnetic flux surface, if the component of the perturbation field aligned with the field lines of the flux surface $q = \frac{m}{n}$ is maximized. Taking the q profile of the magnetic equilibrium and the toroidal mode number $n = 2$ of the MP field, the rational surfaces $q = \frac{m}{n} = \frac{m}{2}$ are overlayed in figure 2.4 (white dots). In the case of $\Delta\phi = +90\,^\circ$, a local maximum in

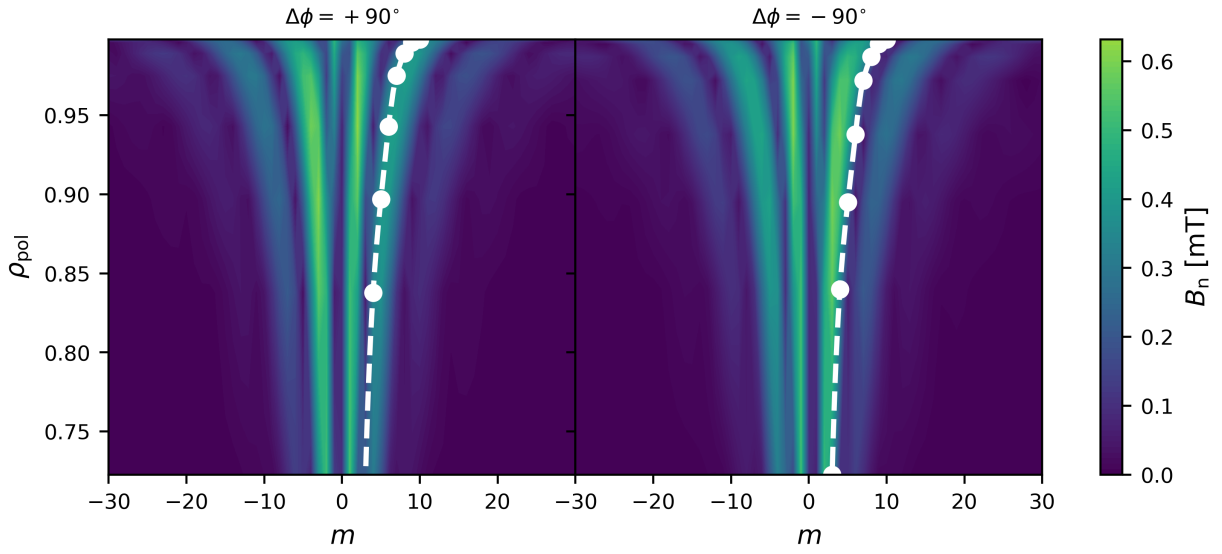

Figure 2.4: Poloidal mode spectrum of the MP coil pattern shown in figure 2.3 for different radial positions. The white dots indicate the rational surfaces, which can be resonant to the $n = 2$ perturbation field at the edge of the plasma.

the poloidal mode spectrum is well aligned with rational surfaces at the plasma edge, i. e. the magnetic perturbation is in resonance with the plasma edge. On the other hand, at $\Delta\phi = -90\,^\circ$ the rational surfaces are not intersecting a local maximum of the perturbation field, i. e. the magnetic perturbation is non-resonant at the edge. Arising resonant effects can be the creation of magnetic islands and a consequent ergodization of the very edge region due to the broad poloidal mode spectrum and steep safety factor profile at the edge. These effects might play a role in the suppression of edge-localized modes and the pump-out effect.

While figure 2.4 just represents the vacuum magnetic perturbation field, it was shown in [**?**] that the total perturbation field can exhibit the vacuum perturbation field significantly. Here, the total perturbation field is the sum of the external, vacuum perturbation field and the perturbation field by currents induced in the plasma a a response to the external perturbation. It was shown in [**?**] that ELM suppression at DIII-D was not found at differential phase angles corresponding to maximum vacuum pitch aligned components but at differential phase angles, which maximize the total pitch aligned components including the plasma response. A parametrization of $\Delta\phi$ with the safety factor and the normalized plasma beta as described in [43] was used in this thesis in order to calculate the differential phase angle necessary for getting the strongest pitch aligned component for each discharge. Albeit, it is not always worthwhile to set $\Delta\phi$ exactly at its optimum value for maximum mode amplitude as predicted by the parametrization. The reason is, that in order to fit $\Delta\phi$ some coils may have to be operated at reduced current due to the force limit of the coils.

2.1.3 Dynamic Patterns

If dynamic magnetic fields are created by the MP coils, mirror currents are induced in the passive stabilization loop (PSL), a large copper conductor on which the MP coils are mounted on (see yellow plates in figure 2.1). According to Lenz' Law, these mirror currents are induced such that their magnetic field counteracts the dynamic perturbation field. Consequently, the amplitude of the dynamic perturbation field is reduced and experiences a phase lag. Since these variations are not negligible, they have to be accounted for. Finite element calculations of AC vacuum fields at various frequencies in front of the upper and lower coils are interpolated in order to provide necessary information for calculating the effective currents in the coils. This calculation has been done for one observation point each for upper and lower MP coils, which is approximately located at the plasma surface of a typical ASDEX Upgrade plasma. The distance of the plasma to the MP coils (10 cm at the upper coils) is larger than the width of the skin current layer near the front of the PSL for ms time scales (< 1 cm) and the distance of MP coil conductor and PSL surface (2 cm). In a good approximation, we can calculate the effective vacuum field of coil conductor and PSL in the far field, i. e. consider the coil current and PSL current as lumped together. The sum of coil current and PSL current, therefore, defines an effective coil current that produces a transient vacuum field.

Already the process of just turning off the MP coils is a dynamic pattern by itself. In the upper plot of figure 2.5, the coil current in one of the MP coils is shown for the case of a normal turn-off of the perturbation field labeled as 'slow' (blue). This labeling comes from the fact that the effective $n = 2$ MP coil current amplitude vanishes not instantly after the turn-off, but decays over several 100 ms due to the PSL response (compare with PSL response in orange, to without PSL response in blue in the lower plot). However, a scheme can be applied to allow for a faster decay of the perturbation field (green). After the turn-off, the MP coils are powered with reversed polarity in order to compensate for the magnetic field due to the mirror currents in the PSL. This allows for a decay of the perturbation field in a few 10 ms instead of several 100 ms.

Furthermore, the coil system of AUG also allows for dynamic operations like $\Delta\phi$ scans and rigid rotations of the perturbation field around the torus. Figure 2.6 shows the toroidal orientation ϕ_0 and the effective $n = 2$ MP coil current amplitude of the perturbation field in a discharge, in which a static magnetic perturbation field was applied up until $t = 3$ s followed by a rigid rotation of the perturbation field toroidally around the torus. It includes calculations without (blue) and with (orange) the PSL response. Up until $t = 3$ s the perturbation field is static and, hence, no difference between both cases can be seen. At $t = 3$ s, the amplitude has to be reduced in order to allow for rigid rotation with a constant amplitude, because the force limit of each individual coil shall not be exceeded at any time during the rotation. After $t = 3$ s, the aforementioned phase lag becomes apparent in the plot of ϕ_0, and after several 100 ms the effective $n = 2$ MP coil current amplitude converges to a value below the case without the PSL response.

Such a rigid rotation of the perturbation field is used in this thesis in order to scan possible toroidal asymmetries located in the 3-dimensional surface corrugation of the

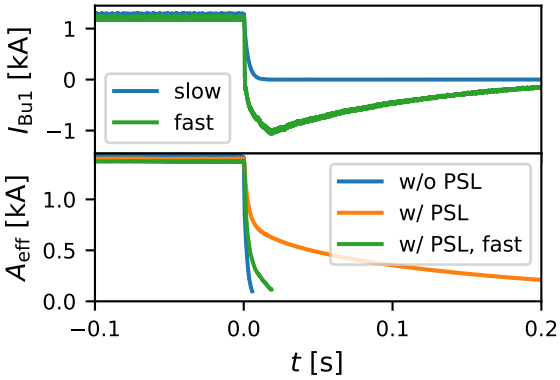

Figure 2.5: Top: current in one of the MP coils for the case of a slow (blue) and fast (green) turn-off. Bottom: effective $n = 2$ MP coil current amplitude for the slow turn-off without (blue) and with (orange) consideration of the PSL response. The case of a fast turn-off including the PSL response is shown in green.

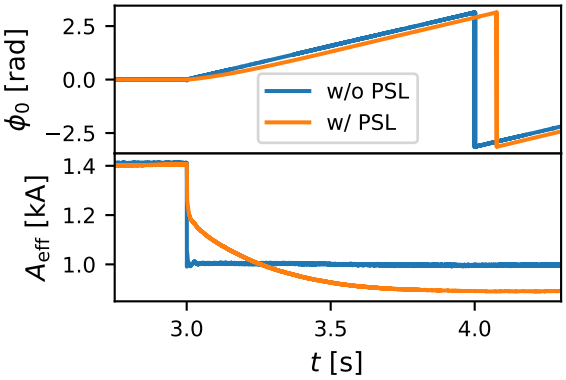

Figure 2.6: Toroidal orientation (top) and effective $n = 2$ MP coil current amplitude (bottom) of a perturbation without (blue) and with (orange) consideration of the PSL response.

plasma with diagnostics fixed in the lab frame. In the following, the amplitude of the perturbation field is always expressed in the effective current amplitude A_{eff} of the main component of the perturbation field including the PSL response.

2.2 Diagnostics

In this section, all important diagnostics are described which are used in this thesis to diagnose the plasma with a focus on the edge region. Their lines of sight are plotted in poloidal and toroidal views in figure 2.7. References are given for more detailed descriptions of each of the following diagnostics.

The reflection of electromagnetic waves at regions of vanishing refractive index N=c/v_ph=0 can be used to probe the plasma density.

2.2.1 Reflectometry

Reflectometry diagnostics [44, 45] are base on the reflection of electromagnetic waves at regions of vanishing refractive index and are used to probe the plasma density. The probing wave can be polarized in either O-mode ($E \parallel B_0$), in which case the cut-off occurs at the plasma frequency (electrostatic electron oscillation) which equals the angular probing frequency omega at a density of $n_{\mathrm{co}} = {\omega^2 m_{\mathrm{e}} \epsilon_0}/{e^2}$, or in X-mode ($E \perp B_0$). In the latter case, the probing frequency and density of the cut-off layer are related via $\omega_{\mathrm{U,L}} = \sqrt{{\omega_{\mathrm{c}}^2}/{4} + \omega_{\mathrm{p}}^2} \pm {\omega_{\mathrm{c}}}/{2}$ with the electron cyclotron frequency $\omega_{\mathrm{c}} = {eB}/{m_{\mathrm{e}}}$ and plasma frequency $\omega_{\mathrm{p}} = \sqrt{{n_{\mathrm{e}} e^2}/{m_{\mathrm{e}} \epsilon_0}}$. Hence, for the a probing wave in X-mode, two solutions exist and are dependent on the magnetic field B.

In this thesis, the conventional reflectometry is used for the observation of changes in the density fluctuations at the cut-off layer. The Doppler reflectometry is used for the measurement of the perpendicular electron velocity. In both cases, the density profile as measured by other diagnostics (Lithium Beam Spectroscopy and Thomson scattering) is used for the mapping of the reflectometry data.

Conventional Reflectometry

With the conventional reflectometry system, large-scale density fluctuations can be measured locally. The incident wave is injected perpendicular to the magnetic flux surfaces and the reflected wave is then analyzed.

ASDEX Upgrade is equipped with each 4 homodyne reflectometry bands in O-mode on the Low and High Field Side: K-band (17 – 25 GHz), Ka-band (25 – 37 GHz), Q-band (37 – 50 GHz) and V-band (50 – 70 GHz) [46, 47]. In addition, a W-band (70 – 100 GHz) is available on the Low Field Side. Furthermore, additional Q- and V-bands are available on the Low Field Side with a heterodyne detection system. While the heterodyne systems allow for a calculation of the relative density fluctuation amplitude ${\delta n}/{n}$, the homodyne systems do not. The amplitude of a measured reflectometry signal is proportional to the density fluctuations at the cut-off layer, but does also depend on e. g. the density gradient at the cut-off layer, the distance between the antenna and the cut-off layer, and the probing frequency. Therefore, a comparison between two homodyne measurements regarding the fluctuation amplitude is just possible when measuring in roughly the same density profile

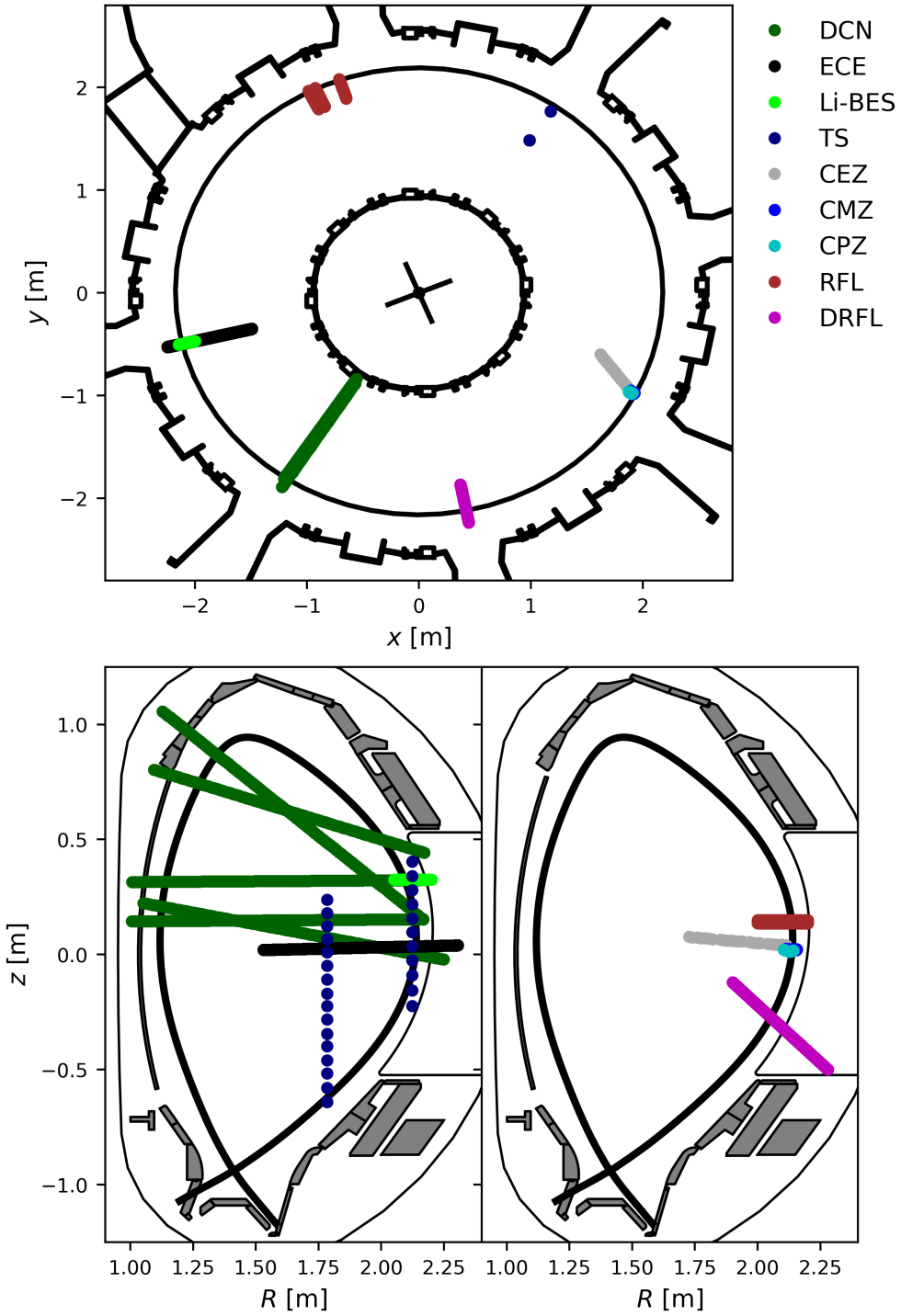

Figure 2.7: Toroidal and poloidal cross-sections of ASDEX Upgrade with the lines of sight of the Deuterium Cyanide interferometry (DCN), the Electron Cyclotron Emission spectroscopy (ECE), the Lithium Beam Emission Spectroscopy (Li-BES), the Thomson Scattering (TS), the Charge Exchange Recombination spectroscopy systems (CEZ, CMZ, CPZ), the conventional reflectometry (RFL) and the Doppler reflectometry (DRFL).

with the same probing frequency. Furthermore, in the homodyne system the measured amplitude also depends on the unknown, fluctuating phase of the signal. Figure 2.7 shows the poloidal and toroidal traces of schematic probing beams from the Ka-, Q- and K-band (from left to right in the toroidal plot).

Doppler Reflectometry

In contrast to the conventional reflectometry, the Doppler reflectometry (DRFL) has the antenna tilted in the poloidal plane away from perpendicular injection. In this case, the probing wave is reflected in a small angle away from the antenna. However, due to the finite beam width and the small injection angles, the reflected beam still contributes a significant fraction to the measured signal. The important contribution to the measured signal arises from the back-scattered beam due to the interaction of the beam with density fluctuations around the cut-off layer.

In this case, back-scattering according to Braggs-Law

$$\boldsymbol{k_\mathrm{i}} = \boldsymbol{k_\mathrm{s}} + \boldsymbol{k_\mathrm{turb}} \tag{2.1}$$

with the incident wave vector $\boldsymbol{k_\mathrm{i}}$, scattered wave vector $\boldsymbol{k_\mathrm{s}}$ and the turbulence wave vector $\boldsymbol{k_\mathrm{turb}}$ is fulfilled for $\boldsymbol{k_\mathrm{s}} = -\boldsymbol{k_\mathrm{i}}$:

$$\boldsymbol{k_\mathrm{turb}} = -2\boldsymbol{k_\mathrm{i}} \tag{2.2}$$

Therefore, the probed part of the turbulence spectrum depends on the wavenumber of the probing beam $\boldsymbol{k_\mathrm{i}} = \boldsymbol{N}k_0$ with the refractive index N and the vacuum wavenumber k_0. While the vacuum wavenumber depends just on the known frequency of the probing beam, the refractive index depends on the incident angle and has to be properly calculated by ray-tracing codes (such as TORBEAM [48]). Due to the movement $\boldsymbol{v_\mathrm{turb}}$ of turbulent structures in the plasma, the back-scattered signal experiences a Doppler shift

$$f_\mathrm{D} = \frac{\boldsymbol{v_\mathrm{turb}}\boldsymbol{k_\mathrm{turb}}}{2\pi} \tag{2.3}$$

Because the fluctuations are typically stretched out along the magnetic field line, it is assumed that $k_\perp \gg k_\parallel$. In addition, due to the higher propagation velocity of the turbulent structures in the perpendicular direction as compared to the radial direction $v_\perp \gg v_\mathrm{r}$ and the vanishing time-averaged radial wavenumber at the cut-off layer $< k_\mathrm{r} > \approx 0$, the Doppler shift can be assumed to be

$$f_\mathrm{D} = \frac{v_\perp k_\perp}{2\pi} \tag{2.4}$$

Since the perpendicular turbulence velocity is measured in the lab frame, the turbulence phase velocity v_phase in the plasma frame ($E_\mathrm{r} = 0$) can be calculated according to $v_\mathrm{phase} = v_\perp - v_\mathrm{ExB}$ with the background ExB velocity of the plasma. The background ExB velocity is determined from Charge Exchange Recombination Spectroscopic measurements (see section 2.2.2). In this thesis, one V-band (50 to 75 GHz) in X-mode [49] with a heterodyne detection scheme is used. Figure 2.7 shows the poloidal and toroidal trace of a schematic probing beam injected by the V-band antenna.

2.2.2 Charge Exchange Recombination Spectroscopy

Charge Exchange Recombination Spectroscopy (CXRS) [44, 45] is used in this thesis to measure the temperature, density and rotation velocity of impurity ions and to infer from it the radial electric field.

The underlying atomic process is the transfer of an electron from on a donating neutral particle, e. g. injected, energetic deuterium D, to a fully ionized, accepting impurity atom A with a charge number Z.

$$\mathrm{A}^{\mathrm{Z}+} + \mathrm{D}^{0} \rightarrow \mathrm{A}^{(\mathrm{Z}-1)+*} + \mathrm{D}^{+} \rightarrow \mathrm{A}^{(\mathrm{Z}-1)+} + \mathrm{D}^{+} + \mathrm{h}\nu \tag{2.5}$$

After the electron transfer, the accepting impurity atom is in an excited state and subsequently emits the excitation energy as a photon with a frequency ν. From the absolute intensity of the resulting spectrum, the impurity density can be deduced. Since the excited ion is in motion, the emitted de-excitation line is Doppler shifted. The shift of the Doppler peak and its broadening define the rotation velocity and temperature of the impurity ion, respectively. Due to the presence of the magnetic field, the temperature has to be corrected for the Zeeman-Effect. Since the main and impurity ions are in partial thermal equilibrium on the time scale of usual acquisition times of CXRS systems [23], the measured impurity temperature can be assumed to be equal to the main ion temperature.

In addition, the radial electric field E_r can be calculated from the CXRS measurement results. The force balance of a plasma, which — assuming negligible collisional friction, axi-symmetry and the pressure p being isostatic and a flux function — can be written for an impurity species α as

$$E_\mathrm{r} = -\nabla\Phi = \frac{1}{e n_\alpha Z_\alpha}\frac{\partial p_\alpha}{\partial r} - v_\theta \cdot B_\phi + v_\phi \cdot B_\theta \tag{2.6}$$

with the electric potential Φ, elementary charge e, the impurity density n_α, the impurity charge Z_α, the radial impurity pressure gradient $\frac{\partial p_\alpha}{\partial r}$, the toroidal v_ϕ and poloidal v_θ rotation velocities, and the toroidal B_ϕ and poloidal B_θ magnetic fields. While the magnetic fields can be deduced from the magnetic equilibrium, all other quantities are directly measured by CXRS.

Diagnostic	CEZ	CMZ	CPZ
Region	core	edge	edge
NBI source	#3	#3	#3
Geometrical view	toroidal	toroidal	poloidal
Integration time	10 ms	2.3 ms	2.3 ms

Table 2.1: Description of the different Charge Exchange Recombination Spectroscopy systems.

Since the CXRS system at ASDEX Upgrade [50, 51, 52] does not include a dedicated neutral beam used exclusively for plasma diagnostics but uses the neutral particles from

NBI sources #3 and #8, the experiments conducted in this thesis always included those beams if possible. If not stated otherwise, boron was used in this thesis as the electron acceptor because boron appears as the dominant impurity after a fresh boronisation (concentration of the order of 1 %). Alternatively, impurities coming from the wall (e. g. carbon, oxygen) or injected impurities (e. g. nitrogen, neon) can be used. Table 2.1 describes the different systems used in this thesis. Their respective lines of sight can be seen in the toroidal and poloidal overview plots of figure 2.7.

2.2.3 Lithium-Beam Emission Spectroscopy

The Lithium-Beam Emission Spectroscopy (Li-BES) [45] measures the electron density at the edge of the plasma.

It is based on the interaction of injected neutral lithium particles with the plasma particles. Due to atomic processes, different excited states of the electron hull of the lithium atoms are populated. The most populated state is the Li(2p) state and, therefore, the emitted line corresponding to the Li(2p $\rightarrow$ 2s) transition at 670.8 nm is detected. The electron density can then be deduced from the obtained emission profile and a set of rate coefficients provided by a collisional radiative model including ionization, impact excitation and charge exchange processes [53, 54].

The Li-BES system of ASDEX Upgrade [55] is equipped with two optical systems consisting of photo-multipliers measuring the emission profile with different radial resolution along the same trace. The lithium beam is chopped [56] with a typical duty cycle of 56 ms on and 24 ms off to allow for a background subtraction. With a typical beam acceleration voltage of 35 – 60 kV, the intensity of the neutral lithium beam drops to insufficient levels due to beam attenuation at around the pedestal top (depends on the electron density). Consequently, the electron density can be calculated just at the edge of the plasma and in the scrape-off layer. While the acquisition rate is 200 kHz, density profiles are usually calculated as an average over $50 - -200$ µs time intervals in order to improve the signal-to-noise ratio. The position of the Li-BES line of sight can be seen in the toroidal and poloidal overview plots in figure 2.7.

2.2.4 Electron Cyclotron Emission Radiometry

The Electron Cyclotron Emission Radiometry (ECE) system [57, 44, 45] is used in order to measure the electron temperature of in the plasma.

Its fundamental physics are based on the emission of radiation by accelerated charges. In a tokamak, an electron gyrating around a helical magnetic field line emits light at the cyclotron frequency

$$f = \frac{\omega}{2\pi} = l\frac{eB}{2\pi m_\mathrm{e}} \tag{2.7}$$

with the elementary charge e, the magnetic field strength B, the electron mass m_e and its harmonics l. Assuming the plasma being a black-body radiator at the cyclotron frequency,

the intensity of the emitted light I_{BB} in the range of GHz is given, with very good accuracy at fusion plasma temperatures, by the Rayleigh-Jeans approximation of Planck's law

$$I_{\mathrm{BB}} = \frac{\omega^2 k_{\mathrm{B}}}{8\pi^3 c^3} T_{\mathrm{rad}} \tag{2.8}$$

with k_{B} being the Boltzmann constant, c the speed of light and the radiation temperature T_{rad}. For a plasma intransparent at cyclotron harmonics (black-body radiator), the radiation temperature equals the electron temperature. Due to the magnetic field dependence in equation 2.7, the measurement is radially resolved, since the magnetic field behaves like $1/R$. However, the assumption of a black-body radiator is just valid where the plasma is optically thick, since the measured intensity I depends on the optical thickness τ as

$$I = I_{\mathrm{BB}}(1 - e^{-\tau}) \tag{2.9}$$

This definition neglects reflections from the wall, since at sufficiently high τ the plasma anyway absorbs the waves.

The optical thickness in ASDEX Upgrade [57] can be approximated as

$$\tau = 3.9 \cdot 10^{-19}\,\mathrm{keVm^{-3}} \cdot n_{\mathrm{e}} T_{\mathrm{e}} \tag{2.10}$$

When τ drops below 3, the measured intensity differs significantly from the black-body approximation. Consequently, ECE does not provide the electron temperature in this situation. This can be the case at the edge of the confined plasma and in the scrape-off layer, where densities and temperatures are typically low. A more advanced forward modeling is necessary in order to still obtain information on the electron temperature in this area. This is used in the framework of the integrated data analysis (see section 2.2.9). The line of sight for a toroidal magnetic field of 1.8 T is shown in the toroidal and poloidal overview plots of figure 2.7.

2.2.5 Thomson Scattering

The Thomson scattering (TS) diagnostic [44, 45] is used to provide information on the electron density and temperature.

Its principle is based on the scattering of a monochromatic electromagnetic wave on the freely moving electrons of the fully ionized plasma. From the intensity of the scattered signal, the electron density can be deduced. The information on the electron temperature is provided by the relative intensity of various spectral intervals in the back-scattered spectrum caused by Doppler broadening.

For the ASDEX Upgrade Thomson scattering system [58], two individual clusters of Nd:YAG lasers (1064 µm) are in pulsed operation with a pulse length of 10 ns, a repetition frequency of 20 Hz and an energy of 1 J. One system with its laser path line through the plasma core consists of four lasers has 16 radially distributed channels. A second system with its laser path intersecting the plasma edge and pedestal region consists of six lasers and 11 channels. Optical fibers transmit the scattered spectrum to polychromators, which

each have four spectral channels and use silicon avalanche photo diodes for detection. The scattering volumes are shown in a poloidal and toroidal cross-section in figure 2.7.

Throughout this thesis, the edge system is used in order to align different diagnostic with each other and overcome uncertainties of the reconstructed separatrix position. Its data is shifted radially, such that the measured temperature at the separatrix is consistent with the SOL heat flux to the divertor parallel to the magnetic field, typically about 100 eV. Measurements of other diagnostics measuring the electron density or temperature are then radially shifted in order to fit the Thomson scattering measurements.

The Deuterium Cyanide (DCN) Interferometry diagnostic [44, 45]

2.2.6 Plasma Interferometry

An interferometer measures the line-integrated density measurement of the plasma. The diagnostic is based on the measurement of the phase shift between a coherent electromagnetic wave traveling through the plasma and a reference wave (typically through air or vacuum).

$$\varphi = \frac{\lambda e^2}{4\pi c^2 m_\mathrm{e} \epsilon_0} \int_0^L n_\mathrm{e}(x) dx \tag{2.11}$$

At ASDEX Upgrade, the probing wave is generated by a deuterium cyanide (DCN) laser (wavelength $\lambda = 195\,\mu\mathrm{m}$) in O-mode [59]. The phase shift is then registered by a Mach-Zehnder interferometer with a sampling rate of 10 kHz. The reference medium is air, which has a refractive index of $N_\mathrm{ref} \approx 1$. In total, five chords are in operation and provide information from within the pedestal top up into the core region. These lines of sight are shown in the overview plots of figure 2.7. The starting points in this plot of the cross-section on the left hand side, i. e. on the high field side, belong to the channels H-4, H-5, H-2, H-0 and H-1 going from top to bottom.

2.2.7 Langmuir Probes

Langmuir probes [44, 45] are used in this thesis for measuring the electron density and temperature at the divertor.

This diagnostic is based on the measurement of an I-V characteristic of a set of one or more electrodes in contact with the plasma with a time varying electric potential between each electrode or the ground. The measured I-V characteristic yields the ion saturation current $I_\mathrm{i,sat}$ and the floating potential V_f, from which the electron density and temperature can be deduced.

At ASDEX Upgrade, triple probes [60] are in use due to their high time resolution ($\approx$ 22 kHz) and robustness against potential fluctuations. In addition, their power supplies are less complicated (no sweeping needed) and the analysis is simple. In this setup, one probe is floating at V_f, one is biased positively V_+ and one negatively V_-, such that $e(V_+ - V_-) \gg T_\mathrm{e}$. While the negatively charged probe pulls the ion saturation current $I_\mathrm{i,sat}$, the positively charged probe can only reach a current of the same amplitude as $I_\mathrm{i,sat}$, but opposite polarity.

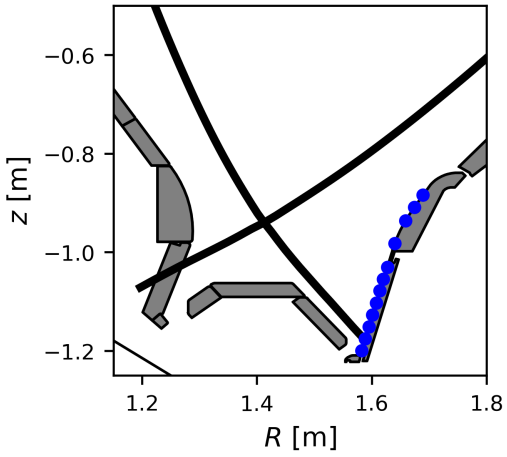

Figure 2.8: Poloidal cross-section of the lower divertor region showing the measurement positions of Langmuir probes on the outer divertor. From the bottom to the top, these probes are labeled from *8ua1* to *8ua9* and finally *8uaa*, *8uab* and *8uac*.

The electron temperature and density can be deduced as:

$$T_\mathrm{e} = \frac{-e(V_+ - V_\mathrm{f})}{k_\mathrm{B}\ln(2)}$$

$$n_\mathrm{e} = \frac{I_+ - I_\mathrm{i,sat}}{eS_\mathrm{eff}\sqrt{k_\mathrm{B}T_\mathrm{e}/2\pi m_\mathrm{e}}}\mathrm{e}^{-\mathrm{eV_+}/\mathrm{k_B T_e}}$$

with the Boltzmann constant k_B, the electron m_e and ion m_i mass, the elementary charge e and the effective probe surface S_eff considering the inclination angle of the magnetic field lines. The poloidal position of the triple probes in the lower, outer divertor of AUG are shown in figure 2.8. The channels are numbered consecutively from 1 to 12 starting from the bottom. Channels *8ua1* to *8ua9* are at a toroidal angle of $\phi = 165\,^\circ$ and *8uaa* to *8uac* at $150\,^\circ$.

2.2.8 Divertor Shunt Current

At ASDEX Upgrade, shunt resistors are used to measure the thermo-electric current in the scrape-off layer. These low-ohmic resistors are installed between a divertor tile and the substructure the tile is mounted on, both, the inner and outer divertor. The voltage drop across the shunt resistors is used to measure the current flowing through magnetic field lines in the scrape-off layer connecting the inner and outer divertor. This current is driven by the temperature difference between the connected divertor tiles and is sensitive to the resistivity of the plasma in the scrape-off layer, which is influenced by particle and heat fluxes from the separatrix to the divertor. Consequently, the divertor shunt current can be used as an indicator for heat fluxes originating from the confined region,transported through the separatrix into the scrape-off layer and finally reaching the divertor. One

practical use of this shunt current is, therefore, its applicability as a monitor for edge localized modes, which cause an ejection of heat and particles from the confined region into the scrape-off layer leading to a transient sharp peak in the divertor shunt current measurement. In the following, the divertor shunt current measured in the outer divertor is labeled as I_{div}.

2.2.9 Integrated Data Analysis

Usually, the measurements of each diagnostic are analyzed independently and afterwards mapped onto a common coordinate such as the normalized poloidal flux radius ρ_{pol}, where it can be then compared to the results of other diagnostics. The concept of Integrated Data Analysis (IDA) [61] within the framework of Bayesian probability theory, however, uses the measurements of multiple complementary diagnostics for a certain set of parameters, e. g. electron density. The measured signals of each diagnostic are then forward modeled, starting with a set of parameters mapped onto the common coordinate. A comparison to the raw measured signals is then used to validate the set of parameters with a likelihood probability distribution.

This tool is used to provide radial profiles of the electron density, electron temperature and ion temperature profiles.

2.3 Magnetic Equilibrium Reconstruction

2.3.1 2D-equilibrium with CLISTE

The 'CompLete Interpretive Suite for Tokamak Equilibria' (CLISTE) code [62] solves the Grad-Shafranov equation

$$-\Delta^*\Psi = \mu_0 R^2 \frac{dp}{d\Psi} + \frac{\mu_0^2}{4\pi^2} I_{\mathrm{pol}} \frac{dI_{\mathrm{pol}}}{d\Psi} \tag{2.12}$$

$$\Delta^* = R\frac{\partial}{\partial R}\left(\frac{1}{R}\frac{\partial}{\partial R}\right) + \frac{\partial^2}{\partial z^2}$$

which is a 2-dimensional, non-linear, partial differential equation in the flux function Ψ for given parametrized source profiles of the pressure p and poloidal current I_{pol}. It is derived from an axisymmetric (in ϕ) force balance $\nabla \boldsymbol{p} = \boldsymbol{j} \times \boldsymbol{B}$ between the plasma pressure gradient and the jxB force. It is solved iteratively by varying the free parameters of the source profiles in order to find a least square fit to magnetic measurements of radial and poloidal fields measured outside the plasma. Additional information such as temperature, density or current profiles can be optionally used as constraints.

In this thesis, CLISTE is used for the purpose of mapping different diagnostics (introduced in section 2.2), which measure at certain positions in the cylindrical coordinate system (R, ϕ, z) of the lab frame, onto the magnetic flux coordinate ρ_{pol} defined in equation 1.1. The q profile calculated by CLISTE is used to identify the approximated positions of resonant surfaces. The magnetic equilibrium serves also as an input for the transport code ASTRA and the 3D equilibrium code VMEC. Furthermore, its magnetic equilibrium is used in combination with the vacuum field calculation of the radial magnetic perturbation field by VACFIELD [63] for field-line tracing in the scrape-off layer.

2.3.2 3D-equilibrium with VMEC

In order to calculate the corrugation of flux surfaces due to the application of radial magnetic perturbations, the 3-dimensional ideal MHD equilibrium code 'Variational Moments Equilibrium Code' (VMEC) [**?**] is used. Since VMEC is an ideal MHD code, no resistive effects induced by the 3D perturbation field, such as the formation of magnetic islands at resonant surfaces or an ergodization of the edge region, are described. Since a possible existence of magnetic islands would influence the surface corrugation, the latter might be fraught with an unknown uncertainty.

The approach of VMEC is to solve the ideal MHD equilibrium equation $\nabla \boldsymbol{p} = \boldsymbol{j} \times \boldsymbol{B}$ in three dimensions by minimizing the potential energy

$$W = \int (\frac{1}{2\mu_0} B^2 + p) dV$$

in the whole plasma volume assuming nested flux surfaces. VMEC equilibria are only defined in the confined region. The calculation of a VMEC equilibrium uses a CLISTE

equilibrium including the pressure profile and current profile as an initial condition. VMEC is then run in the fixed-boundary mode (i. e. keeping the same last closed flux surface as defined by CLISTE) in order to allow the q profile to relax. In the resulting equilibrium, the q profile is flattened in the vicinity of the separatrix and truncated in order to avoid the singularity of the X-point. Thereafter, it is run in free-boundary mode using the previously calculated q profile. In the free-boundary mode, VMEC searches the solution minimizing the potential energy and matching the vacuum field at the separatrix generated by all external source as calculated VACFIELD [63]. These sources include all toroidal field and shaping coils as well as the radial magnetic perturbation coils.

Chapter 3

The Pump-out Effect in ELM Mitigation and Suppression Scenarios

One of the main concerns for a future fusion power plant is the question of how to deal with edge localized modes (ELMs), since they impose a threat to the plasma facing components [30, 64]. Externally applied magnetic perturbation (MP) fields (introduced in section 2.1) are capable of mitigating or even suppressing ELMs. In this chapter, the plasma scenarios used at ASDEX Upgrade for the mitigation or suppression of ELMs with magnetic perturbations are briefly introduced. It is distinguished between discharges with low triangularity (section 3.1) and high triangularity (section 3.2) due to the different effect on ELMs. In both scenarios, also the influence of such MP fields on the plasma temperature, density and pressure is studied for example discharges. All experimental work of this thesis is based on these scenarios described in the following.

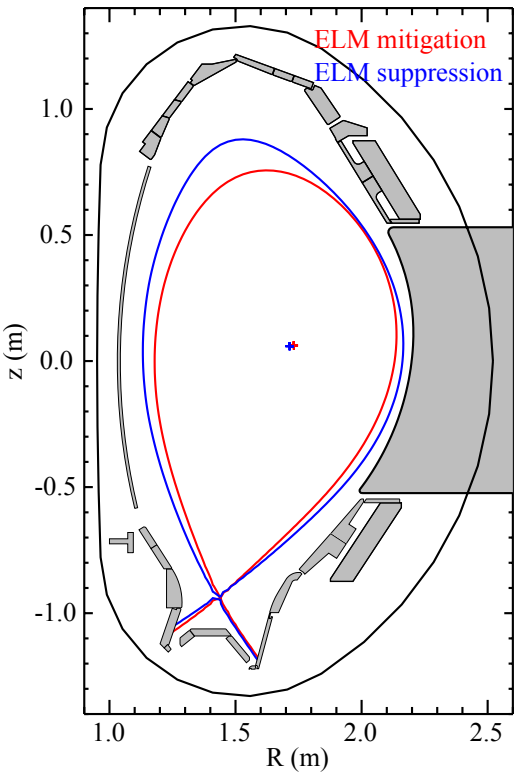

Figure 3.1: Poloidal cross-section of ASDEX Upgrade showing the separatrices of the ELM mitigation (red) and ELM suppression (red) scenarios.

Both scenarios aim at low pedestal collisionality $\nu^* < 1$ in order to reproduce as much as possible the required pedestal collisionality in ITER, $\nu^* \approx 0.1$ [6]. In order to achieve this, little to no deuterium gas puff is used in any of those scenarios keeping the density low, and a heating scheme composed of neutral beam injection (NBI) [13, 65] and electron cyclotron resonance heating (ECRH) [13, 65] is applied. The toroidal magnetic field of these scenarios is chosen such that the ECRH

power is deposited centrally, which avoids the
accumulation of tungsten in the plasma (second harmonic at $B_\phi = 2.5\,\mathrm{T}$ or third harmonic at $B_\phi = 1.8\,\mathrm{T}$). The plasma is shaped in a lower-single-null configuration with a lower triangularity of about $\delta_\mathrm{l} \approx 0.43$ (see figure 3.1). The lower triangularity can not be modified significantly in the ELM control scenarios, since the strike-point on the outer divertor has to be located close to the divertor gap. This allows for best conditions for deuterium pumping, keeping the density of the plasma low, which is crucial for achieving a low collisionality plasma with ELM mitigation or suppression.

3.1 Low Triangularity: ELM Mitigation

After the installation of the MP coil system in 2010 and first attempts of ELM mitigation and suppression at high collisionality [36, 42, 66, 67, 68, 69], scenarios at ITER-like collisionality ($\nu^* \approx 0.15$) and strong ELM mitigation came into the focus of magnetic perturbation research at ASDEX Upgrade [70, 71, 72]. Those scenarios have been developed with a small upper triangularity of $\delta_u \approx 0.06$. In this scenario, ELM mitigation was found in a rather broad control parameter space: a toroidal magnetic field B_ϕ of 1.8 to 2.5 T and a plasma current I_p of 0.6 to 1.2 MA resulting in a wide edge safety factor q_{95} range of around 3.0 to 6.0, a vanishingly small gas puff $\Gamma_D \leq 10^{21}$ particles/s and a total external heating power P_{tot} in the range of approximately 5 to 10 MW.

Figure 3.2 shows the time traces of a discharge exemplary for the ELM mitigation scenario at low triangularity. This discharge is selected as an example due to the high degree of ELM mitigation achieved in it and it also shows the strongest effect on density and temperature profiles. In this scenario, a toroidal magnetic field of $B_\phi = 1.8$ T and a

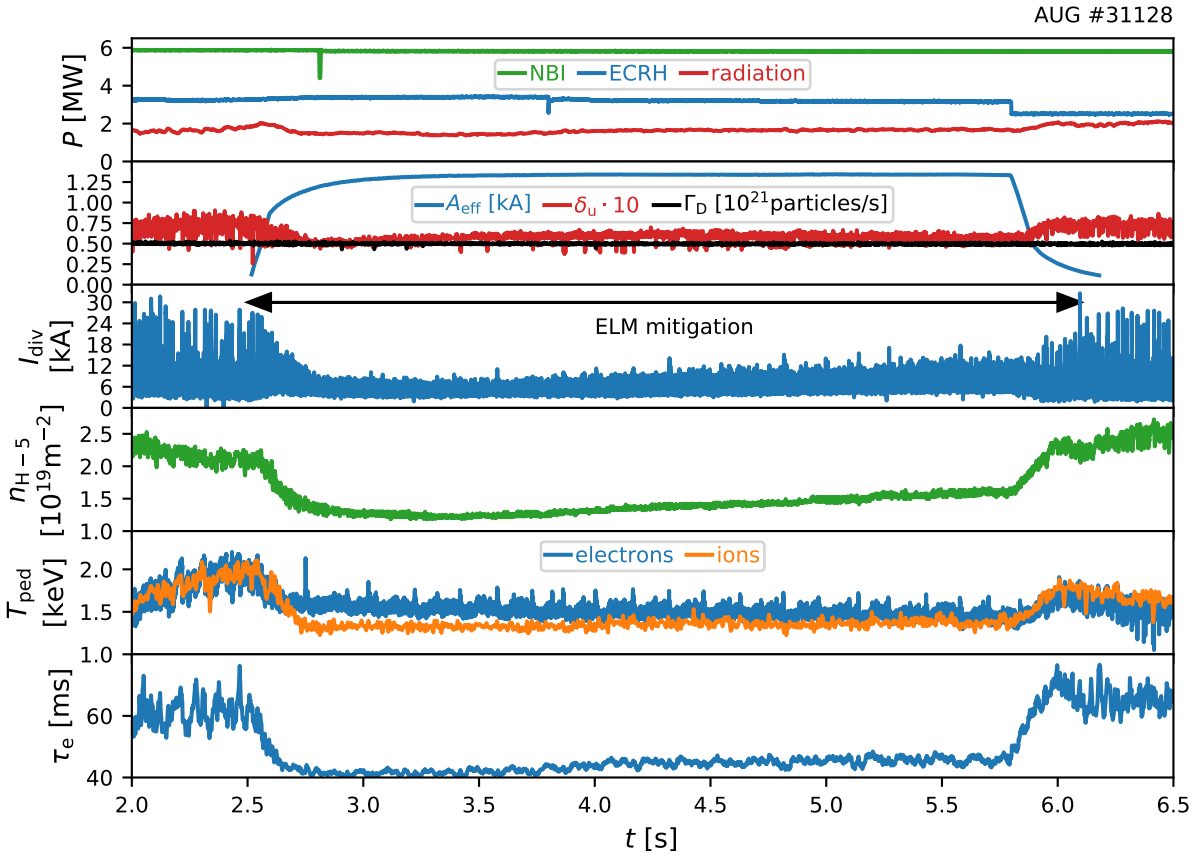

Figure 3.2: Time traces of a low triangularity ELM mitigation scenario showing the heating power by neutral beam injection P_{NBI} and electron cyclotron resonance heating P_{ECRH}, the radiated power $P_{radiation}$, the effective $n = 2$ MP coil current amplitude A_{eff}, the deuterium gas puff Γ_D, the upper triangularity δ_u times 10, the outer divertor shunt current I_{div}, the line-integrated electron edge density n_{H-5}, electron $T_{e,edge}$ and ion $T_{i,edge}$ edge temperature and the energy confinement time τ_e.

plasma current of $I_\mathrm{p} = 0.83\,\mathrm{MA}$ were used, which resulted in an edge safety factor of $q_{95} = 3.8$. The total heating power of about 9 MW is comprised of three NBI source with 2 MW each and about 3 MW of ECRH heating. In this discharge, an MP coil setup with a toroidal mode number $n = 2$, a differential phase angle $\Delta\phi = +96\,^\circ$ (resonant at the pedestal top) and an effective $n = 2$ MP coil current amplitude of $A_\mathrm{eff} = 1.34\,\mathrm{kA}$ has been used. As soon as the MP coils were switched on at $t = 2.5\,\mathrm{s}$, the goal of mitigating ELMs has been achieved as the energy loss per ELM drops by roughly a factor of four. However, also the density and temperatures decrease with the application of the perturbation field due to the pump-out effect. This has consequences for the performance of the plasma, described by the energy confinement time τ_e. With the application of the MP field, τ_e dropped significantly from about 62 ms to 41 ms (a reduction of about 33 % indicating strongly reduced confinement properties in the ELM mitigated phase as compared to the preceding H-mode). The radiated power reduces during the ELM mitigated phase even further, possibly due to the increase in ELM frequency.

Since all control parameters were kept constant at least in the time around the application of the perturbation field at $t = 2.5\,\mathrm{s}$, one can compare the density, temperature and pressure profiles (see figure 3.3) without magnetic perturbations at $t \approx 2.45\,\mathrm{s}$ directly to those taken at $t \approx 3.35\,\mathrm{s}$ with magnetic perturbations. Changes in the profiles can then be attributed to an application of an MP field. These changes are:

- n_e is reduced at the pedestal top and accordingly the density in the entire plasma core is lowered, while the profile shape hardly changes.
- T_e changes little, and entirely within the errorbars.
- T_i is reduced significantly at the pedestal top and significantly flattens in the outer half of ρ_pol.
- p_e is reduced in the whole plasma due to the change in the density.
- p_i is reduced stronger than p_e due to a combination of the density and ion temperature loss.
- p (total pressure) is consequently also reduced.

The absence of a change in the core shape of the electron density profile suggests that the reduction of the density in the core region is a consequence of the reduction of the pedestal top density. While the electron temperature profile does not change, a significant drop in the ion temperature can be observed in the whole plasma.

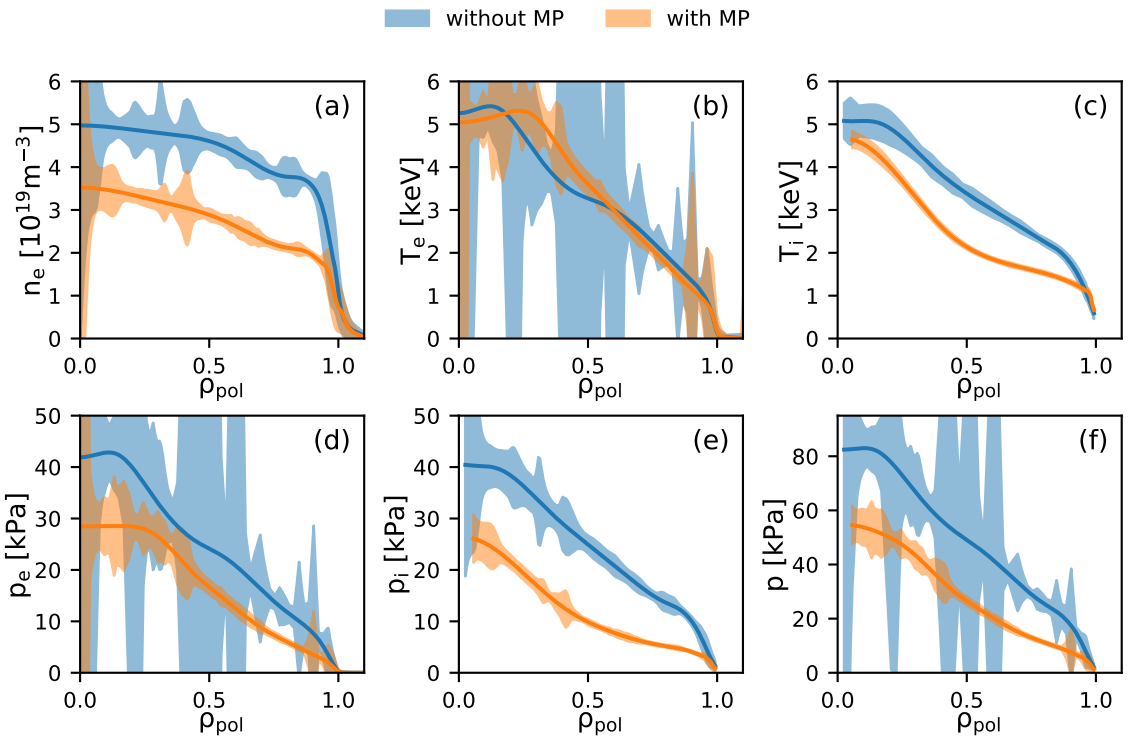

Figure 3.3: Radial profiles of ASDEX Upgrade #31128 showing the (a) electron density (IDA including DCN, Li-BES and TS), (b) electron temperature (IDA including ECE and TS), (c) ion temperature (CXRS), (d) electron pressure, (e) ion pressure and (f) total pressure profiles before magnetic perturbations were applied at $t = 2.45\,\mathrm{s}$ (blue) and with powered MP coils at $t = 3.3\,\mathrm{s}$ (orange).

3.2 High Triangularity: ELM Mitigation and Suppression

While ELM mitigation was found in a rather broad range of control and plasma parameters, the access to ELM suppression is more restricted. First of all, the plasma current and toroidal magnetic field have to be such that the plasma operates in certain q_{95} windows, which depend on the toroidal mode number of the applied MP field, the plasma shape and collisionality [73]. Hints indicate also a possible existence of a rotation threshold in DIII-D [74], but to date no such threshold was found in AUG [75]. Another parameter important for ELM suppression was found in similarity experiments conducted on both, DIII-D and

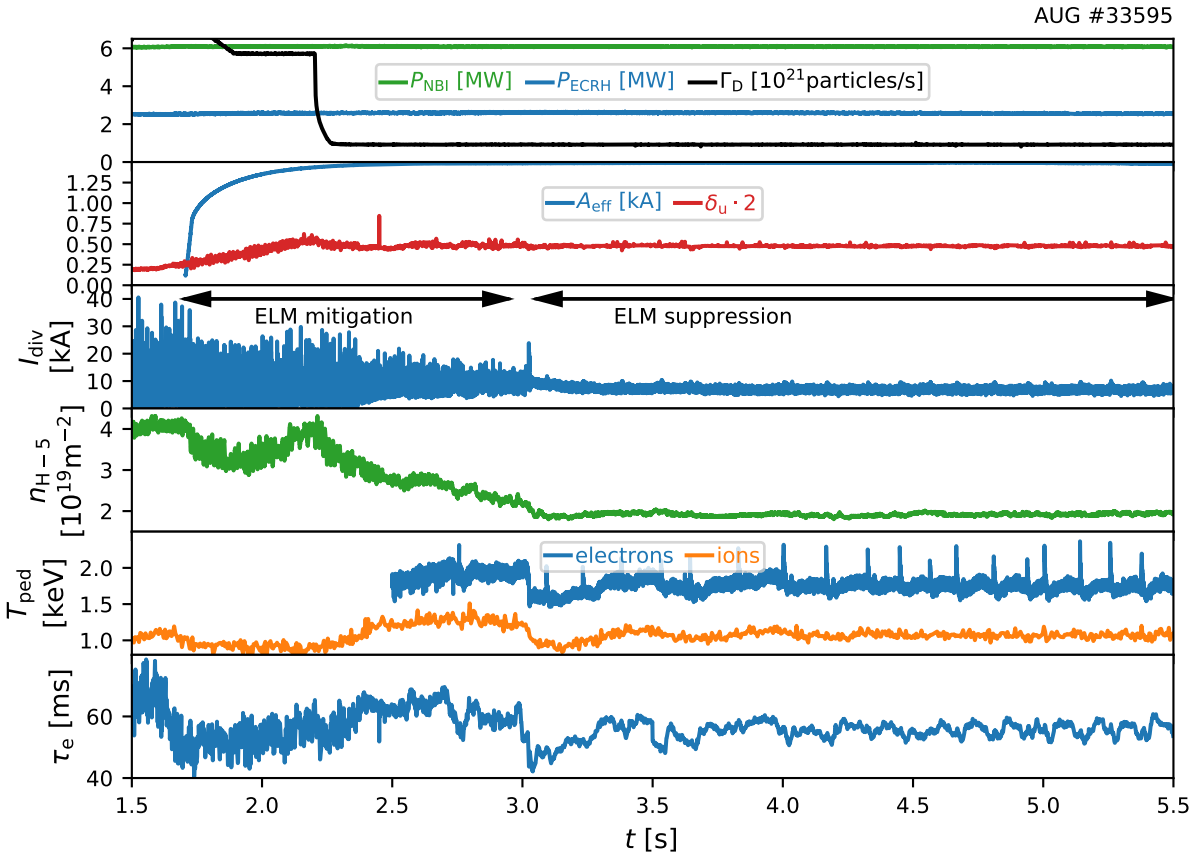

Figure 3.4: Time traces of a high triangularity ELM suppression scenario showing the heating power by neutral beam injection P_{NBI} and electron cyclotron resonance heating P_{ECRH}, the radiated power $P_{\mathrm{radiation}}$, the effective $n = 2$ MP coil current amplitude A_{eff}, the deuterium gas puff Γ_{D}, the upper triangularity δ_{u} times 10, the outer divertor shunt current I_{div}, the line-integrated electron edge density $n_{\mathrm{H-5}}$, electron $T_{\mathrm{e,edge}}$ and ion $T_{\mathrm{i,edge}}$ edge temperature and the energy confinement time τ_{e}.

ASDEX Upgrade: the plasma triangularity [76, 77, 75]. This work also suggests an empirical limit in the edge density. Furthermore, the plasma facing components must be covered with a boron layer, which improve the pumping of deuterium.

As mentioned previously, the lower triangularity can not be varied significantly and, hence, the upper triangularity is further increased to achieve ELM suppression in ASDEX Upgrade. At higher triangularity, the ELM frequency decreases and, consequently, the exhaust of impurities is smaller. This can lead to impurity accumulation if no significant gas puff is employed. As a solution, plasma discharges with the goal of achieving low pedestal collisionality at elevated triangularity start at the low triangularity scenario (see figure 3.4) and the application of magnetic perturbations at $t = 1.7\,\mathrm{s}$ leads to a weak mitigation of ELMs and a consequent increase of their frequency. This in turn helps to avoid an accumulation of impurities in the plasma. Then the upper triangularity is ramped up to about $\delta_\mathrm{u} \approx 0.24$ and the gas puff is reduced in order to lower the density and collisionality. At $t = 3\,\mathrm{s}$, the transition into complete ELM suppression occurs. The applied MP field is similar to the MP field in the ELM mitigation case at low triangularity. It has a toroidal mode number of $n = 2$, a differential phase angle $\Delta\phi = +95\,^\circ$ and an effective $n = 2$ MP coil current amplitude of $A_\mathrm{eff} = 1.49\,\mathrm{kA}$. This magnetic perturbation scenario at high triangularity shows a significantly better performance in terms of the energy confinement time τ_e. During the transition from the pre-MP phase at $t < 1.7\,\mathrm{s}$ to the ELM suppressed phase, adjustments to the gas puffing rate and the upper triangularity have been applied. Since these changes have a direct influence on the plasma parameters, changes between the pre-MP and the ELM-mitigated/suppressed phases can not solely be attributed to the magnetic perturbation field. Therefore, comparisons are made to a reference discharge #33998 at $t = 3.0$ – $3.1\,\mathrm{s}$ without magnetic perturbations, which did not collapse due to radiation. Comparing the confinement time during ELM suppression of $\tau_\mathrm{e} = 55\,\mathrm{ms}$ to a confinement time of $\tau_\mathrm{e} = 70\,\mathrm{ms}$ in #33998, this equals to a confinement reduction of 23 %. This is a significantly less confinement reduction as compared to the low triangularity ELM mitigation case. In addition, in the ELM suppression scenario the confinement can be further improved by operating at reduced MP coil currents, which keep the electron density just below the empirical limit. The confinement time could be increased in the same way in the ELM mitigation scenario, however, then also the energy loss associated with the ELMs increases, too [39]. A comparison between the ELM mitigated and suppressed phase in #33595 to the reference phase in #33998 shows the following changes with the application of the magnetic perturbation field:

- n_e is reduced at the pedestal top and accordingly the whole core profile is lowered, while the profile shape hardly changed. A further reduction can be seen at the transition into ELM suppression.

- T_e shows an increase with MPs due to steepening in the whole plasma.

- T_i shows a slight increase in the outer core region, while the increase in the center is very pronounced.

- p_e is reduced only slightly since the increase in T_e nearly makes up for the decrease in n_e.

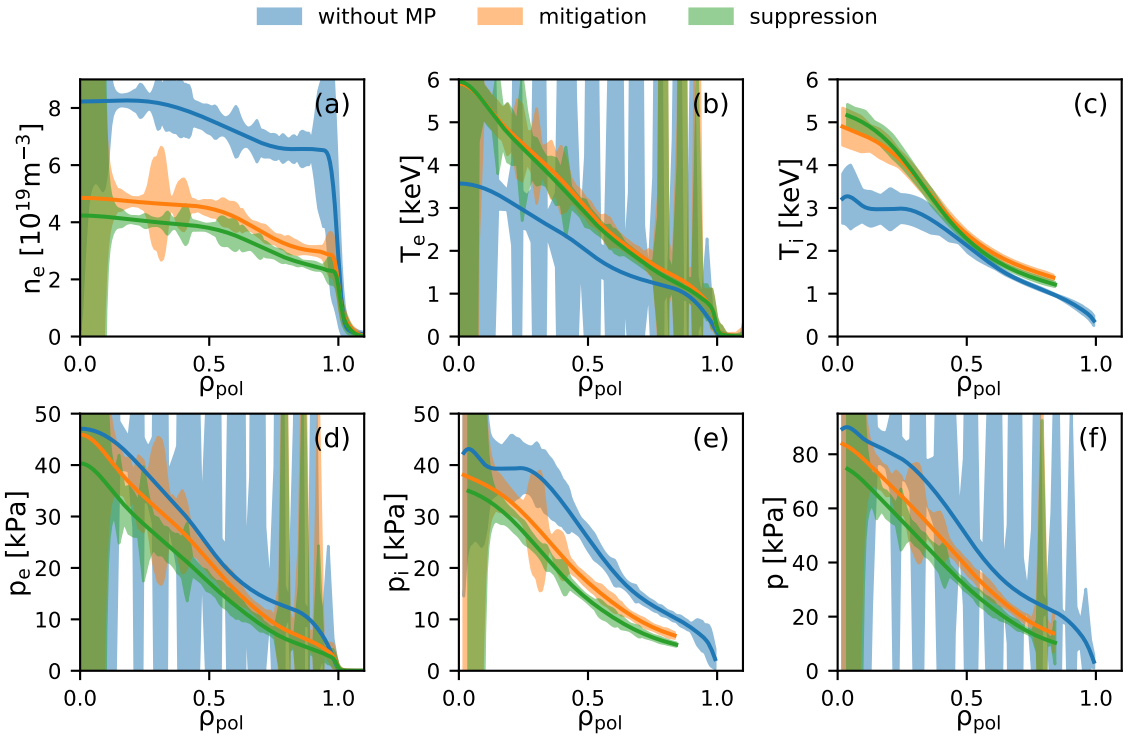

Figure 3.5: Radial profiles of the (a) electron density (IDA including interferometry, Li-BES and TS), (b) electron temperature (IDA including ECE and TS), (c) ion temperature (CXRS), (d) electron pressure, (e) ion pressure and (f) total pressure profiles for #33998 without magnetic perturbations at $t = 3.0 - 3.1$ s (blue), for #33595 at $t = 2.9 - 3.0$ s in ELM mitigation (orange) and for #33595 at $t = 4.1 - 4.2$ s in ELM suppression (green).

- p_i is reduced since the increase in T_i is weaker than that of T_e, except in the center, where p_i is hardly changed.
- p is consequently reduced only slightly.

While the electron density profiles show hardly any change of their shape in the core, the gradient in the edge becomes smaller. The change during the transition from mitigation to suppression shows the same characteristics. The electron as well as ion temperature increase in the whole plasma with the application of the magnetic perturbation. Contrary to the electron density, a further change in the temperature profiles can not be observed during the transition from mitigation to suppression. In the profiles of the pressure, one can see that the total pressure reduction of less than 20 % is not as significant as in the low triangularity regime.

3.3 Summary

From the presented low collisionality measurements one can see that, while the drop of electron density due to the magnetic perturbations is always present, the effect on the temperature profiles can vary. At low triangularity, the electron temperature stays approximately constant, while the ion temperature drops. On the other hand, at high triangularity the temperatures of both, the electrons and ions, increase and nearly make up for the pressure loss due to the density reduction. In this thesis, the focus is on the effects of the magnetic perturbations on the density.

The density pump-out effect seems unavoidable if one wants to significantly mitigate or suppress ELMs with magnetic perturbations in the low collisionality scenario. In the low triangularity case, the energy loss due to ELMs scales with the electron density at the pedestal top [39] and, hence, refueling in order to counteract the density pump-out increases the energy loss per ELM. In the high triangularity scenario, the density at the pedestal top has to stay below an empirical limit for ELM suppression, $3 \cdot 10^{-3}\,\mathrm{m}^{-3}$ at the pedestal top. Attempts to refill such plasmas above this empirical limit also bring back ELMs [78, 79]. Furthermore, an additional density pump-out can be observed when ELM suppression is achieved with full MP coil amplitude.

Chapter 4

Radial Localization of Enhanced Transport

As we have seen in chapter 3, application of non-axisymmetric magnetic perturbations leads to a reduction of plasma density, the so-called 'pump-out' effect. Although the plasma density is affected in the entire plasma volume, it is not a priori evident whether the transport mechanism that leads to 'pump-out' is also globally present in the plasma or just a phenomena at the plasma edge, where the magnetic perturbation is strongest. In case of locally increased transport, global changes of particle density can occur by outward diffusion. In this chapter, we aim to resolve this question by actively influencing the pump-out strength through a modulation of the perturbation field amplitude. The resulting density waves can be observed by several diagnostics measuring the electron density in the whole plasma. From the propagation of these waves one can learn about the origin of the pump-out effect. The performed experiment is described in section 4.1 and its results are shown in section 4.2. In section 4.3, the propagation of the density waves in the plasma is reproduced by transport simulations performed with the ASTRA code [80].

4.1 Modulation of the Magnetic Perturbation Field Amplitude

The modulation experiment is based on the ELM suppression scenario (see section 3.2) where, due to the absence of ELMs, the modulation is more precisely diagnosed. This scenario, however, strongly limits the possible amplitude range of the modulation. While there is always an upper limit for the current in each individual MP coil due to Lorentz forces, operating in ELM suppression also calls for a minimum amplitude for preserving this regime. In addition, the frequency of the modulation f_{mod} has to be such that one achieves as many periods as possible during a discharge, while maintaining an as strong as possible modulation, since the amplitude of the density wave decreases with increasing modulation frequency. It is essential that the modulation is resolvable by the Thomson scattering (TS) system, which measures the electron density over a wide radial range. In the experiments, modulations with $f_{\mathrm{mod}} = 10$ and 4 Hz have been hardly observable in the Thomson scattering signals. The best measurements were achieved with a 125 A modulation at 2 Hz on top of a constant $A_{\mathrm{eff}} = 1.025$ kA perturbation.

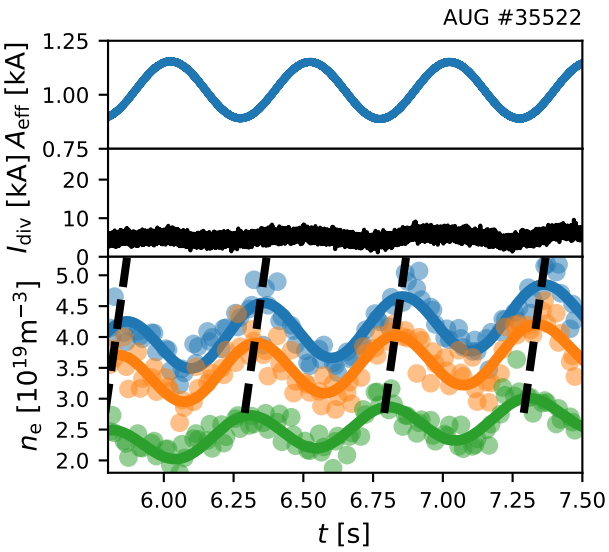

Figure 4.1: Evolution of the electron density during a modulation of the magnetic perturbation field amplitude in an ELM suppressed H-mode scenario in #35522. Time traces of the effective $n = 2$ MP coil current amplitude A_{eff} and the divertor shunt current I_{div} as well as the electron density n_{e} measurement by Thomson scattering at $\rho_{\mathrm{pol}} \approx 0.2$ (blue), $\rho_{\mathrm{pol}} \approx 0.5$ (orange) and $\rho_{\mathrm{pol}} \approx 0.9$ (green).

Figure 4.1 shows the modulation of the effective $n = 2$ MP coil current amplitude, which was applied after the transition into ELM suppression in #35522. During the modulation, no spikes can be seen in the divertor shunt current, which consequently means that ELM suppression was preserved at all times during the modulation. At the same time, the electron density is modulated, as shown by the Thomson scattering measurements. The modulated electron density signals shown in figure 4.1 at different radial positions exhibit a time delay with respect to each other as indicated by the dashed lines. The maxima in these signals occur just after the effective $n = 2$ MP coil current amplitude reaches its minimum. The electron density, averaged over modulation periods, increases slowly with time. This is a result of the reduced background MP coil currents in order to provide headroom for the modulation, which does not allow to maintain the initial, low density level.

4.2 Evaluation of the Density Modulation

For the evaluation of the electron density modulation, measurements from Thomson scattering (TS), interferometry (DCN) and lithium-beam emission spectroscopy (Li-BES) are used (see section 2.2) in #35522 in the time window from $t = 5.8$ to 7.5 s. This range provides three full periods of the modulation for analysis. In this time window, the signals of all channels of the aforementioned diagnostics as a function of time are fitted with a function consisting of a trigonometric and a polynomial term:

$$f(t) = \sum_{i=1}^{I} [A_\mathrm{i} \sin(i\omega t) + B_\mathrm{i} \cos(i\omega t)] + \sum_{j=0}^{J} C_\mathrm{j} t^j \tag{4.1}$$

with the highest order of the trigonometric term I, the highest order of the polynomial term J, the angular modulation frequency $\omega = 2\pi f_\mathrm{mod}$ and the time t. The fit to three channels of the TS system is shown in figure 4.1. The polynomial term accounts for the slow increase of the background electron density during the modulation. The $n = 2$ contribution (first order) of the trigonometric term of each signal is used for further Fourier analysis. A discrete Fourier-Transformation is used on the $n = 2$ components of each signal in order to determine the amplitude and phase of the density modulation at each radial position. The phase is calculated with respect to the phase of the effective $n = 2$ MP coil current amplitude but shifted by π, because the strength of the pump-out is expected to be in anti-phase with the density evolution. Hence, $\phi = 0$ refers to a signal being in perfect anti-phase to the effective $n = 2$ MP coil current amplitude.

The evaluated amplitude normalized to the background density and phase of each electron density measurement is plotted in figure 4.2 as a function of ρ_pol. The radial position of the interferometry measurement is where the beam is tangential to a flux surface. While the modulation of the MP field strength modulates the electron density, also the induced surface corrugation can be expected to be modulated. Since already small changes in the surface corrugation can influence measurements significantly in the edge gradient region, the Li-BES channels probing that region are omitted. The phase of the density modulation decreases from the very core region towards the separatrix. Here, the measurement by the interferometry shows the same trend as the Thomson scattering system, however, it seems to be slightly offset towards smaller phase. The reason might be the line-integrated nature of this measurement. This radial phase profile of the electron density modulation shows that the change in density induced by the MP coils occurs first at the pedestal top and propagates towards the plasma center. The normalized amplitude stays roughly constant in the whole radial region at about 10 %. Crossing the separatrix, the phase in the scrape-off layer is shifted by approximately π as compared to the measurements at the pedestal top. A decrease of the density in the confined region means that particles are expelled into the scrape-off layer and, hence, the signal at the pedestal top in the confined region is in anti-phase with the signals in the scrape-off layer. The normalized amplitude increases in the scrape-off layer, due to the strongly decreased background density as compared to the confined region.

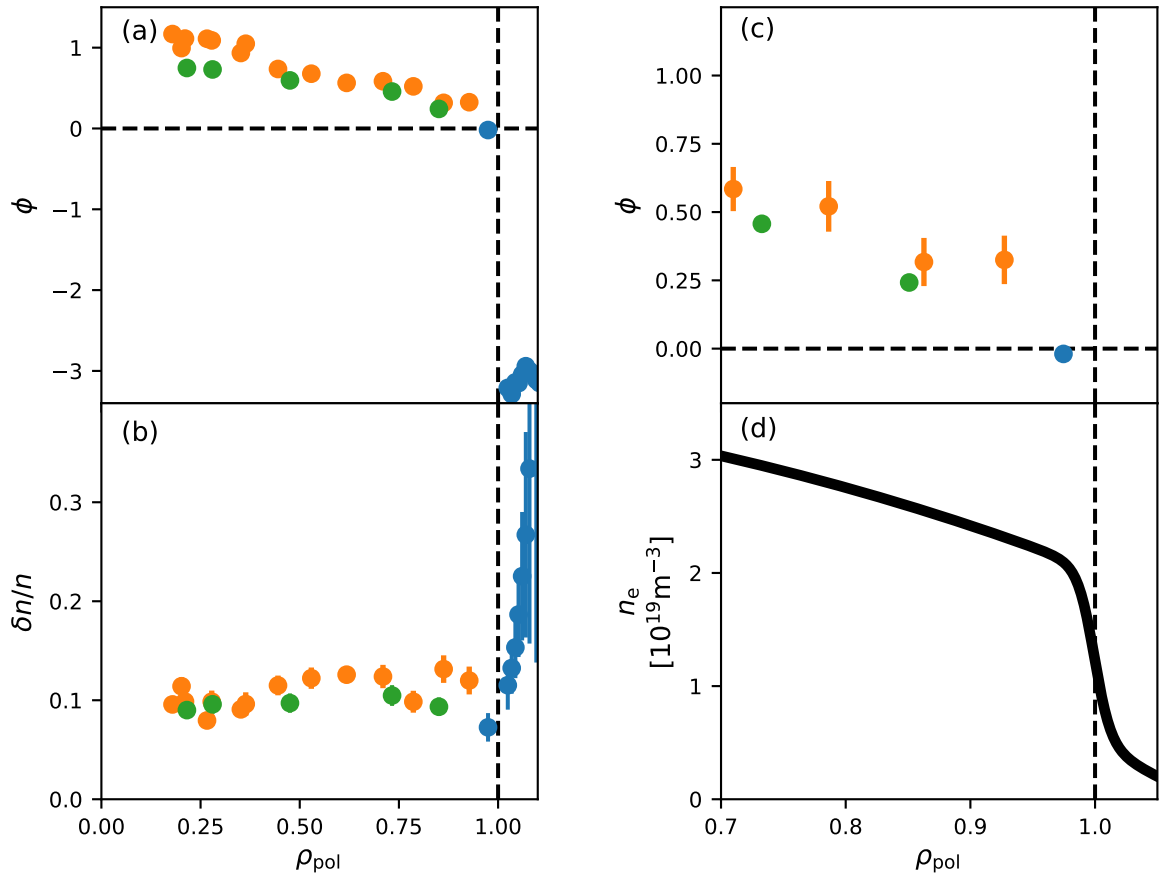

Figure 4.2: Radial profile of the phase ϕ (a) and normalized amplitude $^{\delta n}/_{n}$ (b) of the density modulation as measured by TS (orange), DCN (green) and Li-BES (blue). A magnification of the phase ϕ around the edge is shown in (c) relative to a fit of the electron density profile (d).

4.3 Simulation of the Density Modulation

Transport simulations with ASTRA are performed in order to investigate whether or not the density modulation observed in the core region can be explained by a modulated particle transport restricted to the the steep gradient region. General information on the application of ASTRA in this thesis can be found in appendix B. Initial conditions for the simulation are given by measurements of the electron density, electron temperature, ion temperature and toroidal rotation of #35522 at $t \approx 5.65\,\mathrm{s}$. Since ion temperature and toroidal rotation measurements at the edge were not available in #35522, these measurements are taken from a similar discharge #35307.

First, ASTRA is run in the interpretative mode in order to determine the power balance electron heat conductivity χ_e up until $t = 0.5\,\mathrm{s}$. From the electron heat conductivity, the electron particle diffusion coefficient is approximated as $D_\mathrm{e} \approx 0.4 \cdot \chi_\mathrm{e}$. The particle pinch velocity v is then calculated by the stationary diffusion-convection equation $D \cdot \nabla n_\mathrm{e} - v \cdot n_\mathrm{e} + S = 0$ with the sources and sinks S. For the purpose of this thesis, thermal diffusion (particle diffusion due to gradients in the electron or ion temperature) is neglected. After determining the electron diffusion coefficient and pinch velocity, the simulation is continued predictively from $t = 0.5\,\mathrm{s}$ on and a sinusoidal modulation of the electron diffusion is superimposed in the radial range $\rho_\mathrm{tor} = 0.955$ to 0.98 (see figure 4.3). The frequency of the modulation is fixed to the frequency of 2 Hz used in the experiment. From $t \approx 2\,\mathrm{s}$ on the amplitude and phase of the density modulation is leveled off and a discrete Fourier-Transformation is then used on all radial grid points of the electron density evolution as predicted by ASTRA. The amplitude of the superimposed D_e modulation is then adjusted such that the difference between the amplitude of the simulated density modulation and the amplitude measurement of the two outermost channels of the core Thomson scattering system is minimized. Furthermore, a phase offset is added to the simulation result such that the difference between the phase of the simulated density modulation and the phase of the two outermost channels of the core

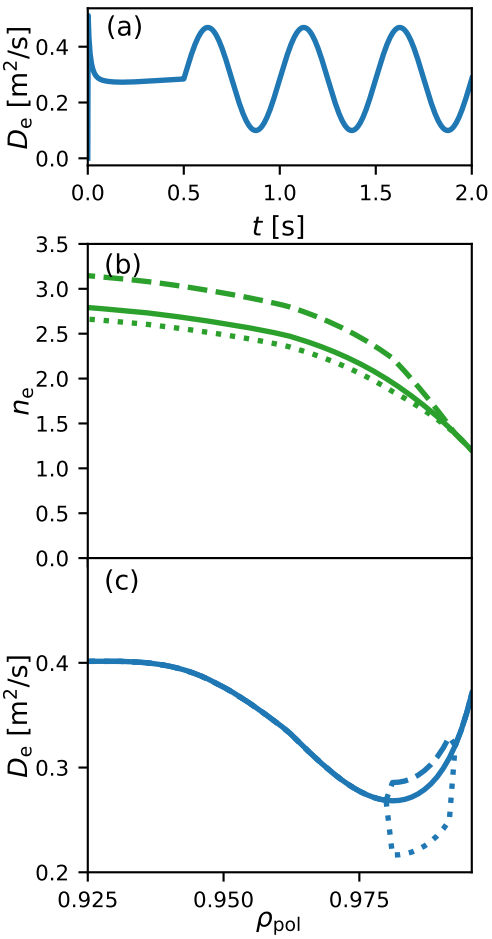

Figure 4.3: (a) Time trace of the electron diffusion at $\rho_\mathrm{pol} = 0.97$. Radial profiles of the electron density (b) and electron diffusion (c) for the reference just before the application of the diffusion modulation at $t = 0.5\,\mathrm{s}$ (solid) and at two different times within the modulation phase (dashed and dotted).

Thomson scattering system is also minimized.

A comparison of the resulting phase and amplitude profiles to the experimental results of section 4.2 is shown in figures 4.4(a) and (b), respectively. By definition the amplitude and phase of the ASTRA simulation results fit well to the two outermost channels of the core Thomson scattering system. Towards the plasma core, the phase delay as predicted by ASTRA is in good agreement with the measurement. Not only the increasing trend towards the core is reproduced, but also the absolute value. The simulation as well as the measurement show a decrease of the modulation amplitude towards the plasma core, however, in the case of the experiment the decrease less pronounced.

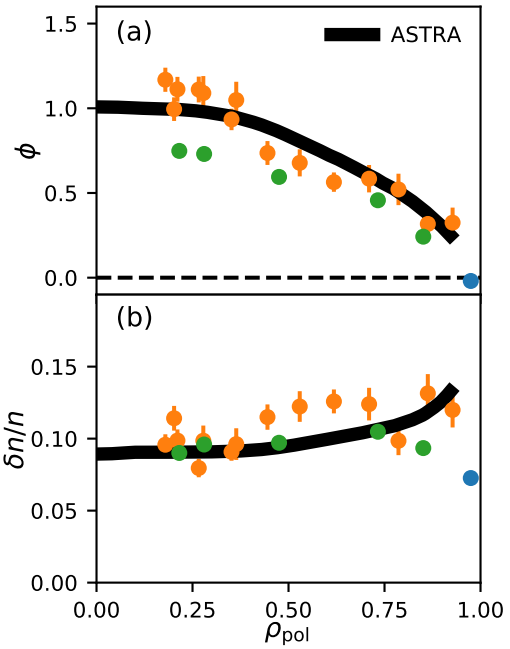

Figure 4.4: Comparison of the simulated phase (a) and amplitude (b) profile (black) to the experimental results of section 4.2.

4.4 Summary & Discussion

In this chapter, an experiment is described which aimed at shedding light on the radial localization of the increased particle transport due to radial magnetic perturbations in the ELM suppressed H-mode scenario. For this purpose, a density modulation was invoked by a modulation of the MP field amplitude. A Fourier analysis of electron density measurements shows an increase of the phase from the pedestal top towards the core of the plasma. At the pedestal top the density signal measured by Li-BES is in anti-correlation with the modulation of the MP field amplitude which is inverse to the modulation of the strength of the density pump-out. While these measurements show that the density pump-out effect originates from the edge of the plasma, it can not be distinguished whether modulations happen first at a rational surface at the pedestal top or just inside the steep gradient region due to the low radial resolution of density measurements. The results were then compared to an ASTRA simulation, in which the density modulation was invoked by a modulated electron diffusivity in the steep gradient region close to the pedestal top. As also measured, the ASTRA simulation predicts a global change of the density. Since the simulated radial phase and amplitude profiles show good agreement with the measurements, this shows that the evolution of the density profile in the plasma core can be described just by a modulation of the electron diffusion coefficient in the steep gradient region. Consequently, the agreement with the experiment demonstrates that a purely edge-localized transport modification due to the magnetic perturbations is sufficient to explain the observed 'pump-out' effect.

Chapter 5

Importance of the Electric and Electron Resonance at the Pedestal Top

When magnetic perturbations (MPs) penetrate the plasma, magnetic flux surfaces and also the equipotential field lines can get distorted. This in turn can lead to increased radial neoclassical transport. However, resonant magnetic perturbations are usually shielded by helical currents induced in the plasma, except for a narrow region around the separatrix. In [81], ASDEX Upgrade discharges were analyzed using a model to describe the interaction between the plasma and the magnetic perturbations as well as calculating the resulting neoclassical transport coefficients. This model suggests an important role of fluid and particle resonances for the penetration of the MP field and, consequently, for the enhanced neoclassical transport induced by the magnetic perturbations. These resonances and accompanying transport is described briefly in section 5.1. The model predicts clear transport changes at resonances, which should be possible to be identified in the experiment (section 5.2). The experimental results are then discussed in section 5.3.

As a consequence, radial transport increases not only by parallel particle motion along the perturbed magnetic field lines, but also due to ExB drifts.

5.1 The Model

The quasi-linear kinetic model explained in [81] describes the effect of a magnetic perturbation field on neoclassical transport in a cylindrical plasma. Therein, the quasi-linear transport equations are derived from gyrokinetic equations. Linear [82, ?] and quasi-linear [83] kinetic models are used to calculate the currents as a response of the plasma to the magnetic perturbation field, which is needed in order to describe the total magnetic perturbation field relevant for the calculation of the transport coefficients. In this model, two resonances have been identified during an analytical scan of the toroidal plasma rotation at which shielding is significantly reduced (see figure 10 in [81]). Consequently, the magnetic perturbation field can penetrate to the corresponding resonant surface and can lead to a local increase of radial transport at this layer (see figure 11 in [81]). The first resonance is called the electron resonance and occurs when the zero crossing of the perpendicular electron velocity $v_{\mathrm{e},\perp}$, referred to as its reversal point, is overlapping with a surface resonant to the magnetic perturbation field. A magnetic surface with safety factor q is resonant to a magnetic perturbation field with a toroidal mode number n and poloidal mode number m, when $q = m/n$ is fulfilled.

$$\text{Electron resonance:} \quad v_{\mathrm{e},\perp} = 0 \quad \text{at} \quad q = m/n \tag{5.1}$$

Here, a strong reduction of the plasma shielding is observed and the amplitude of the resonant magnetic perturbation field increases towards its vacuum prediction. This resonance has already been found in 2-fluid MHD calculations [84]. In the case of the electron resonance, the enhanced transport is mainly due to the parallel motion of particles along the distorted magnetic field lines (see figure 11 (a) and (b) in [81]). In this model another resonance is observed when the reversal point of the radial electric field E_{r} is overlapping with a resonant surface, called the electric resonance.

$$\text{Electric resonance:} \quad E_{\mathrm{r}} = 0 \quad \text{at} \quad q = m/n \tag{5.2}$$

Indeed, the radial magnetic perturbation field can even be amplified above the vacuum level at the electric resonance. In addition to the transport parallel to the field lines, in the case of the electric resonance also convective transport related to ExB drifts can occur (see figure 11 (c) in [81]). The reason is that distorted equipotential lines lead to a poloidal electric field, which, crossed with the toroidal magnetic field component, causes a radial ExB drift. Furthermore, at the electric resonance, the $E_{\mathrm{r}} \times B$ poloidal drift as a decorrelation mechanism between particles and the perturbation fields is absent.

As a consequence of one of the two resonances, the density profile around the corresponding resonant surface is expected to flatten. Since the inward particle pinch is not expected to change and the particle source is mainly outside the plasma, density core profiles in the investigated discharges are typically rather flat. Then such a local flattening at the pedestal top or in the steep gradient region would also lead to a decrease of the density further inward of the flattened region. This effect is illustrated in figure 5.1. The solid profile refers to an unperturbed case, while the

dashed profile could result from a complete flattening in the pedestal top region and the dotted profile from a complete flattening in the steep gradient region. In a tokamak, the perpendicular electron velocity is the sum of the radial ExB velocity and the diamagnetic electron velocity. Since usual pressure profiles are monotonously decreasing from the core to the edge, the position of the perpendicular electron velocity reversal is consequently always located further inward from the radial electric field reversal point for the discharges investigated in this thesis.

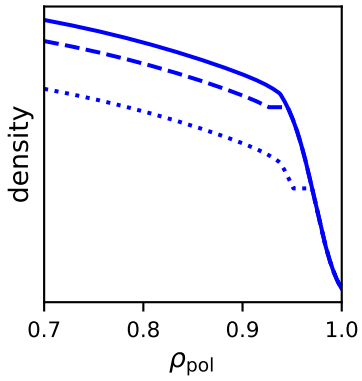

Figure 5.1: Schematic density profile in the unperturbed case (solid) and in the presence of a magnetic island at the pedestal top (dashed) or in the steep gradient region (dotted).

5.2 Experimental Test

5.2.1 Approach: Safety Factor Scan

In order to examine whether the electron and/or electrical resonances (see equation 5.1 and 5.2) can be observed in experiments, we designed discharges in which resonant surfaces and resonance locations are shifted radially with respect to each other as a function of time. The importance of these resonances can be assessed by changes in the observed electron density when crossing through the resonances. According to the model, a stronger pump-out, i. e. lower electron density, is expected when a resonance condition is fulfilled. The suggested experimental scans through the resonances can be approached in two ways:

1. Modifying the radial electric field or perpendicular electron velocity profile, while keeping the resonant surface locations unchanged. This implies a constant edge safety factor.

2. Modifying the resonant surface locations, by changing the edge safety factor, while keeping the radial electric field or perpendicular electron velocity profile unchanged.

Even though it is possible to change the E_r and $v_{\mathrm{e},\perp}$ profiles, e. g. by varying the plasma rotation, the positions of their reversal points cannot be moved reliably over a significant range. Therefore, we choose the second approach using a variation of the edge safety factor. The goal was to modify the equilibrium during the discharge in such a way that resonant surfaces are moved through the fixed electron flow and ExB reversal points, hence, turning on and off the resonance condition. This can be achieved by a variation of the edge safety factor q_{95} during a plasma current ramp controlled by the OH-transformer. Since the differential phase angle $\Delta\phi$ of the perturbation field required for an optimal plasma response and pump-out depends on q_{95}, $\Delta\phi$ was adjusted continuously during the scan in order to maintain the same condition for the density pump-out. The prediction for the optimal $\Delta\phi$ uses the empirical parametrization according to [43]. As explained in section 2.1, the toroidal mode number of the perturbation field can be set very precisely while the poloidal mode number exhibits a rather broad spectrum. As a consequence, several magnetic surfaces resonant to the magnetic perturbation exist in the pedestal top and edge region.

Since the determination of the radial localization of the reversal points contains uncertainties and the intervals in between rational surfaces crossing resonances should not be shorter than a typical particle confinement time in order to observe a recovery of the density profile, resonant surfaces should be separated radially as far as possible. On the one hand, the radial distance between resonant surfaces can be controlled by the safety factor. The lower the safety factor, the further away are resonant surfaces located from each other. On the other hand, the number of resonant surfaces in a given safety factor q profile is defined by the structure of the perturbation field. The least amount of rational

surfaces is reached for a perturbation field with a toroidal mode number of $n = 1$. In this case, the resonant surfaces are just integers $q = {}^{m}/_{n} = 1, 2, 3, 4...$ corresponding to the poloidal modes $m = 1, 2, 3, 4...$ of the perturbation field and, hence, they are furthest away from each other. Unfortunately, $n = 1$ magnetic perturbation fields at ASDEX Upgrade are found to be very likely to also trigger $m = 2$ $n = 1$ locked modes in the plasma core. These are non-rotating magnetic islands, which can be disruptive and should, therefore, be avoided. For that reason, an ELM mitigation scenario (see section 3.1) at higher values of the edge safety factor operating at $B_\phi = 2.5\,\mathrm{T}$ was chosen, since this scenario is less prone to locked modes. At $B_\phi = 2.5\,\mathrm{T}$, two plasma current ramps have been performed in two separate discharges (see figure 5.2) covering the range of $q_{95} = 4.6$ to 6.6. The operation in the ELM mitigation scenario (see section 3.1) rather than the ELM suppression scenario is preferred due to the wider range of accessible q_{95}. The separation into two discharges is favorable in order to allow for slower plasma current ramps which means longer phases without a resonance and more time for the density to adjust. After the ramp-up, the magnetic perturbation coils were switched on and the gas puff was reduced to a lower level. Keeping some gas puff helps to avoid locked modes. The fueling rate as well as the different heating powers were kept steady during the q_{95} scans to ensure that changes in density are just related to the magnetic perturbations. In addition to the deuterium puff, also a small nitrogen puff was applied in order to ensure good CXRS signals used for the calculation of the E_r profile. The magnetic perturbations lead to a weak mitigation of ELMs as indicated by the small decrease of the spike height in the I_div signal. During the increasing plasma current ramps the density and ELM size increase. After the initial pump-out due to the magnetic perturbations at $t = 2.0\,\mathrm{s}$, the plasma current ramps started in both discharges at $t = 2.5\,\mathrm{s}$. Together, the current ramps from 0.8 MA to 0.95 MA and from 0.65 MA to 0.85 MA cover the q_{95} range from 4.6 to 6.6. figure 5.4 shows the positions of the surfaces resonant to the $n = 1$ magnetic perturbation field close to the pedestal top with respect to the density profile at the start (solid, $t = 2.45\,\mathrm{s}$) and end (dashed, $t = 5.4\,\mathrm{s}$ and 6.15 s for #34381 and #34385, respectively) of each current ramp. In #34381 (left), the $q = 5$ surface is at the pedestal top at the beginning of the ramp and subsequently it moves further out into the gradient region. Meanwhile the $q = 4$ surface moves towards the pedestal top. Then this discharge was stopped prematurely by the plasma controller, detecting an $m = 2$ $n = 1$ locked mode. In #34385 (right), it is the $q = 6$ surface which is at the pedestal top in the beginning. During the discharge the $q = 5$ surface moves through the pedestal top and in the end it is the $q = 4$ surface, which is located at the pedestal top. Poloidal mode spectra of the $n = 1$ perturbation field are shown in figure 5.3 for the relevant magnetic flux surfaces with $q = 4$, 5 and 6. These data were taken at $t = 3\,\mathrm{s}$ during #34381 and do not include the plasma response. The vacuum poloidal spectra for the $n = 1$ main component in figure 5.3 show that $m = 4$, $m = 5$ and $m = 6$ modes are simultaneously produced at the corresponding resonant surfaces, so that tearing must be expected if shielding conditions at either of these surfaces are lost. While this is just data for one time during one of the scans, the situation does not vary significantly throughout the performed scans. In figure 5.5 the E_r profiles for #34381 (top) and #34385 (bottom) measured with CXRS are shown across the whole plasma on the left; the plots

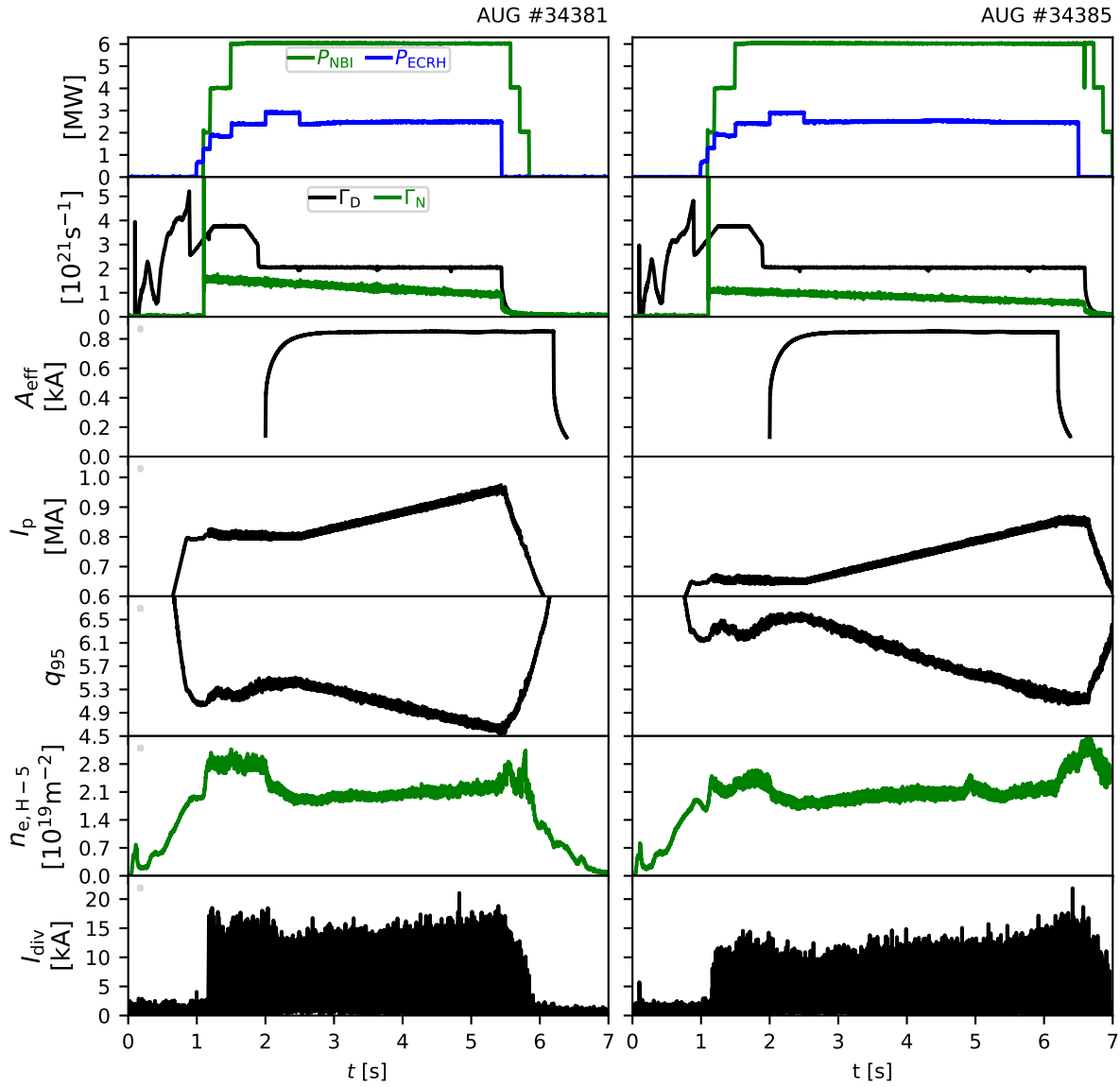

Figure 5.2: Time traces of the Neutral Beam Injection P_{NBI} and Electron Cyclotron Resonance P_{ECRH} heating power, the deuterium Γ_{D} and nitrogen Γ_{N} gas puffing rates, the effective $n = 1$ MP coil current amplitude A_{eff}, the plasma current I_{p}, the edge safety factor q_{95}, the line-integrated electron edge density $n_{\mathrm{e,H-5}}$ and the outer divertor shunt current I_{div}.

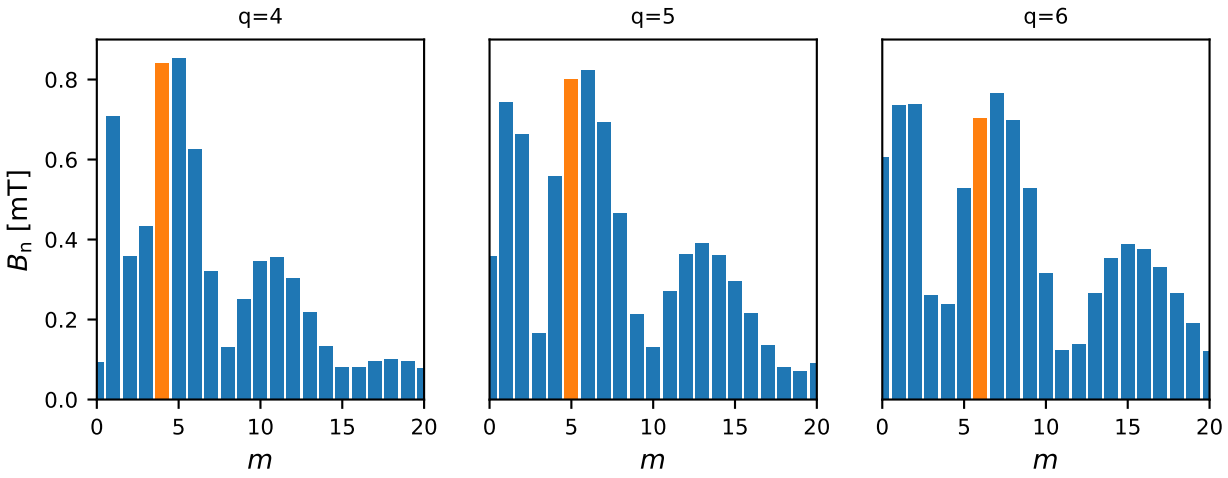

Figure 5.3: Poloidal spectrum of the magnetic perturbation field at $q = 4$, $q = 5$ and $q = 6$ surfaces located at the pedestal top region. The resonant component is highlighted in orange.

on the right are zoomed in around the E_r reversal point. The abrupt change in smoothness and uncertainties seen for each profile at around $\rho_{pol} = 0.945$ is due to the change from the core to the edge CXRS system. For both discharges, four exemplary time points during the q_{95} scan are shown. A slight increase of E_r during the time of the scan can be observed in the core region.
However, in the edge region the calculated profiles stay constant within the error bars. This implies that the E_r reversal point stays at about the same position during the q_{95} scan, which is in both discharges at around $\rho_{pol} = 0.95 - 0.975$. As compared to the density profiles in figure 5.4, the E_r reversal point is located in the upper half of the gradient region or the pedestal top. Hence, the goal to design discharges in which the E_r reversal point stays at the same location while resonant surfaces are moved through the pedestal top region, was achieved.

5.2.2 Results

In order to identify changes in the particle transport possibly induced by the movement of resonant surfaces through the reversal points, one can search for sudden changes in the time evolution of the electron density. The line-integrated electron density measurements by the different DCN interferometry channels are shown in figure 5.6 during the q_{95} scans. Here, green traces refer to the discharges with MPs and black to their reference without MPs. All density traces are congruent up until $t = 2.0\,s$, which is when the MPs were switched on and the density pump-out set in. As seen in the q_{95} scan on the right, after switching off the MPs at $t = 6.2\,s$, the density in the MP and reference case match again. On a slow time scale the density increases in all discharges due to the ascending plasma current ramps. The only sudden change can be observed in #34385 at $t = 4.8\,s$. However, at this very time an impurity event occurs. Figure 5.7 shows two consecutive frames of a visible light camera inside the vessel illustrating this event. In the first frame, an impurity

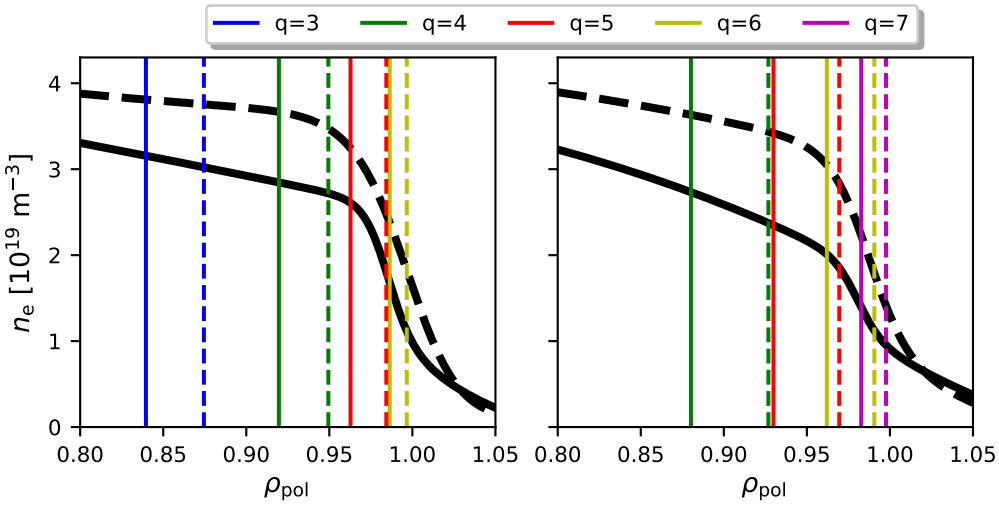

Figure 5.4: Profiles of the electron density (black) and locations of rational surfaces for #34381 (left) and #34385 (right). Solid lines correspond to the beginning of the current ramp at $t = 2.45\,\mathrm{s}$, dashed lines to its end at $t = 5.4\,\mathrm{s}$ and $6.15\,\mathrm{s}$ for #34381 and #34385, respectively.

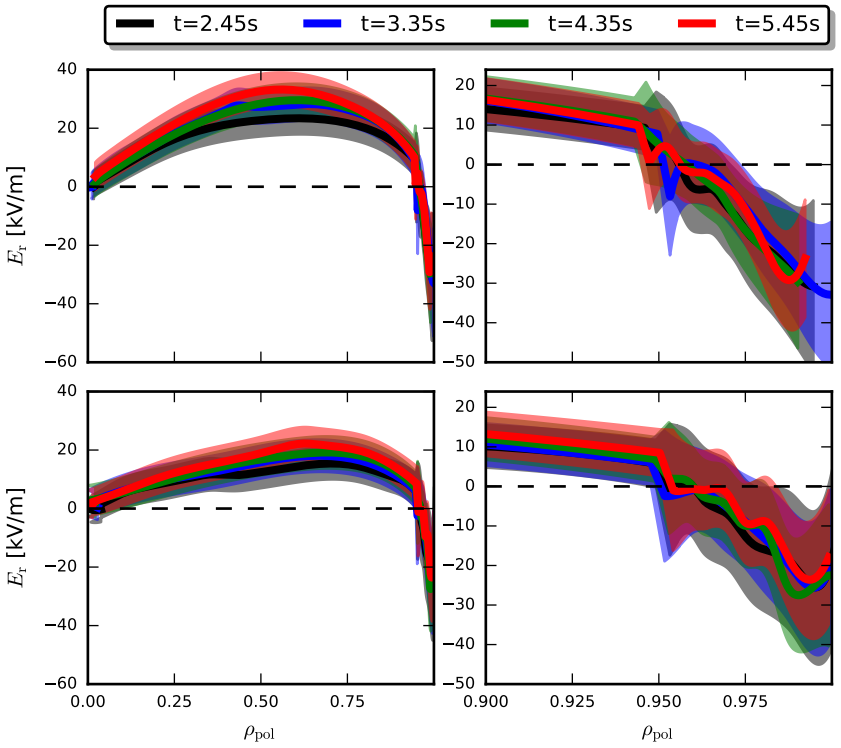

Figure 5.5: Profiles of the radial electric field E_r different times during #34381 (top) and #34385 (bottom) as measured by CXRS. The plots on the right side show zoom-ins around the E_r reversal point.

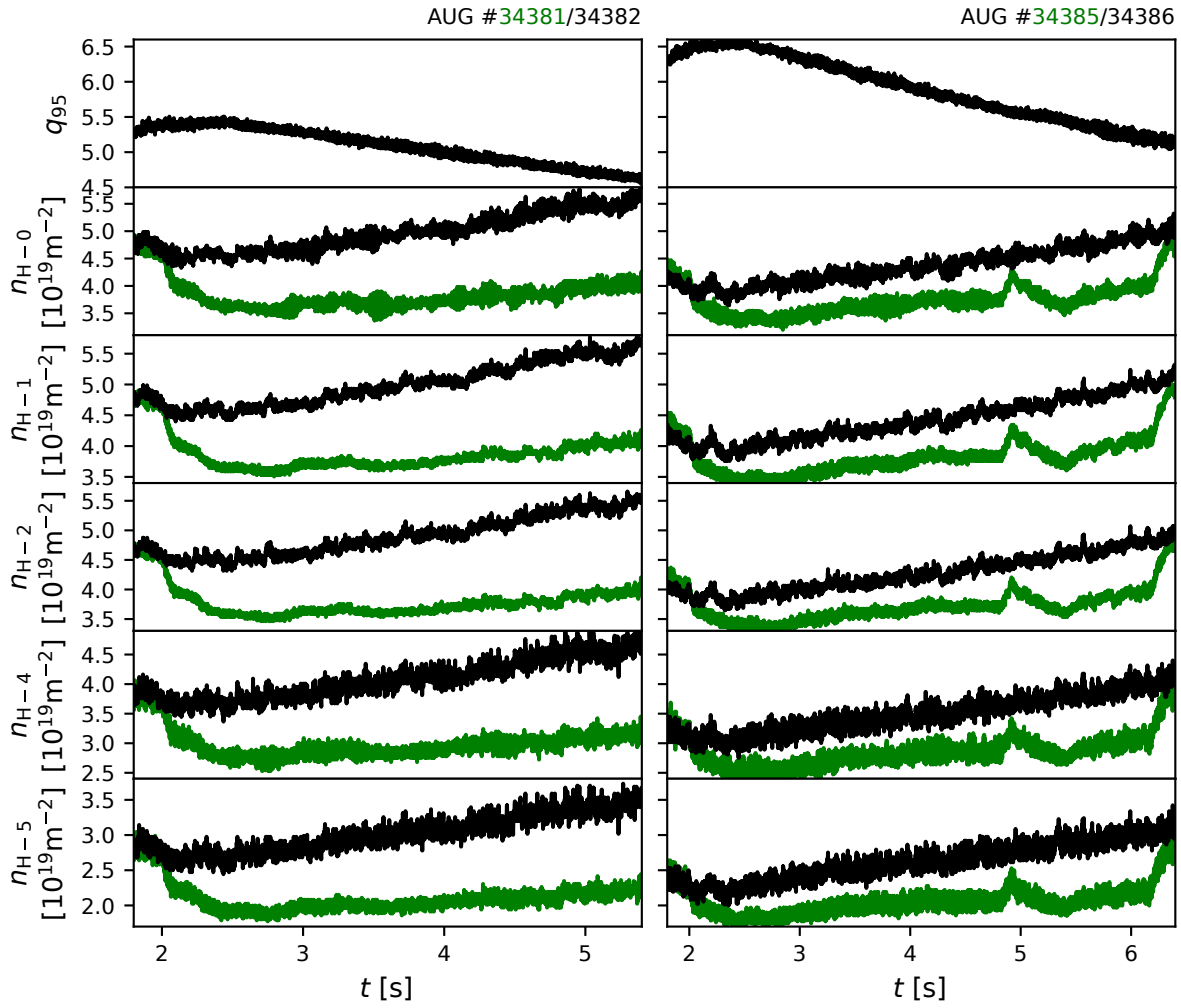

Figure 5.6: Time traces of the edge safety factor q_{95} and the different line of sights of the line-integrated electron density ranging from the core $n_{\mathrm{H}-0}$ to close to the pedestal top $n_{\mathrm{H}-5}$. The density is shown for both, the discharge with MPs (green) and their reference without MPs (black).

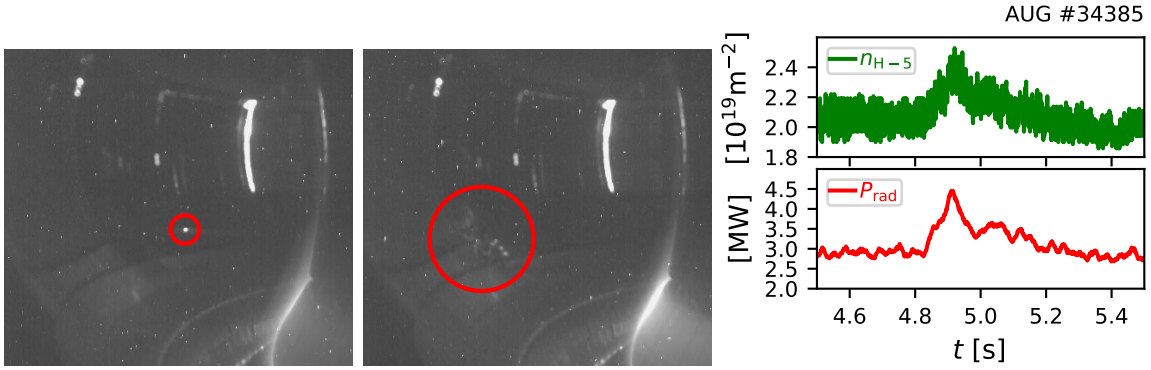

Figure 5.7: Left: Picture from inside the vessel at $t = 4.813\,\mathrm{s}$ with an encircled impurity flake. Middle: Same picture at $t = 4.846\,\mathrm{s}$ showing the flake hitting the vessel. Right: Time traces of the line-integrated electron density at the pedestal top $n_{\mathrm{H}-5}$ and the total radiated power P_{rad}.

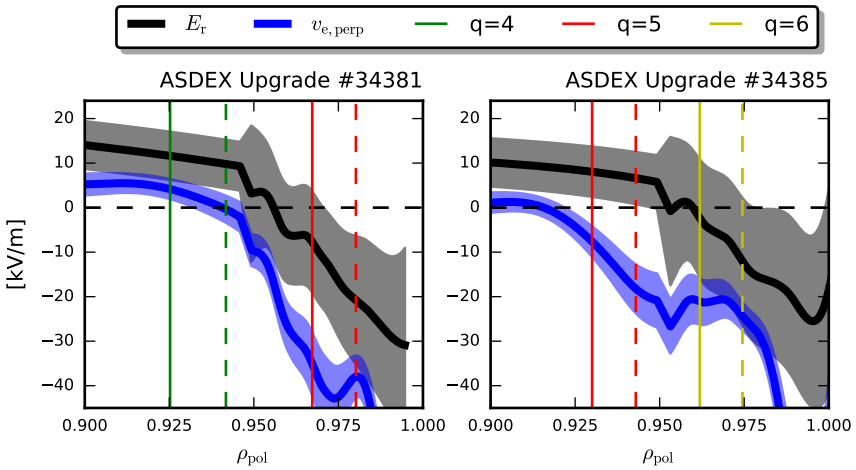

Figure 5.8: Profiles of the radial electric field E_r and the perpendicular electron velocity times the magnetic field $v_{e,\perp} \cdot B$. The data is averaged over the whole duration of the q_{95} scan. The solid lines correspond to the positions of the resonant surfaces at $t = 3.05\,s$ and $t = 2.75\,s$, the dashed lines at $t = 4.75\,s$ and $t = 3.75\,s$ for #34381 and #34385, respectively.

flake coming from an antenna is encircled. In the second frame, the flake hits the vessel and shatters. At the same time the electron density in the confined plasma increased and the total radiated power showed a distinct peak. Therefore, this event can be attributed to impurities entering the confined plasma rather than to a loss of the resonance condition and the subsequent loss of density pump-out. Other than that, no significant changes in the density evolution can be observed.

In figure 5.8 the $v_{e,\perp} \cdot B$ and E_r profiles are shown averaged over the full duration of each q_{95} scan as well as the position of resonant surfaces near the pedestal top. In #34381 at $t = 3.05\,s$ the rational surfaces are as far away as possible from the zero crossing of either $v_{e,\perp}$ or E_r. Later at $t = 4.75\,s$ the $q = 4$ surface overlaps nicely with the $v_{e,\perp}$ reversal point. Sighting these time points in figure 5.2, in both situations the density is way below the reference density implying a strong pump-out effect and around these times also no change in the temporal density gradient, which could be connected to a movement through the resonance condition, can be seen. In #34385 at $t = 2.45\,s$ the $q = 6$ surface overlaps with the E_r reversal point, while at $t = 3.75\,s$ no surface is overlapping with either reversal point. Again, figure 5.2 shows a distinct density pump-out throughout the whole scan and no sudden changes in the electron density evolution can be seen around these times.

5.3 Summary & Discussion

When magnetic perturbations penetrate the plasma at the radial position, where the reversal point of the perpendicular electron velocity or of the radial electric field overlaps with a surface resonant to the perturbation field, magnetic field lines and equipotential lines can become perturbed. Consequently, parallel transport along the disturbed magnetic field lines and convective transport due to radial $E \times B$ drifts can increase. In this chapter, the significance of these effects for the density pump-out has been investigated.

The approach for testing the electric and electron resonance was to keep the position of the reversal points constant during a discharge, in which the resonant surfaces were moved through those reversal points via a q_{95} scan. Such conditions were achieved in two discharges in the range from $q_{95} = 4.6$ to 6.6. In the range covered by the scan, a significant density pump-out was always present when compared to reference discharges without magnetic perturbations. The amount of density pump-out appears to be independent of whether a resonance condition was fulfilled or not. In addition, no significant changes in the time derivative of the density measurements are obvious when a resonant surface moved through one of the two reversal points. The conclusion is that either the investigated effects do not contribute significantly to the pump-out effect, or the resonance condition was never lost during the q_{95} scans. The latter could be due to the resonant surfaces being always close to each other at the pedestal top combined with the flat profiles of perpendicular electron velocity and radial electric field around the reversal points. However, the measurements do not indicate any movements of the reversal points, e. g. following the resonant surfaces. Such a clamping of a reversal point to a resonant surface would become apparent when the resonant surface moves into the gradient region during the q_{95} scan. Either a deformation of the density profile should be observed or a sudden jump of the reversal point to the next resonant surface arriving at the pedestal top. Neither can be seen in the experiment.

Chapter 6

Experimental Observations of Plasma Edge Turbulence during ELM Suppression

In this chapter, experimental observation of turbulence in the steep gradient region during ELM suppression are discussed especially with respect to potential toroidal asymmetries. Therefore, a helical field-line label α is introduced in section 6.1, which serves as a coordinate defining the location of a measurement inside the surface corrugation pattern.

As shown in section 6.2, broadband density fluctuations can be observed during ELM suppression. Their appearance is linked to the presence of the magnetic perturbation field, hence, the fluctuation level drops significantly when the perturbation is switched off. A comparison of these density fluctuation measurements with the appearance of a density shoulder in the scrape-off layer as well as fluctuation measurements with Langmuir probes in the outer divertor is presented in section 6.2.2.

Furthermore, a quasi-coherent mode can be observed in ELM suppression at high perturbation amplitudes (see section 6.3). The radial and toroidal localization of the mode is shown in section 6.3.1 and section 6.3.2, respectively. The transitions between the quasi-coherent mode and broadband fluctuations can be observed when the MP field amplitude is alternated as shown in section 6.4. During the discharges dedicated to characterize the quasi-coherent mode, the polarity of the current in one of the 16 magnetic perturbation coils was unintentionally inverted. This applies to the coil *Bl5* (see figure 2.3) for all discharges between #35045 and #36793. The result is a spectral leakage from the $n = 2$ perturbation desired in these discharges into an $n = 1$ component. Since the quasi-coherent mode has been observed in past discharges without the MP coil current inversion, the small $n = 1$ perturbation overlapping the $n = 2$ perturbation is not necessary for the existence of the quasi-coherent mode. If consequences of the MP coil current inversion arise for the investigation of the different properties of the quasi-coherent, these consequence are discussed in the respective section.

Due to the toroidal localization of the measured fluctuations in the surface corrugation

pattern, also the toroidal dependency of turbulence driving and stabilizing quantities are investigated in section 6.5. A summary and discussion of the observations on edge turbulence presented in this chapter can be found in section 6.6.

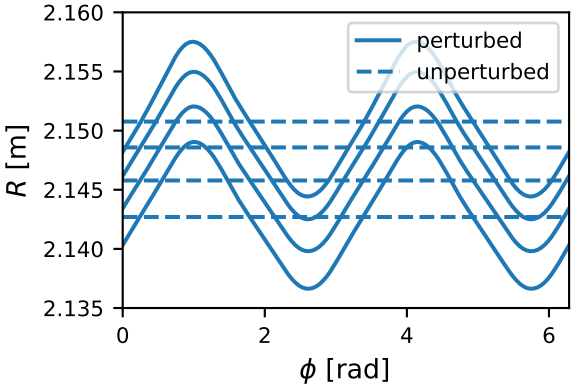

Figure 6.1: Illustration of the surface displacement in a top view as caused by radial magnetic perturbations.

6.1 Helical Field-Line Label α

The application of a radial magnetic perturbation field disturbs the magnetic equilibrium of a plasma. Radial perturbations can either push or pull on magnetic flux surfaces and, hence, these perturbed flux surfaces experience a displacement from the unperturbed flux surfaces. This is illustrated in figure 6.1, which shows the line of intersection of undisturbed (dashed) and disturbed flux surfaces (solid) with the midplane. Such a displacement can alter e. g. the curvature and magnetic shear, and as a consequence locally influence the stability properties of the magnetic equilibrium as shown in [85, 86]. In this thesis, the investigation of toroidal asymmetries during rigid rotations of an applied radial magnetic perturbation field is one major object and, therefore, it is advantageous to define a coordinate with respect to the MP induced displacement of the magnetic flux surfaces.

In the following, a straight field-line coordinate system with the poloidal θ^* and toroidal ϕ^* angle is used (as described in [87] and the references therein). While the toroidal angle ϕ^* stays the geometrical ϕ in this coordinate system, the poloidal angle θ^* is determined from the geometrical θ. It was shown in [87], that the radial displacement at the edge of the plasma is strongly pitch-aligned even in cases where the magnetic perturbation field is not. Therefore, a field-line on a certain flux surface stays approximately in the same phase with respect to the surface corrugation and, hence, the safety factor q can be used as an approximation for the inclination of the surface displacement in the θ^* - ϕ plane. The helical field-line label α is then defined as

$$\alpha = \theta^* \cdot q + \phi \tag{6.1}$$

In this definition of α, an arbitrary offset in ϕ can be chosen and this freedom can be used in order to align e. g. $\alpha = 0$ with a certain phase of the surface corrugation. Therefore, a measurement or prediction of the surface corrugation is necessary. In the following subsection, a comparison between the surface corrugation as measured with the Li-BES diagnostic and the surface corrugation as predicted by VMEC is made.

6.1.1 Comparison of Measured Surface Corrugation with VMEC

In an experiment using a rigid rotation of the MP coil current pattern, the corrugation of the plasma surface can be seen in several profiles diagnostics on the LFS as a radial shift of their profile at different times, which correspond to different toroidal observation angles in the frame of the perturbation field. In addition, the surface corrugation can also be calculated from the predicted 3D VMEC equilibrium.

In #34548 (see figure 6.2), the MP coils were powered at $t = 1.5\,\mathrm{s}$ with a pattern as commonly used for ELM suppression, i. e. $n = 2$, $\Delta\phi = 90\,^\circ$ and maximum amplitude. After reaching full ELM suppression at $t = 2.7\,\mathrm{s}$ - as recognized by the disappearance of the pronounced spikes in I_{div} - the differential phase $\Delta\phi$ was increased to $135\,^\circ$ at $t = 3.0\,\mathrm{s}$. At the same time, the rigid rotation of the MP coil current pattern began with a frequency of $0.5\,\mathrm{Hz}$ in anti-clockwise direction, as seen from above the torus. Lasting up until $t = 7\,\mathrm{s}$, two full rotation periods are achieved with constant ELM suppression. In the first period from $t = 3 - 5\,\mathrm{s}$, the $n = 2$ MP field amplitude is slightly higher than in the second period from $t = 5 - 7\,\mathrm{s}$. The density shows the distinct density pump-out during the phase with the magnetic perturbation field and the recovery of the plasma density when the perturbation is switched off at $t = 7\,\mathrm{s}$. During the rotation phase the density shows a slow increase by roughly 10 % over the full duration. This is often observed during ELM suppression with reduced MP field amplitude, which is the case during a rotation of the MP field. Except for a short phase directly after entering ELM suppression, both, the ion and electron temperatures stay reasonably constant. In figure 6.3(a) density profiles from Li-BES are shown for three different time points during the first period of the rigid rotation. Tracking the radial position of a fixed separatrix electron density of $1.2 \cdot 10^{19}\mathrm{m}^{-3}$ during the rigid rotation gives the radial surface displacement as a function of time, revealing the corrugation of the plasma surface (see figure 6.3(b)). The measured separatrix position as a function can include higher

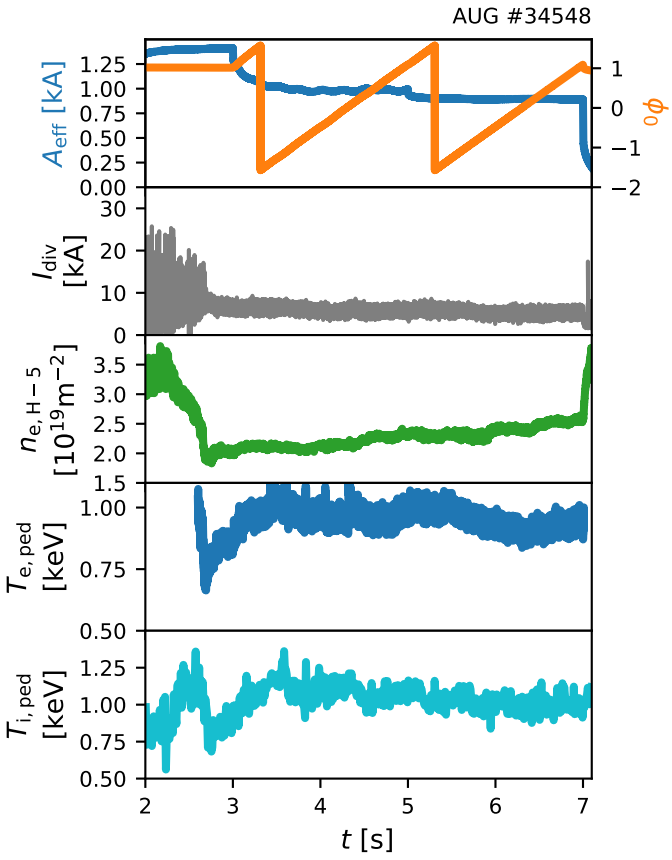

Figure 6.2: Time traces of the effective $n = 2$ MP coil current amplitude A_{eff}, the toroidal angle ϕ_0, the divertor shunt current measurement I_{div} as well as the line-integrated electron density $n_{\mathrm{e,H-5}}$, electron temperature $T_{\mathrm{e,ped}}$ and ion temperature $T_{\mathrm{i,ped}}$ close at the pedestal top.

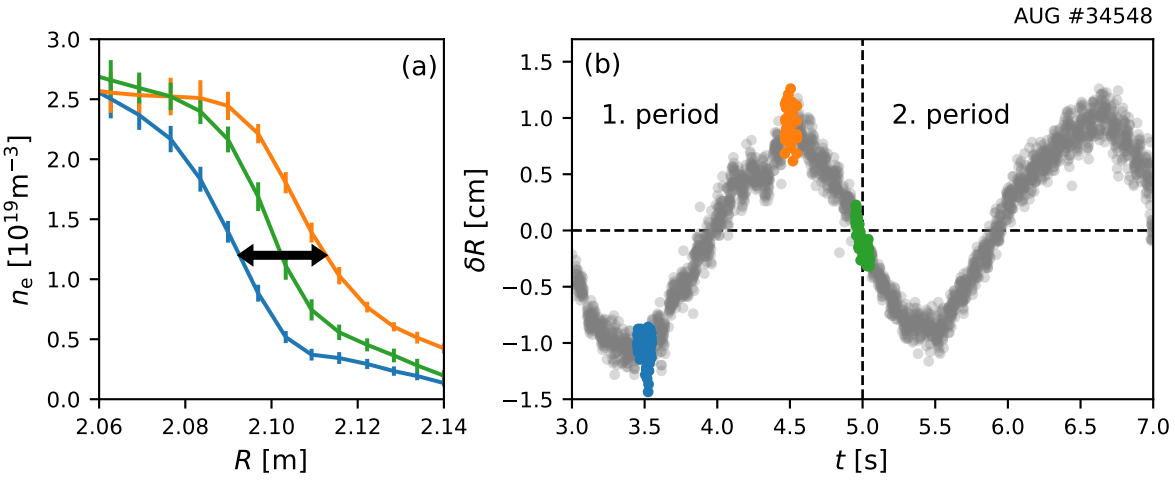

Figure 6.3: (a) Electron density n_e profiles from the Li-BES diagnostic at three different times (colors) during a rigid rotation of the magnetic perturbation field. (b) Radial displacement δR of the separatrix with respect to its average position during the whole scan.

harmonics as well as a non-periodic contribution due to the evolution of the density during the rigid rotation. In order to correct for these effects, the signal is fitted first by the function shown in equation 4.1. This fit is shown in figure 6.4 (orange, dashed). In order to compare it to the surface corrugation calculated from the VMEC equilibrium (blue), the polynomial term is neglected and just the $n = 2$ contribution (first order) of the trigonometric term is kept. This signal is then corrected for the movement due to the plasma control system (PCS) as explained in [88], the result is the orange, solid line. While the comparison in the presented discharge with ELM suppression shows good agreement in terms of amplitude ($\delta R \approx 0.75\,\mathrm{cm}$), there remains a time delay of roughly 55 ms even after the correction for the PCS. However, this time delay corresponds to a phase offset of only $0.055\,\pi$, i. e. 2.25 %, which is of the order of possible uncertainties within the correction for the plasma control system. Small uncertainties may arise on the side of the measured corrugation due to non-stationary density, determination of the separatrix density and the arbitrary choice of the highest orders in the fit function for the density as well as for the PCS correction. On the side of the VMEC prediction, uncertainties may arise due to the negligence of the small contributions from eigenmodes with a high poloidal mode number close to the separatrix, since VMEC flattens and truncates the q profile at the very edge at $\rho_{\mathrm{pol}} > 0.9998$. Furthermore, the ideal MHD code VMEC does not include resistive effects such as a possible formation of magnetic islands, which may arise with the application of magnetic perturbations.

6.1.2 Definition of the Helical Field-Line Label for Rigid Rotations

The previous section showed good agreement between the surface corrugation as measured by the Li-BES diagnostic and predicted by the 3-dimensional ideal MHD equilibrium as

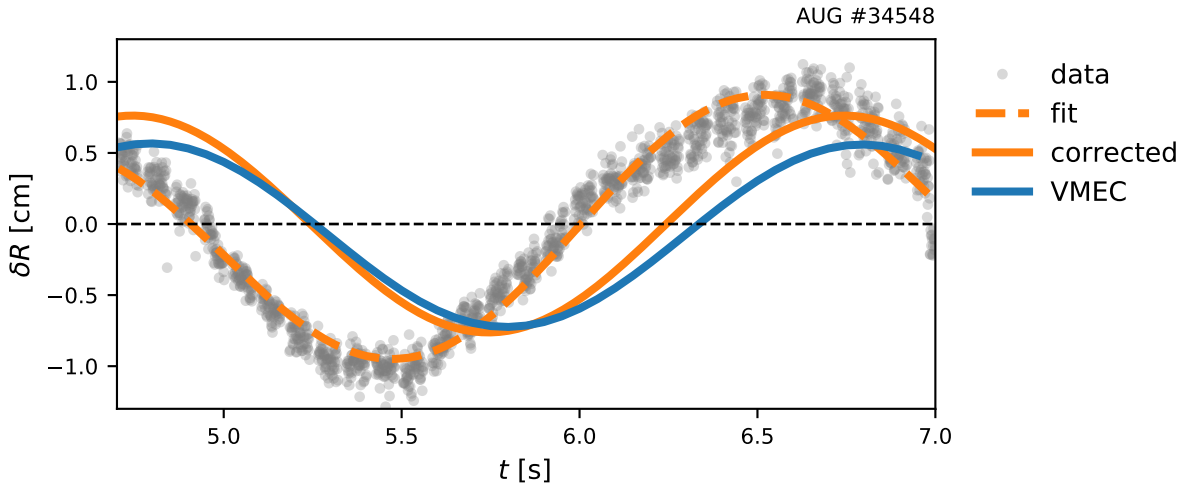

Figure 6.4: Radial displacement δR of the separatrix with respect to its average position during the whole scan. Comparison between the measured data (grey), $n = 2$ filtered (dashed orange) and PCS corrected corrugation (solid, orange) and the $n = 2$ contribution of the VMEC simulation (blue).

calculated by VMEC. The VMEC prediction of the plasma surface corrugation in the line-of-sight of the Li-BES is now used for the definition of the helical field-line label

$$\alpha = \theta^* \cdot q + \phi \tag{6.2}$$

For the rigid rotation in #34548, the toroidal angle ϕ can be expressed in terms of a time varying contribution $\phi_{\text{rot}} = \pi \cdot f_{\text{rot}} \cdot (t - t_{\text{start}})$ with the rotation frequency of the $n = 2$ perturbation field of $f_{\text{rot}} = 0.5\,\text{Hz}$, the time t and the time at the beginning of the rigid rotation $t_{\text{start}} = 3\,\text{s}$, an arbitrary offset angle ϕ_0 and the toroidal angle of the diagnostic ϕ_{diag}. Therefore, α can be written as

$$\alpha = \theta^* \cdot q + \phi_{\text{rot}} + \phi_0 + \phi_{\text{diag}} \tag{6.3}$$

and α is in the range of 0 to π for one transition through the surface corrugation. ϕ_0 is chosen such that α is equal to $0.75\,\pi$ at the minimum of the corrugation, which is in the line-of-sight of the Li-BES during the rigid rotation at $t = 5.78\,\text{s}$. Consequently, α is equal to $0.25\,\pi$ at the maximum of the corrugation and 0, $0.5\,\pi$ or π when the displacement is zero. Given the offset ϕ_0, the safety factor q and the toroidal and poloidal coordinates of a diagnostic, the time dependent measurement of this diagnostic can be mapped onto α during the rigid rotation.

Figure 6.5 shows the corrugation of the whole unfolded $\rho_{\text{pol}} = 0.97$ surface. The red dots serve as a guide for the eye for tracing the maximum of the surface displacement ξ. The black line indicates a field-line on this surface with $q = 3.56$, which crosses the corrugation maximum at the straight poloidal angle of the Li-BES diagnostic. One can see that the field-line inclination $q = 3.56$ is not parallel to the inclination of the corrugation maximum. Consequently, the use of the helical field-line label has an uncertainty, which increases further away from the straight poloidal angle where it was defined and especially

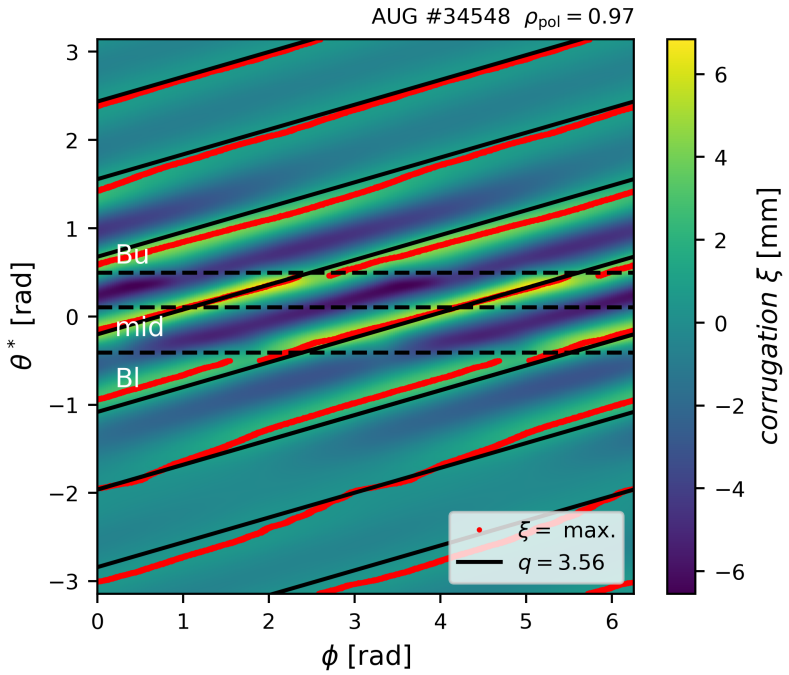

Figure 6.5: Unfolded $\rho_{\mathrm{pol}} = 0.97$ surface of #34548 with the corrugation of the surface as predicted by VMEC being color coded. The black solid lines refer to a field-line on this surface, i. e. to a trace of constant helical field-line label α. The red dots serve as a guide for the eye for the maximum of the surface corrugation. The dashed lines refer to the approximate straight poloidal angle of the lower (Bl) and upper (Bu) MP coils as well as the midplane (mid).

outside the straight poloidal angle range on the LFS enclosed by the upper (Bu) and lower (Bl) MP coils. This uncertainty is discussed in the next section for measurements within the aforementioned range on the LFS and in a radial range of roughly $\rho_{\mathrm{pol}} = 0.95$ to 1.0.

6.1.3 Estimate of the Uncertainty in α

The first source for the slight misalignment between a field-line and a trace of constant surface displacement on any magnetic flux surface is most likely due to uncertainties in the computation of the q profile and due to the exclusion of resistive effects in VMEC, which can influence the surface corrugation, such as magnetic islands and an ergodized edge. A second source for misalignment may arise from the flattening of the q profile in VMEC with the intention of avoiding the singularity of the X-point. Therefore, VMEC neglects the effect from contributions of the perturbation field with a broad poloidal spectrum on the resonant surfaces close to the separatrix. Figure 6.6 shows the q profile as used by VMEC for #34548 with a magnification of the very edge. From $\rho_{\mathrm{pol}} = 0.9998$ outwards, the q profile is flattened and truncated at $q \approx 5.35$, and consequently all components with a poloidal mode number higher than

approximately 10 – 11 do not contribute to the surface corrugation as calculated by VMEC. Therefore, the use of α is not well defined at $\rho_{\mathrm{pol}} > 0.9998$ and might not align with the surface corrugation at all in this very narrow region. The poloidal eigenmodes resonant at $q > 5.35$ are not limited into that region but have a radial extension, which is why the surface corrugation at $\rho_{\mathrm{pol}} < 0.9998$ could also suffer to some extent from the flattening of the q profile and might lead to the misalignment.

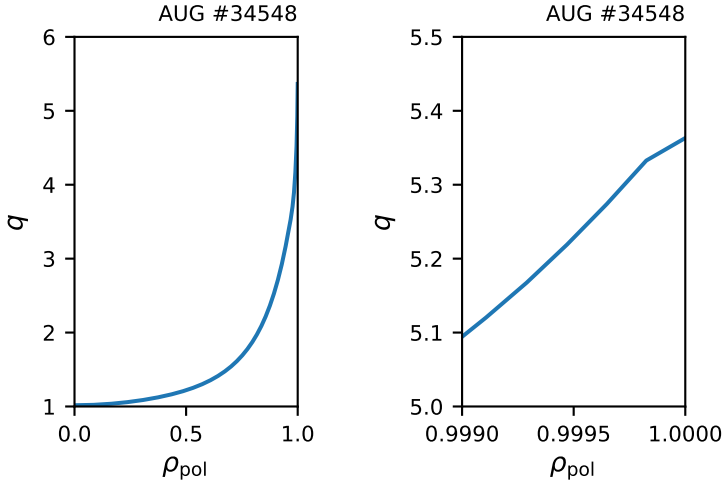

Figure 6.6: Radial profile of the safety factor q with a magnification of the very edge region, where the profile is flattened and truncated in VMEC.

The plots of the surface corrugation of the unfolded $\rho_{\mathrm{pol}} = 0.95$ and $\rho_{\mathrm{pol}} = 0.99$ surfaces in figure 6.7 focus on the LFS, where the important diagnostics are located. On the LFS, already a small range of the straight poloidal angle θ^* covers the important angular range with most diagnostics. The offset in α is defined at the line-of-sight of the Li-BES diagnostic and, therefore, the field-line with $\alpha = 0.25\,\pi$ (black line) overlays with the maximum of the surface corrugation (indicated by the red dots) in both cases. The diagnostic furthest away from the Li-BES is the Doppler reflectometry (DRFL). On the $\rho_{\mathrm{pol}} = 0.95$ surface, the misalignment at the straight poloidal angle of the DRFL amounts to $0.05\,\pi$. Even though the difference in the inclination of the field-line and the surface corrugation pattern grows slightly towards the separatrix, the misalignment at the DRFL location in the case of the $\rho_{\mathrm{pol}} = 0.99$ surface is even smaller with $0.045\,\pi$. The reason is that at flux surfaces closer to the separatrix the positions of diagnostics on the LFS are located significantly closer together in θ^*. The misalignment at the location of the conventional reflectometry (RFL) is about $0.015\,\pi$ and at the location of the edge charge exchange recombination spectroscopy system (CMZ) it is about $0.022\,\pi$ for both flux surfaces. For the purpose of the comparisons in this thesis, these uncertainties in α are negligible.

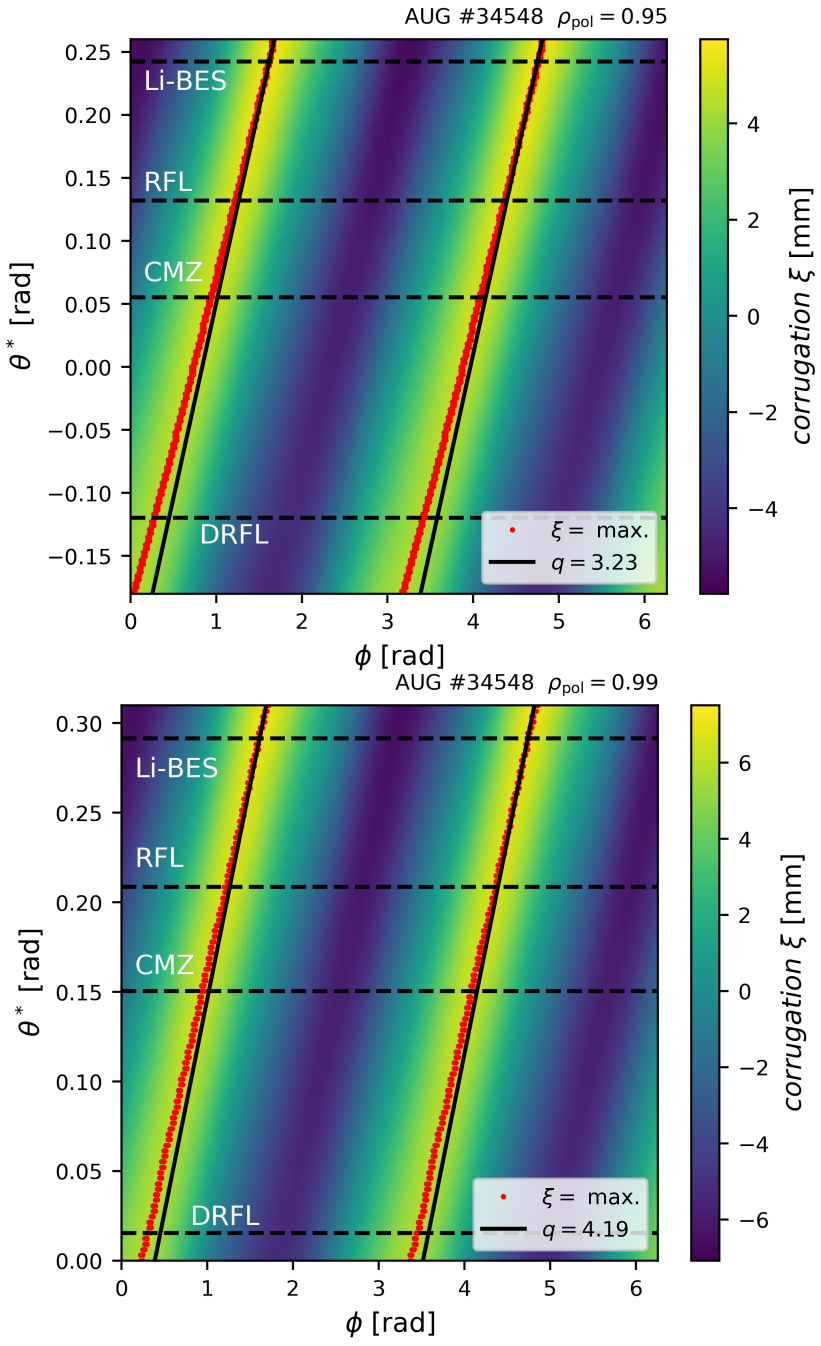

Figure 6.7: Unfolded $\rho_{\mathrm{pol}} = 0.95$ (top) and 0.99 (bottom) surfaces of #34548 with the corrugation of the surface as predicted by VMEC being color coded. The dashed lines refer to the straight poloidal angle θ^* of the correspondingly labeled diagnostic. The black solid lines refer to a field-line on this surface, i. e. to a trace of constant helical field-line label α. The red dots serve as a guide for the eye for the maximum of the surface corrugation.

6.2 Observation of Broadband Density Fluctuations

In #34548, conventional reflectometry (see section 2.2.1) has been used to measure large-scale density fluctuations. The reflectometer RF frequency for the K-band system was set to 18 GHz and for the Ka-band system to 37 GHz corresponding to a cut-off density of about $0.45 \cdot 10^{19}\mathrm{m}^{-3}$ and $1.7 \cdot 10^{19}\mathrm{m}^{-3}$, respectively. In this discharge, an $n = 2$ magnetic

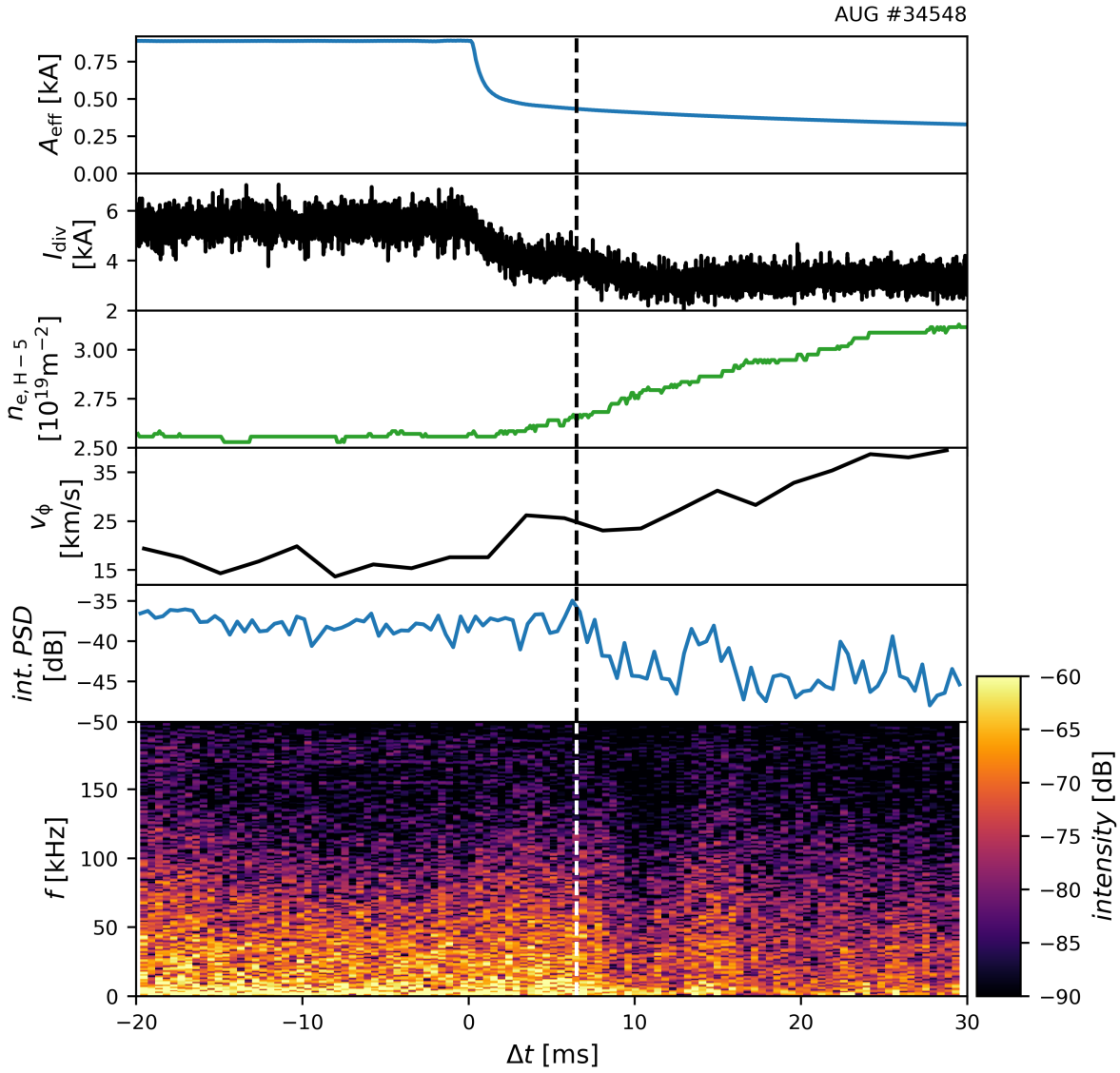

Figure 6.8: Time traces of the effective $n = 2$ MP coil current amplitude A_{eff}, the divertor shunt current I_{div}, the line-integrated electron density $n_{\mathrm{e,H-5}}$ and toroidal velocity v_ϕ of boron (B5+) impurities at the pedestal top, the integrated power spectral density PSD and the spectrogram of the conventional reflectometer Ka-band measurement with respect to $t = 7\,\mathrm{s}$, at which time the MP coils are switch off. Two distinct drops in I_{div} can be observed. The first one at $\Delta t = 0\,\mathrm{ms}$ is contemporaneous with the reduction of the MP field amplitude. The second drop at $\Delta t = 6.5\,\mathrm{ms}$ (dashed line) is contemporaneous with the reduction of broadband density fluctuations (see PSD of the reflectometer.

perturbation with a differential phase $\Delta\phi = 135\,^\circ$ was used until $t = 7\,\mathrm{s}$ in order to suppress ELMs. Figure 6.8 shows from top to bottom the effective coil current amplitude of the $n = 2$ perturbation field A_{eff}, a shunt current measurement in the divertor I_{div}, the line-integrated electron density around the pedestal top region $n_{\mathrm{e,H-5}}$, the toroidal velocity of boron (B5+) impurities at the pedestal top v_ϕ, the integrated power spectral density PSD and the spectrogram of the Ka-band reflectometry measurement as a function of Δt, which is the time with respect to the shutdown of the MP coil power supply at $t = 7\,\mathrm{s}$. Figure 6.9 shows the reflection position of the probe wave of the Ka-band system as the intersection of the horizontal line labeled 'Ka-band' with the density profile at 6.95 s just before turning off the perturbation field. It is localized in the confined region just inside the separatrix, where the electron density gradient is steep. The perturbation field shows an initial fast decay in the first 2 to 3 ms after turning off the MP coil power supply followed by a decay on a slower time scale due to the eddy currents in the PSL (as explained in section 2.1.3). As the MP coils are switched off, ELMs do not reappear immediately (first ELM occurs at $\Delta t = 56\,\mathrm{ms}$), but the plasma enters a non-stationary ELM-free regime accompanied by an increase of the electron density and toroidal velocity from $\Delta t = 0\,\mathrm{ms}$ on. The divertor shunt current, an indicator for energy transport onto the divertor, starts to decrease when the perturbation coils are switched off. This drop sets in at $\Delta t = 0\,\mathrm{ms}$ and saturates at $\Delta t = 2.5\,\mathrm{ms}$, which is when the initial decay of the perturbation field ends. From roughly $\Delta t = 6.5\,\mathrm{ms}$ until $\Delta t = 13\,\mathrm{ms}$ the shunt current drops further, resulting in a total drop of 40 %. The second drop sets in at the same time as the integrated power spectral density of the reflectometer measurement starts to decrease (dashed line). The reduction of the integrated power spectral density is ascribed to a reduction of broadband fluctuations in the range up to roughly 200 kHz. The measurement position of the Ka-band system can change slightly during the non-stationary phase due to the evolution of the electron density. In the time from $\Delta t = 0$ – 30 ms no density profile measurements are available. However, by $\Delta t = 10\,\mathrm{ms}$ the line integrated density at the pedestal top increased by 9 % and, therefore, the change of the measurement position should be negligible. Furthermore, as described in section 2.2.1, the intensity measured by reflectometry does not only depend on the density fluctuations but also on the electron density gradient at the measurement position, which increases after turning off the MP coils. However, an increase of the density gradient would lead to an increase of the reflected intensity, which contradicts the observation. Hence, the change in

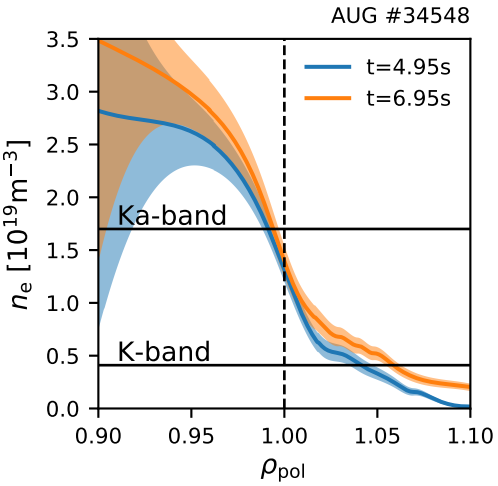

Figure 6.9: Radial electron density n_e profile as measured by Li-BES at two different times during the rotation. These refer to measurements in both periods at around the second zero crossing. The horizontal lines are at the cut-off densities for the corresponding reflectometry band. The dashed line indicates the separatrix.

reflected intensity can not be attributed to the change in the background density profile. Note that during the investigated time frame, control parameters such as toroidal magnetic field, plasma current, heating power or gas puffing were kept constant.

In section 6.1.1, the surface corrugation induced by the magnetic perturbation is compared to predictions from VMEC calculations. This allows us to study the alignment of turbulence measurements within the pattern of the surface corrugation in section 6.2.1. The surface corrugation pattern predicted by VMEC is then used to map different diagnostics on the helical field-line label α (introduced in 6.1). A comparison to density and temperature fluctuations measured by Langmuir probes (introduced in 2.2.7) in the outer divertor region and Li-BES measurements in the scrape-off layer is shown in section 6.2.2.

6.2.1 Toroidal Asymmetry

Conventional reflectometry (see section 2.2.1) has been used to measure density fluctuations during rigid rotations of the MP coil current pattern. These measurements give insight into toroidal symmetry properties of the observed density fluctuations during ELM suppression.

An advantage of the conventional reflectometry system is that it has no observation volume fixed in space, but measures at the cut-off density of the probing wave, which in O-mode does not depend on the magnetic field. Consequently, during a rigid rotation a band always measures at about the same position with respect to the moving pedestal profile (neglecting the small changes of the density profile) and, hence, can be compared directly at different times. Furthermore, since the antennas for conventional reflectometry are installed on both, the high-field side and low-field side, also the poloidal symmetry can be studied.

In #34548 (described in section 6.1.1, figure 6.2), the K-band reflectometer was operated at 18 GHz and the Ka-band at 37 GHz corresponding to a cut-off density of about $0.45 \cdot 10^{19} \mathrm{m}^{-3}$ and $1.7 \cdot 10^{19} \mathrm{m}^{-3}$, respectively. Figure 6.9 shows the density profiles as measured by Li-BES at two different times, one during the first rotation period and one during the second period. These times are equivalent in regards of their respective position in the corrugation pattern. However, the density profile changed slightly due to the small increase of the electron density during the discharge (see figure 6.2). Overlayed are the cut-off densities for the K- and Ka-bands. While the probing wave of the K-band is reflected in the scrape-off layer, the reflection of the Ka-band probe wave occurs in the confined region just inside the separatrix where the density gradient is steep. The changes in measurement position and local gradient are minor, which is why we assume that even in the presence of these changes, the reflectometry measurements at different times can be compared well with each other. In figure 6.10, the measurements of the Ka- (a) and K-band (b) systems on the LFS are shown. The plots at the top show the surface corrugation in the line-of-sight of the respective band, followed by the integrated power spectral density and its spectrogram. These quantities are presented as a function of the helical field-line label α in order to allow for a comparison between different diagnostics. The Ka-band measurement shows broadband fluctuations in the range up to 200 kHz. In both periods, the reflected intensity stays fairly constant for a long time, i. e. for a broad range in α. However, the intensity

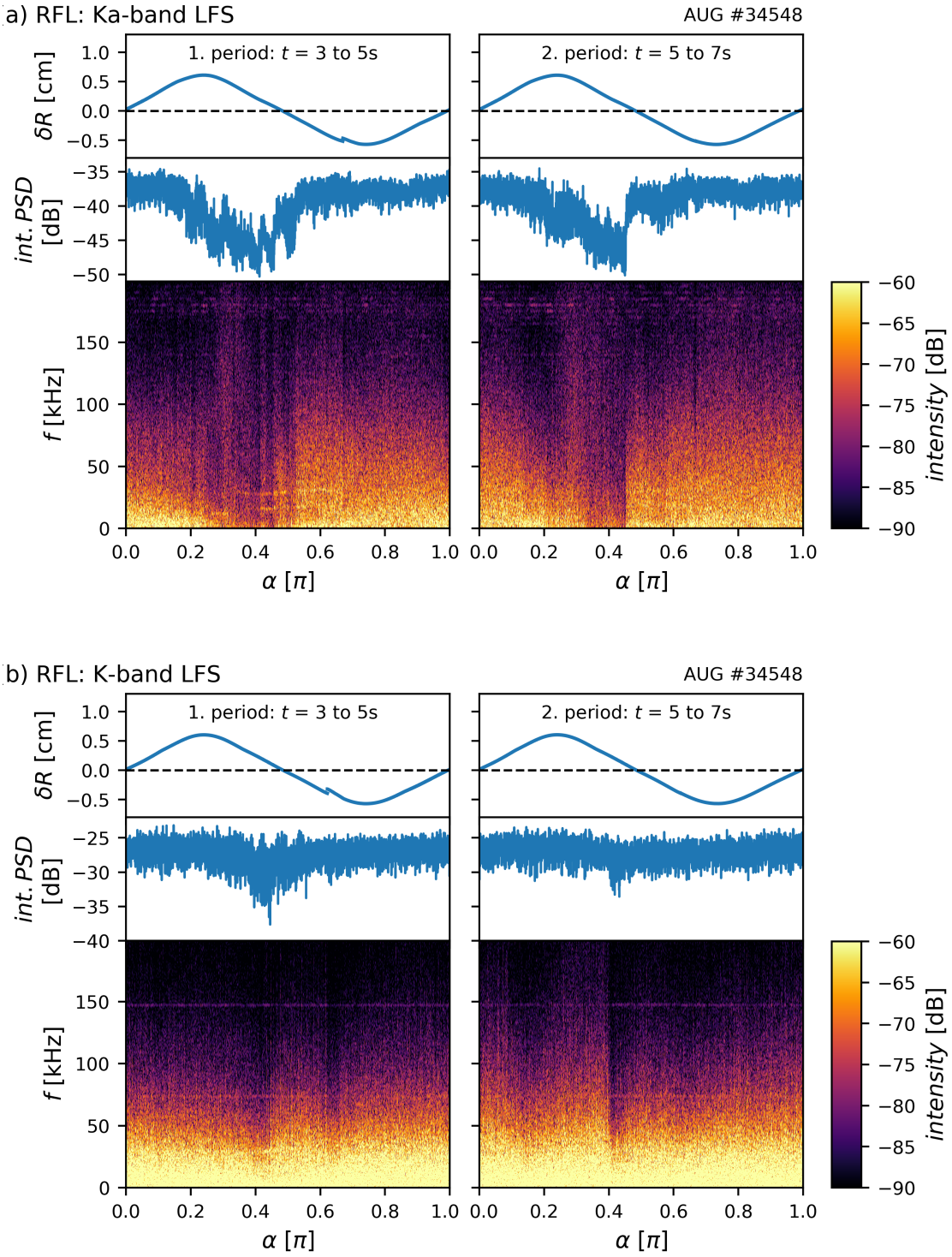

Figure 6.10: The radial displacement δR of the separatrix in the LOS of the diagnostic, the measured integrated power spectral density PSD and its spectrogram for the Ka-band (a) and K-band (b) systems on the LFS as a function of the helical field-line label α for both rotation periods.

drops from $\alpha = 0.2\,\pi$ onwards until a minimum of $-10\,\mathrm{dB}$ is reached in both periods at $\alpha \approx 0.41\,\pi - 0.46\,\pi$. Yet, the decreased signal intensity is not symmetric around these minima. The increase of the reflected intensity towards higher α happens faster, reaching the constant signal level again at $\alpha = 0.56\,\pi$ in the first period and $0.49\,\pi$ in the second period. Figure 6.11 shows the spectra of the Ka-band measurement for the first (solid) and second (dotted) rotation period for the case of $\alpha \approx 0.45\,\pi$ and $\alpha \approx 0.75\,\pi$, referring to reduced and fairly constant intensity, respectively. It can be seen that the intensity is reduced in the range of up to roughly 150 kHz, with increasing discrepancy towards lower frequencies. At frequencies higher than about 150 kHz the spectra are identical in all cases. The drop of the reflected intensity can also be observed in the scrape-off layer with the K-band measurement. Yet, the α range where it occurs is much smaller with $\alpha \approx 0.4\,\pi - 0.47\,\pi$ in the first and $\alpha \approx 0.4\,\pi - 0.45\,\pi$ in the second period. These small windows are close to where the minima in the Ka-band measurements were observed and are localized close to one of the zero crossings of the surface corrugation. In the case of the Ka-band measurement, the windows of reduced intensity begin roughly at the maximum of the surface corrugation and end just below the aforementioned zero crossing of the corrugation.

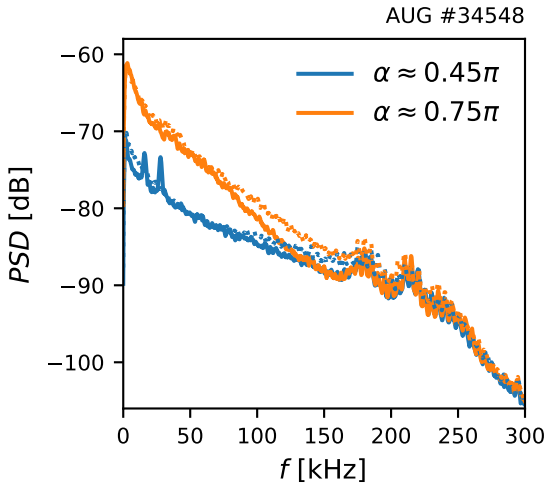

Figure 6.11: Power spectral density of the Ka-band measurement in the fairly constant phase ($\alpha \approx 0.75\pi$) and in the phase of decreased intensity ($\alpha \approx 0.45\pi$) in the first (solid) and second(dotted) rotation period.

The integrated power spectral density and its spectrogram shown in figure 6.12 are taken from the Ka-band system on the HFS. In this signal, an artificial line at $\approx 75\,\mathrm{Hz}$ and its harmonics were filtered out. A fluctuation gap as observed previously on the LFS can not be found on the HFS. Still, small variations in the broadband fluctuations are present in both rotation periods especially above $\approx 20\,\mathrm{kHz}$. For example, broadband fluctuations appear periodically at the beginning of both rotation periods and at the end of the first period. However, they do not occur at the same phase within the surface corrugation pattern and, therefore, it is not clear whether these fluctuations are related to the magnetic perturbation field or a temporal feature during the discharge.

6.2.2 Connection with Scrape-off Layer and Divertor Observations

In order to detect if the observed fluctuations actually cause net outward transport, it is necessary to find connections between those fluctuations and quantities related to transport onto the divertor plates.

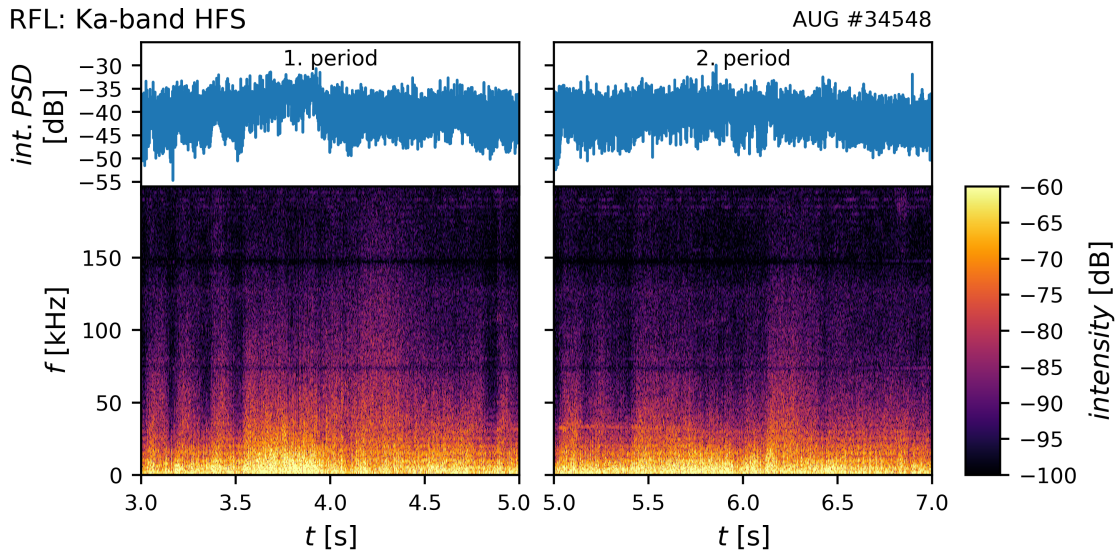

Figure 6.12: The measured integrated power spectral density PSD and its spectrogram for the Ka-band systems on the HFS as a function of time.

One indicator for increased outward transport can be the appearance of a density shoulder in the scrape-off layer. Figure 6.13 (left) shows density profiles measured by the Li-BES diagnostic in #34548. Since the separatrix position moves in radial direction during the rotation periods, the profiles are shifted at each time in radial direction such that the profiles overlap at $n_e = 1.2 \cdot 10^{19} \mathrm{m}^{-3}$, which is the approximated separatrix density. At a radial region in the near scrape-off layer centered around roughly $R = 2.12\,\mathrm{m}$, strong discrepancies between the density profiles at different toroidal positions in the perturbation field are observed. In the far scrape-off layer and in the steep gradient region the density measurements are converging. The right plot of figure 6.13 shows the electron density tracked at $R = 2.12\,\mathrm{m}$ as a function of the helical field-line label α for both rotation periods. One can see a strong sinusoidal dependence of the electron density in the near scrape-off layer on α, i. e. depending on the position in the perturbation field. The minimum electron density can be observed around $\alpha = 0.4\,\pi - 0.47\,\pi$, which is close to one of the zero-crossings of the surface corrugation. The maximum electron density is reached in a broader region centered around the other zero-crossing at $\alpha = 0.0$ or $1.0\,\pi$. The density shoulder disappears in the same phase of the surface corrugation pattern (i. e. around $\alpha = 0.45\,\pi$) where also the broadband density fluctuations observed in the gradient region on the LFS are strongly suppressed (see section 6.2.1).

Flush-mounted Langmuir probes (see section 2.2.7) on the outer divertor plates provide measurements of the electron density and temperature in the divertor region. They can be used for a comparison of density fluctuations in the divertor with the fluctuations measured by reflectometry in the confined region. However, the data acquisition rate of the Langmuir probes is limited to 22 kHz. Hence, the range of broadband density fluctuations measured by the conventional reflectometry up to 150 kHz can not be be covered by the Langmuir

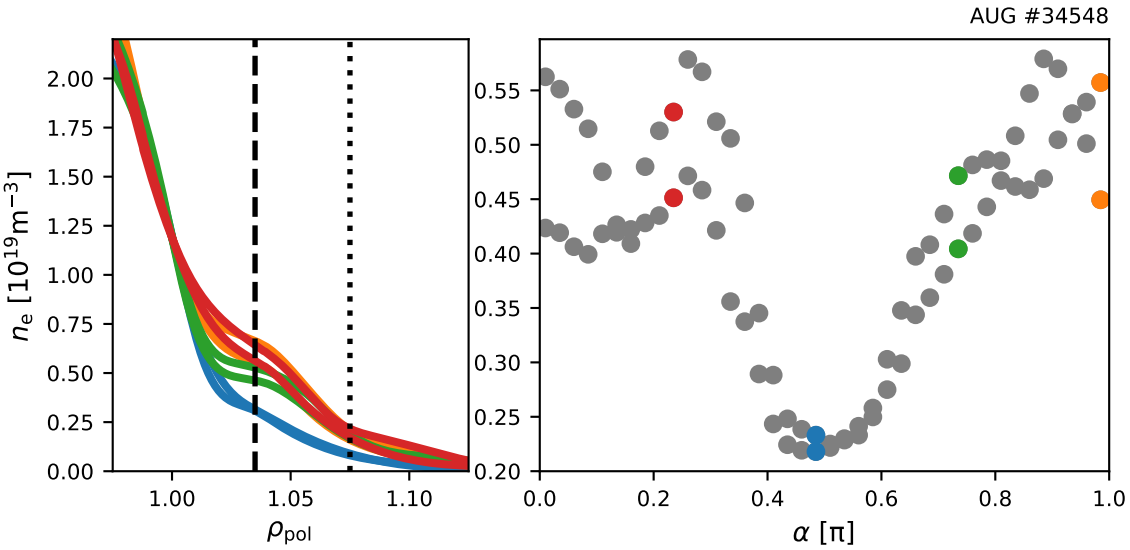

Figure 6.13: Left: Density profiles measured by Li-BES at different α for both periods (same color). The profiles are shifted such that all profiles exhibit a separatrix density of $1.2 \cdot 10^{19}\mathrm{m}^{-3}$. The dashed line approximates the center of the density shoulder, i. e. where the profiles are flattest. The dotted line corresponds to the approximate position where the shoulder region ends. Right: Density tracked at $\rho_{pol} = 1.035$ (dashed line in left plot).

probes, but just up to their Nyquist frequency of 11 kHz.

Density and temperature measurements of the probe *8ua7* are plotted in figure 6.14 for #34548. As long as ELMs are present before $t = 2.68$ s, the accompanied transient energy and particle transport onto the divertor can be seen as spikes in the Langmuir probe measurements. In the ELM suppression phase enclosed by the dashed lines, transient transport onto the divertor can still be observed in the electron density and temperature. During the rigid MP field rotation from $t = 3$ to 7 s, phases with strongly reduced transient peaks in density and temperature occur in both periods at the same time.

Spectrograms of the electron density measurements from Langmuir probes are plotted against time during the rigid MP field rotation of #34548 on the left side of figure 6.15. In most probes, broadband density fluctuations covering the whole measured frequency range can be observed, however, there are three exceptions. Probe *8ua1* shows no broadband fluctuations, since this probe is located in the private flux region (see figure 6.17), i. e. below the outer strike-point. Therefore, particles and energy expelled through the separatrix into the scrape-off layer in the majority of the plasma chamber will not reach this probe. Likewise, measurements of probe *8uac* are made far away from the strike-point and the measured signal is of the order of the noise level. Probe *8ua3* was not in operation. In the remaining probes, the measured fluctuations show a common pattern. While most of the time broadband fluctuations are present, time windows with a strongly reduced fluctuation level exist. These reduced fluctuation levels occur at different times in the individual probes. A rough trend can already be seen in figure 6.15 by adding a line to guide the eye. The further away the probe is from the strike-line, the earlier the window

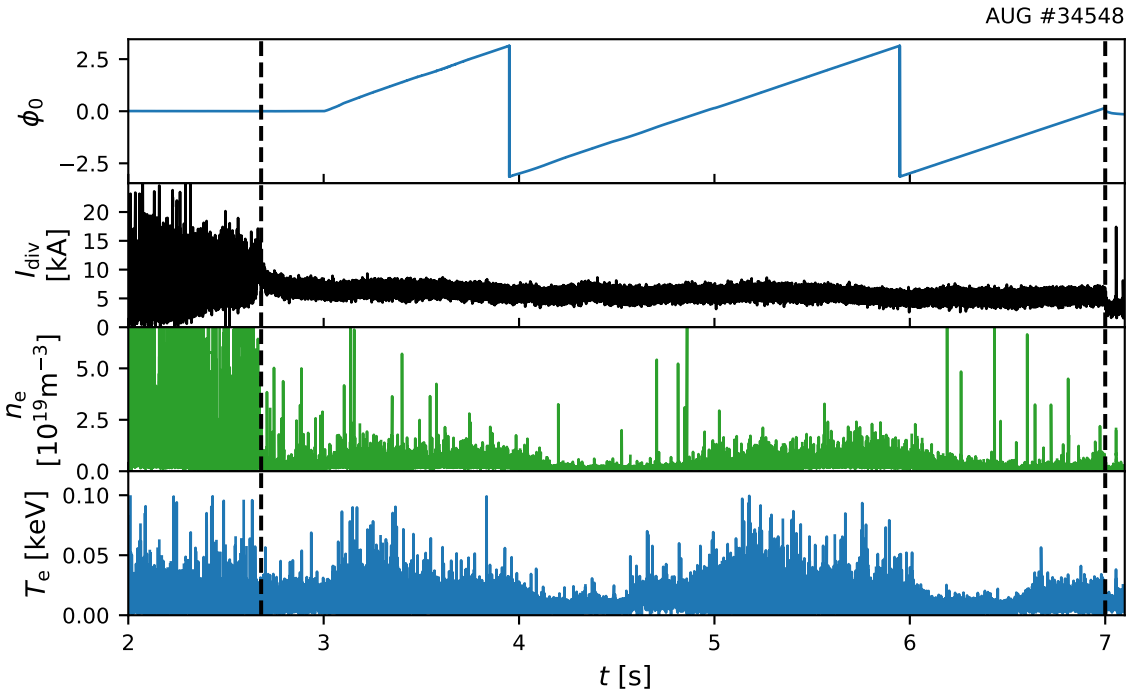

Figure 6.14: Time traces of the toroidal phase ϕ_0 of the MP field, the shunt current in the outer divertor I_{div} and the electron density and temperature measured by the divertor Langmuir probe *8ua7* for #34548. The dashed lines enclose the time of ELM suppression.

of reduced fluctuation level appears. The temporal shift is based on the fact that the Langmuir probes on the outer divertor are connected via field lines with different toroidal angles if traced to a certain horizontal plane. Figure 6.18 shows the poloidal (left) and toroidal (right) cross-sections of AUG including the Langmuir probes *8ua4* (blue), *8ua7* (orange) and *8uaa* (green). Also an approximate beam trace originating from the antenna of the Ka-band reflectometry system is shown (black, dotted). If field lines connected with these Langmuir probes are traced up to the horizontal plane which intersects with the trace of the Ka-band probe wave, they end at vastly different toroidal angles as seen in the plot of the toroidal cross-section. The field line tracing uses the magnetic equilibrium of CLISTE and the vacuum field generated by the MP coils. The plasma response to the MP field is not included. The positions of the Langmuir probes can now be mapped onto the helical field line label α as used for the Ka-band system including the toroidal offset between each Langmuir probes and the Ka-band probe wave as observed in figure 6.18. The resulting spectrograms mapped on α are shown in figure 6.15 on the right side. One can see that the region of reduced fluctuation amplitude align well at $\alpha \approx 0.4\,\pi - 0.7\,\pi$. This is in fairly good agreement with the observation from reflectometry presented in section 6.2.1 where the strongest reduction of broadband density fluctuations was observed in the steep gradient region of the confined plasma as well as in the scrape-off layer at around $\alpha \approx 0.4\,\pi - 0.47\,\pi$. Only the window of reduced fluctuation level in probe *8ua2* does not align well with the others. This probe is at the position of the strike-point as it can be seen

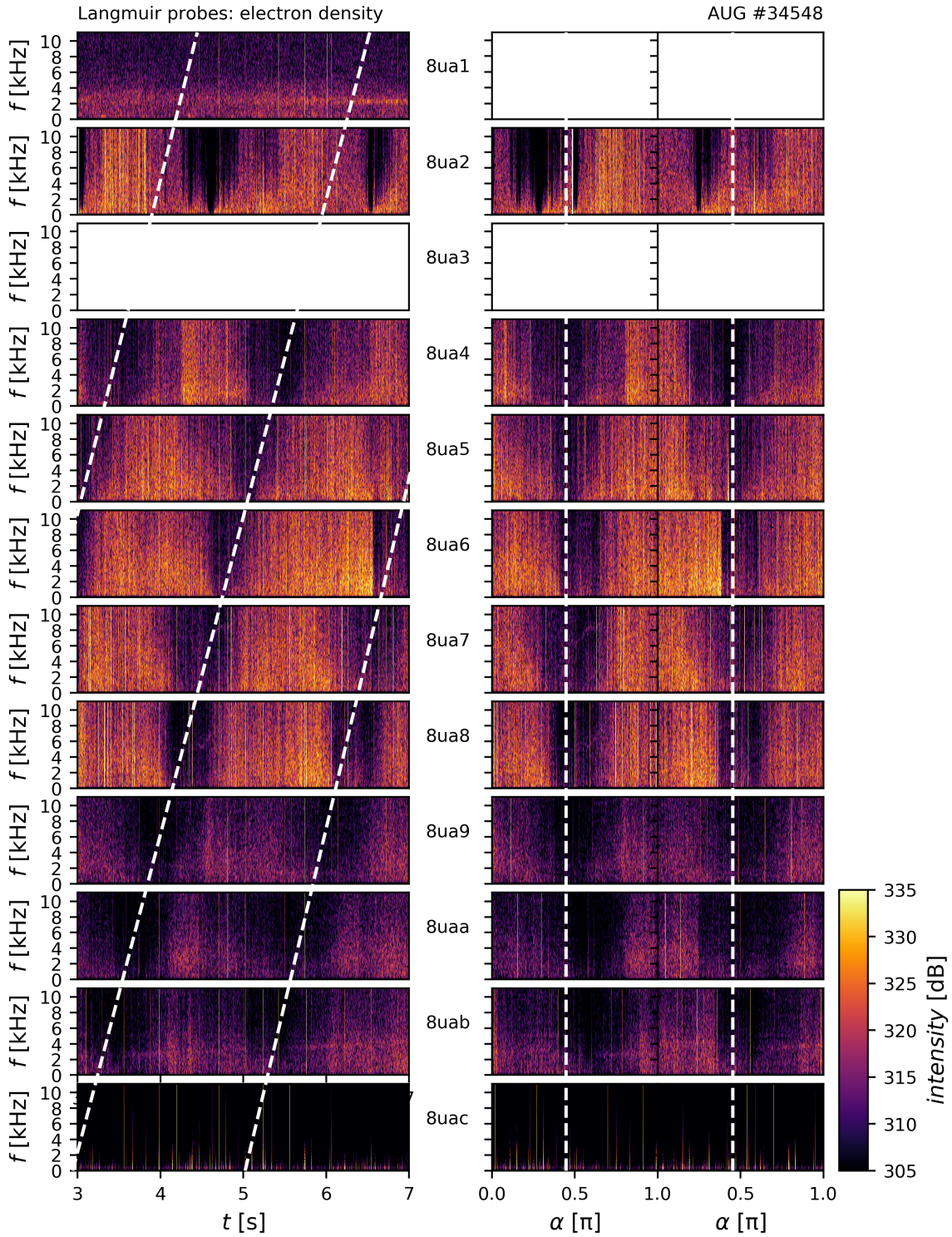

Figure 6.15: Spectrograms of the electron density as measured by the Langmuir probes in the outer divertor as a function of time (left) and α (right). The white dashed lines are guides for the eye leading roughly through the observed fluctuation gaps. On the right side, these lines are at constant $\alpha \approx 0.45\,\pi$.

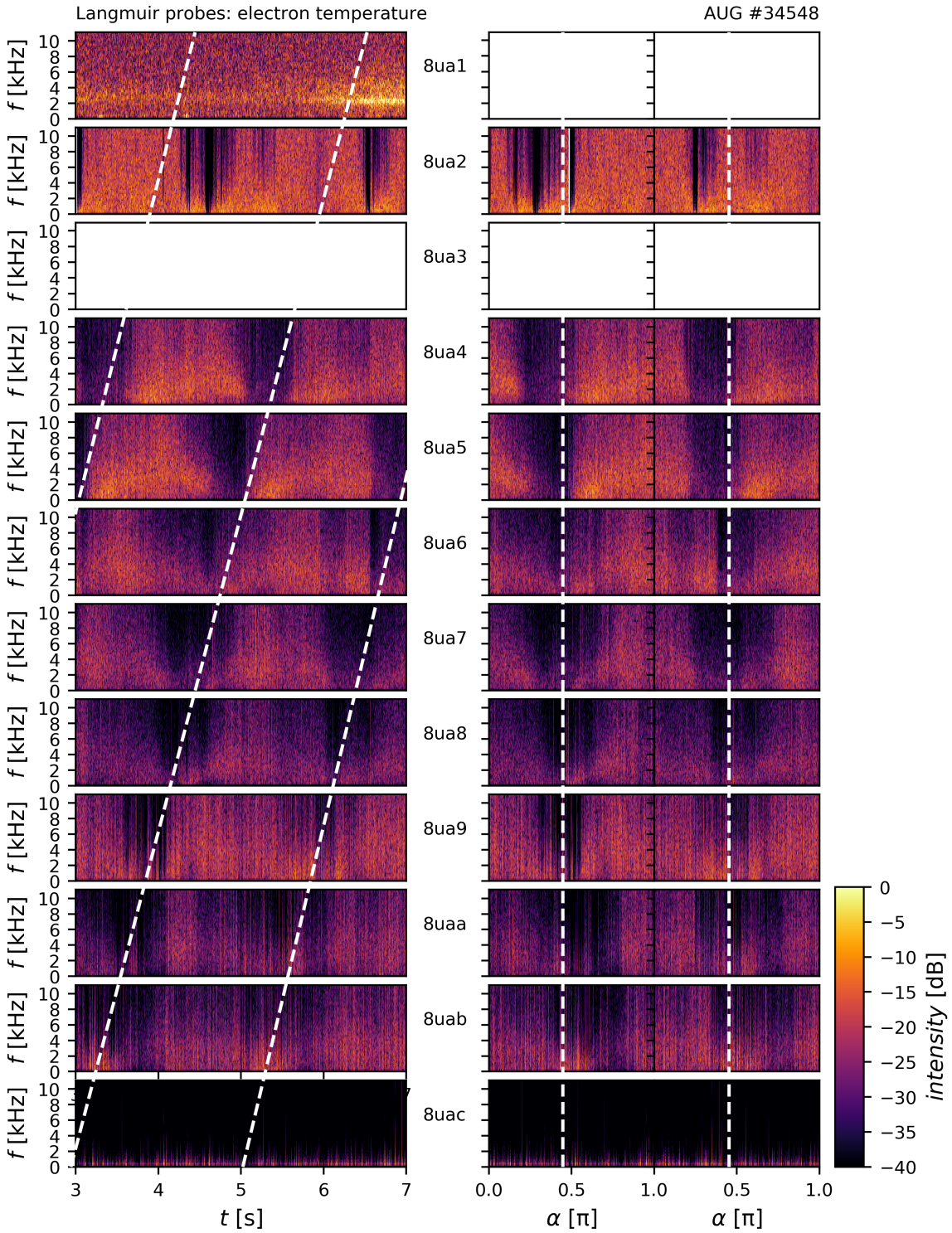

Figure 6.16: Spectrograms of the electron temperature as measured by the Langmuir probes in the outer divertor as a function of time (left) and α (right). The white dashed lines are the same guides for the eye as in figure 6.15.

in figure 6.17. A measurements at this position can be strongly influenced by movements of the strike-point during the discharge. Furthermore, a significant drop of intensity can be observed between probe *8ua8* and the ones closer to the strike-point as compared to probe *8ua9* and the ones further away from the strike-point. Probe *8ua9* intersects the flux surface $\rho_{\mathrm{pol}} = 1.075$ (dotted line in figure 6.17). This is also in the radial region where the outer end of the shoulder region is observed by Li-BES in figure 6.13.

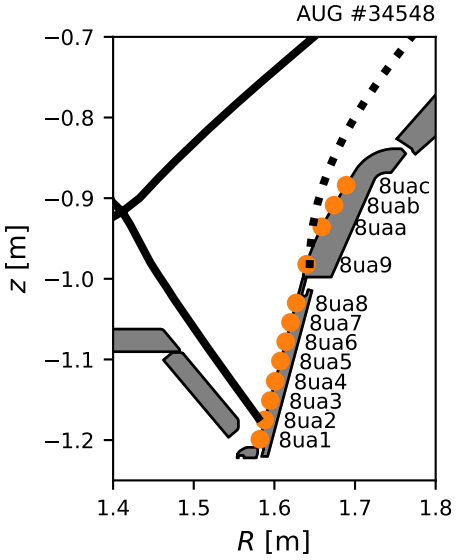

Figure 6.17: Poloidal cross-section of the outer divertor region showing the positions of Langmuir probes (blue dots) in the outer divertor. The separatrix position (solid line) and flux surface at $\rho_{\mathrm{pol}} = 1.075$ (dotted line) are included for #34548 at $t = 3.7\,\mathrm{s}$.

The spectrograms for the electron temperature as measured by the Langmuir probes are shown in figure 6.16. Similar to the elctron density measurement, phases of reduced fluctuation levels can be observed during the rigid rotation. In the case of the electron density, the mapping on the helical field-line label α showed an occurrence of these phases always at $\alpha \approx 0.4\,\pi - 0.7\,\pi$ for all reliable probes. For the electron temperature, this mapping shows worse agreement among the different probes (note that the guides for the eye are the same as in figure 6.15). Especially in the case of probes *8ua4* and *8ua5*, the phase of reduced fluctuation level occurs at lower α. Also, the sudden decrease of the fluctuation level at $\rho_{\mathrm{pol}} = 1.075$ can not be observed in the case of the electron temperature.

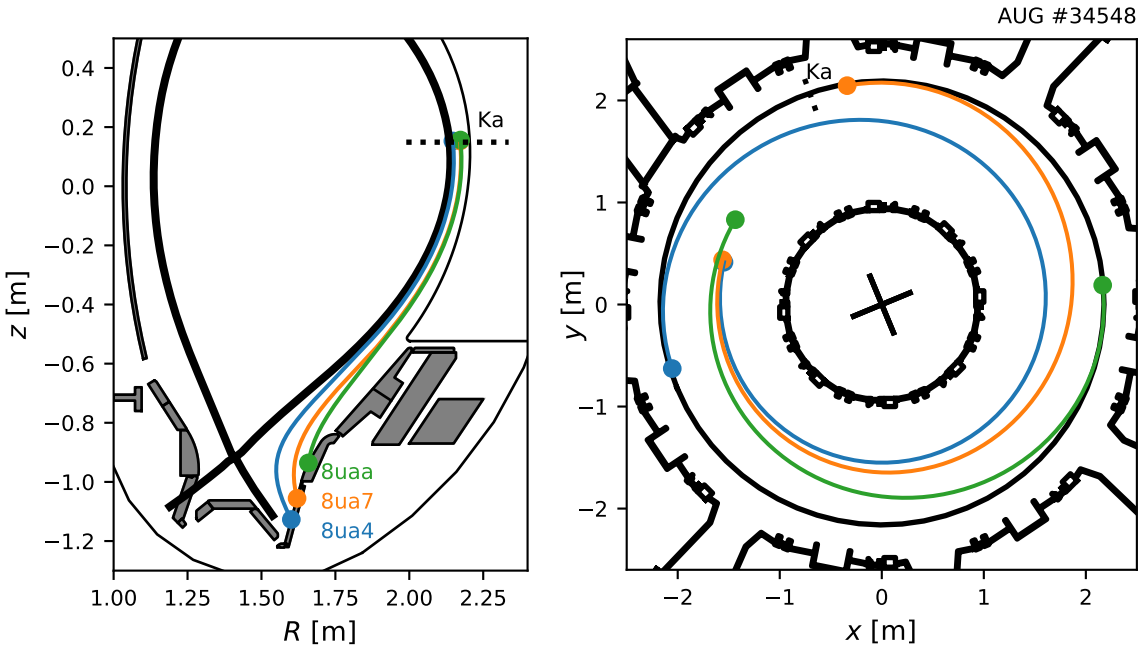

Figure 6.18: Poloidal (left) and toroidal (right) cross-section of ASDEX Upgrade showing the separatrix (black, solid), an indicator for the beam trace of the Ka-band system (black, dotted) and the traces of field lines (colored, solid) connected with three Langmuir probes (colored, dot) in the outer divertor followed up to the horizontal plane of the Ka-band system.

6.3 Observation of a Quasi-Coherent Mode

In #35307, magnetic perturbations with a toroidal mode number $n = 2$, differential phase $\Delta\phi = 90\,^\circ$ and $\phi_0 = 0\,^\circ$ at maximum coil currents were used to fully suppress ELMs. Figure 6.19 shows from top to bottom the effective coil current amplitude of the $n = 2$ perturbation field A_{eff}, a shunt current measurement in the divertor I_{div}, the line-integrated electron density around the pedestal top region $n_{\mathrm{e,H-5}}$, the integrated power spectral density PSD for the range of 25 to 85 kHz and the spectrogram of the Ka-band measurement as a function of time. When full ELM suppression was reached at $t = 2.22\,\mathrm{s}$ (dashed line), the electron density experienced another strong reduction. Along with this reduction, a quasi-coherent mode centered around 60 kHz appeared in the Ka-band measurement

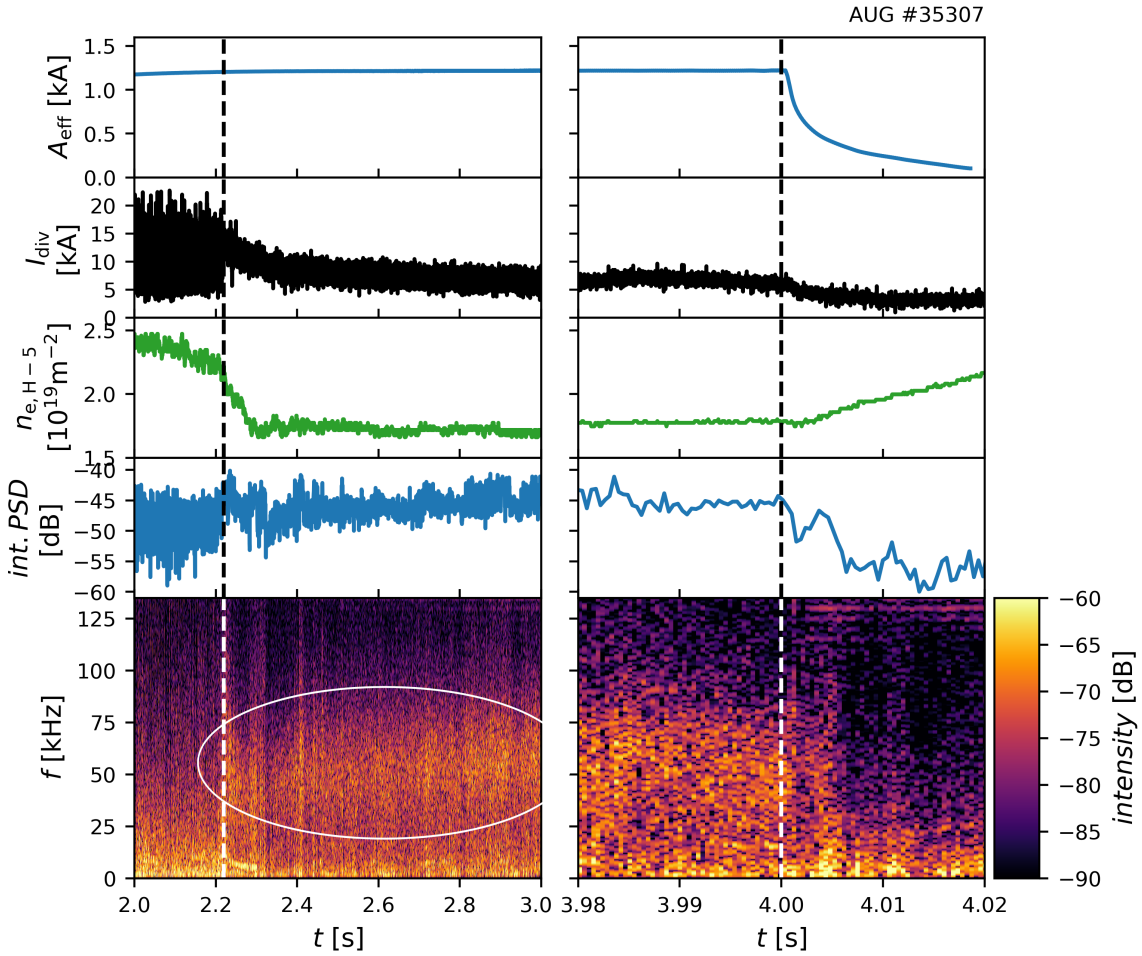

Figure 6.19: Time traces of the effective coil current amplitude of the $n = 2$ magnetic perturbation A_{eff}, the divertor shunt current measurement I_{div}, the line-integrated density at the pedestal top $n_{\mathrm{e,H-5}}$, the integrated power spectral density PSD and its spectrogram of the conventional reflectometer Ka-band measurement with respect to $t = 7\,\mathrm{s}$, which is when the power supply of the MP coils is switched off. The dashed lines indicate the onset and offset of the full ELM suppression. The white circle indicates the quasi-coherent mode.

(shown in figure 6.19) as well as in the K- and Q-band. The reflectometer RF frequency for the K-band system was set to 25 GHz, for the Ka-band system to 37 GHz and for the Q-band system to 40 GHz corresponding to a cut-off density of about 0.78, 1.70 and $1.98 \cdot 10^{19}\mathrm{m}^{-3}$, respectively. These cut-offs are shown in figure 6.20 with respect to the density profile measured by Li-BES at $t = 3.9 - 4.0$ s. While the K-band measured just outside the separatrix, the Ka- and Q-band measured close to the pedestal top. Yet, the quasi-coherent mode was just found on the LFS and is present during the steady ELM suppression phase until $t = 4$ s (dashed line in figure 6.19). At this time the MP field was switched off in a fast manner (as explained in section 2.1.3) in order to disentangle the presence of a magnetic perturbation from the low electron pedestal density as reason for the existence of the turbulence and the suppression of ELMs. One can see that within 1 ms after switching off the MP field, the shunt current measured in the divertor starts to drop. Also the power spectral density as measured by the Ka-band system and integrated over the frequency range of 25 – 85 kHz drops significantly within 10 ms after turning off the MP field indicating the disappearance of the quasi-coherent mode. The density then starts to increase at $t = 4.003$ s. Hence, while the magnetic perturbation field is present with a sufficient strong amplitude, ELMs are suppressed and the density stays stationary. When the magnetic perturbation field decays the quasi-coherent mode disappears even though the electron density hardly changed. Just after the disappearance of the mode, the electron density starts to increase indicating the transition from a stationary ELM suppressed scenario to a non-stationary ELM free scenario, in which the increased transport due to the magnetic perturbations is not present anymore.

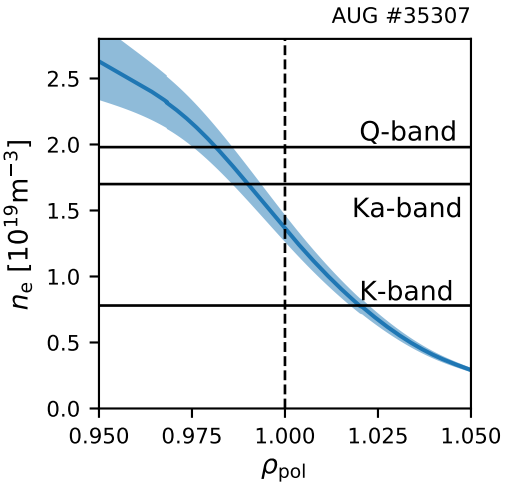

Figure 6.20: Electron density n_e profile as measured by Li-BES at $t = 3.90$ to 4.0 s. The horizontal lines are at the cut-off densities for the corresponding reflectometry band. The dashed line indicates the separatrix position.

6.3.1 Radial Localization

In order to radially localize the position of the observed quasi-coherent mode, discharges with steady ELM suppression and density with the maximum amplitude of the perturbation field can be investigated with the conventional reflectometry in a frequency 'hopping' mode. In all discharges, an $n = 2$ MP field was used at full amplitude, $\Delta\phi = 90\,^\circ$ and $\phi_0 = 0\,^\circ$.

In #35310, #35943 and #36514, the K-, Ka- and Q-band systems hopped through several different probing frequencies covering most of the plasma edge region. In #35943 the Ka-band measurement was not reliable and, therefore, is not used here. Figure 6.21 shows fits of the density profiles to the IDA data (grey). The highlighted points in the fit serve as an indicator for the appearance of the quasi-coherent mode. Here, a green

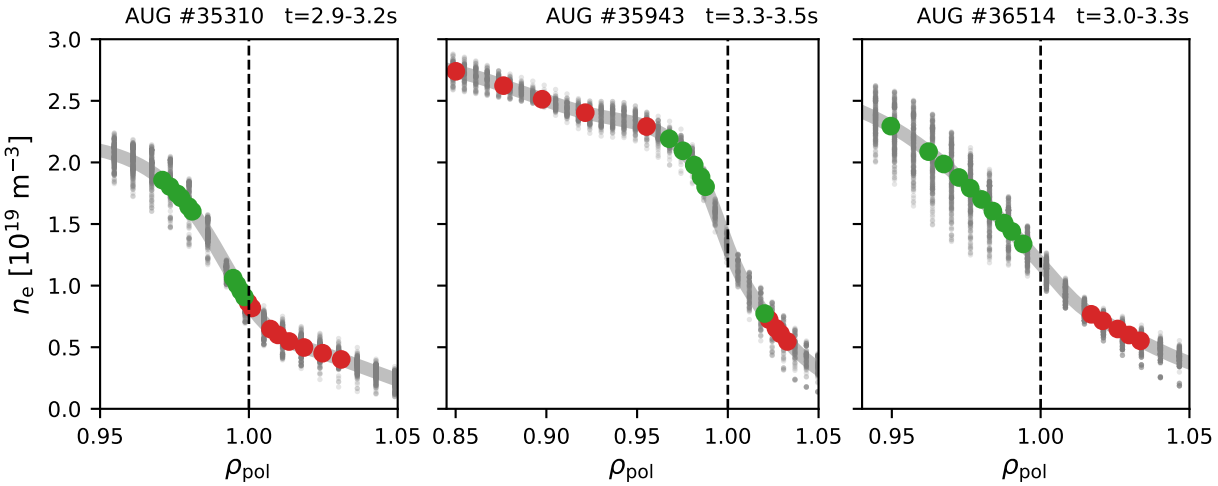

Figure 6.21: Electron density n_e profiles as calculated by IDA (grey dots) and their fit (grey line). The colored points within the fit indicate the measurement positions of the conventional reflectometry systems. Green indicates an observation of the mode, while red refers to the mode not being spotted. The dashed lines indicate the separatrix positions.

point refers to a radial position where the mode was observed in the reflectometry, while a red point refers to a measurement in which the mode was not seen. In #35310 and #36514, the mode can be found all across the steep gradient region from the pedestal top up until the separatrix (dashed lines), whereas it is not found in the scrape-off layer region. Additional measurements further inward are accessible in #35943, which provide information on the radial expansion of the mode towards the core region. One can see that as soon as the density profile flattens at the pedestal top, the mode can not be observed anymore. However, at the pedestal top and in the core region, the electron profile is significantly flatter than in the edge region. In combination with the uncertainties in the density measurements, this leads to an increased uncertainty in the actual radial position of the cut-off layers of each probing frequency. Also, in #35943 — and in contrast to the other presented discharges — the mode was observed temporarily in the innermost measurement of the K-band in the scrape-off layer. In this discharge, the density gradient at the position of the K-band measurement in the near scrape-off layer is also significantly higher than in #35310 and #36514, in which the mode was not observed in the K-band.

6.3.2 Toroidal Asymmetry

During the rigid rotation discharge presented in section 6.2.1, the quasi-coherent mode was not observed by reflectometry. This might result from the need to reduce the amplitude of the magnetic perturbation field during rigid rotations. The maximum possible amplitude of the $n = 2$ perturbation field can only by obtained by four selected field orientations $\phi_0 = 0\,°$, $\phi_0 = 90\,°$, $\phi_0 = 180\,°$ and $\phi_0 = 270\,°$, for which all coils carry the maximum current. In #35862, the four different orientations ϕ_0 of the MP field allowing for maximum amplitude were scanned in order to investigate the toroidal symmetry of the quasi-coherent mode.

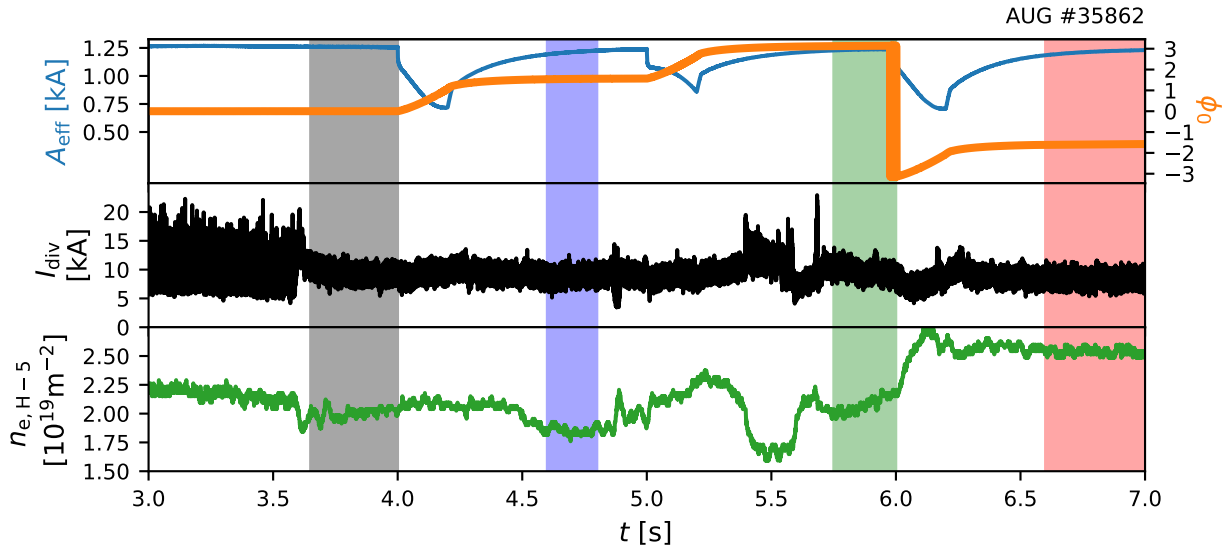

Figure 6.22: Time traces of the effective $n = 2$ MP coil current amplitude A_{eff} and phase ϕ_0, the divertor shunt current measurement I_{div} and the line-integrated density at the pedestal top $n_{\mathrm{e,H-5}}$ for #35862. The shaded areas are the references for figure 6.24.

figure 6.22 shows the evolution of the $n = 2$ MP field amplitude and orientation, the shunt current measurement in the divertor and the line-integrated electron density at the pedestal top. Four phases, one at each orientation, are chosen (highlighted time periods) based on having similar density and MP field amplitude as well as being in ELM suppression. The only exception is $\phi_0 = 270\,^\circ$ (red) due to the increased density as compared to the other phases. The density profiles during the phases of $\phi_0 = 0$, 90, and $180\,^\circ$ are comparable and, hence, the profile taken at $t = 3.9\,\mathrm{s}$ (black) was used to represent them in figure 6.23. The density profile in the fourth phase with $\phi_0 = 270\,^\circ$ and increased electron pedestal density is shown in red. Throughout the discharge, the conventional reflectometry systems were hopping through the probing frequency range of 35 – 40 GHz in 1 GHz steps, covering the vertical grey shaded range at the steepest electron density gradient in figure 6.23. As it was shown in section 6.3.1, the quasi-coherent mode exists in the steep gradient region up to the pedestal top, which is partially covered by these reflectometry measurements. In order to compare measurements at the same radial position, the measurement at 37 GHz is taken for the cases with $\phi_0 = 0$, 90 and $180\,^\circ$ (black horizontal line and profile, respectively) and at 40 GHz for $\phi_0 = 270$ GHz (red horizontal line and profile, respectively). The spectra of these measurements are plotted in figure 6.24 for the highlighted time intervals in figure 6.22. While the absolute PSD can not be compared between these measurements, one can see that the quasi-coherent mode can be observed at 40 – 60 kHz just in the case with the toroidal orientation $\phi_0 = 0\,^\circ$. At this orientation, the mode is present at all probing frequencies covering the shaded region in figure 6.23, while for the other orientations the mode can not be found at any frequency.

As mentioned earlier, during the rigid rotation in #34548 the quasi-coherent mode has not been observed. Another rigid rotation during ELM suppression has been performed in

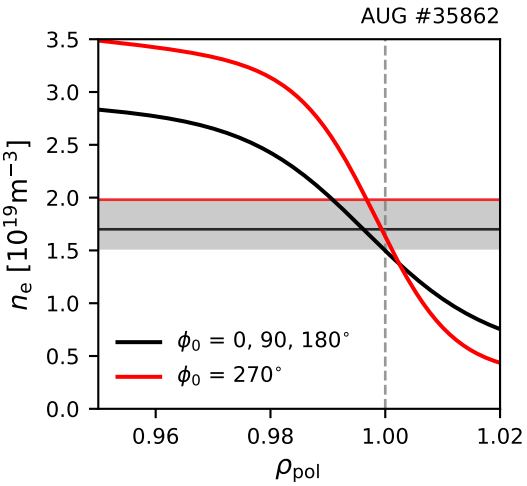

Figure 6.23: Electron density profiles fitted to Thomson scattering and interferometry data. The black profile is taken at $t = 3.65 - 4.0$ s and the red profile at $t = 6.6 - 7.0$ s. The vertical grey shaded region represents the range covered by reflectometry measurements. The black and red horizontal lines are at the cut-off densities for 37 and 40 GHz, respectively.

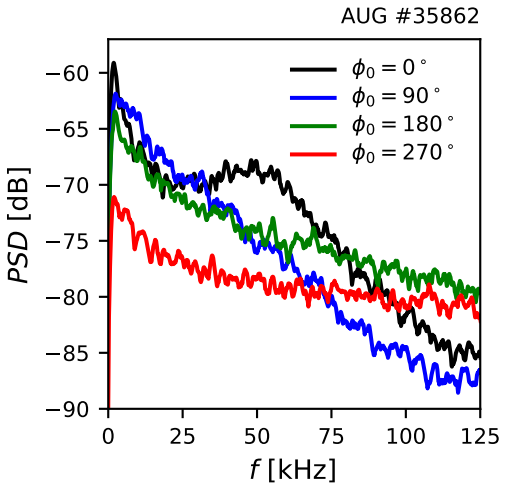

Figure 6.24: Power spectral density of the reflectometry measurements at 37 GHz for $\phi_0 = 0$, 90, 180 ° and 40 GHz for $\phi_0 = 270$ °.

#35929 (see figure 6.25) with a higher rotation frequency of 0.75 Hz, opposite rotation direction and different starting angle ϕ_0 as compared to #34548. The Q-band system of the conventional reflectometry was operated with a fixed probing frequency of 36 GHz corresponding to a cut-off density of about $1.6 \cdot 10^{19}$m^{-3}. In the spectrogram of this reflectometry signal, the fluctuation gap can be observed during each rotation period especially below 25 kHz, e. g. at $t = 3.0 - 3.3$ s, $4.25 - 4.55$ s and $5.7 - 6.0$ s (see figure 6.25). However, due to the inverted coil current in *Bl5* the foreseen rigid rotation in #35929 lead to several perturbing effects. First of all, while the rotation of the $n = 2$ MP field invoked by the upper row of coils stays linear (shown as ϕ_0 in figure 6.25), the rotation of the mixed $n = 2$ and $n = 1$ MP field in the lower row is non-linear. Second, the $n = 1$ and $n = 2$ amplitudes are modulated in anti-phase during the rigid rotation. Hence, not only does the electron density steadily increase during the discharge as a consequence of the overall reduced MP field amplitude, but also some modulations of the density can be seen during the rigid rotation. In figure 6.26, density profiles are shown for the three phases (as highlighted in figure 6.25) in which the fluctuation gap has been observed. The horizontal line indicates the cut-off density of the reflectometry measurement. In any of these cases, the measurement position is within the steep gradient region, but it moves further away from the pedestal top during the discharge. In contrast to #34548, the quasi-coherent mode can also be observed in this discharge during the rigid rotation from $t = 2.98$ to 3.25 s, as it can be seen in the corresponding blue reflectometry spectrum in figure 6.27. This phase during the rigid rotation overlaps partially with the fluctuation

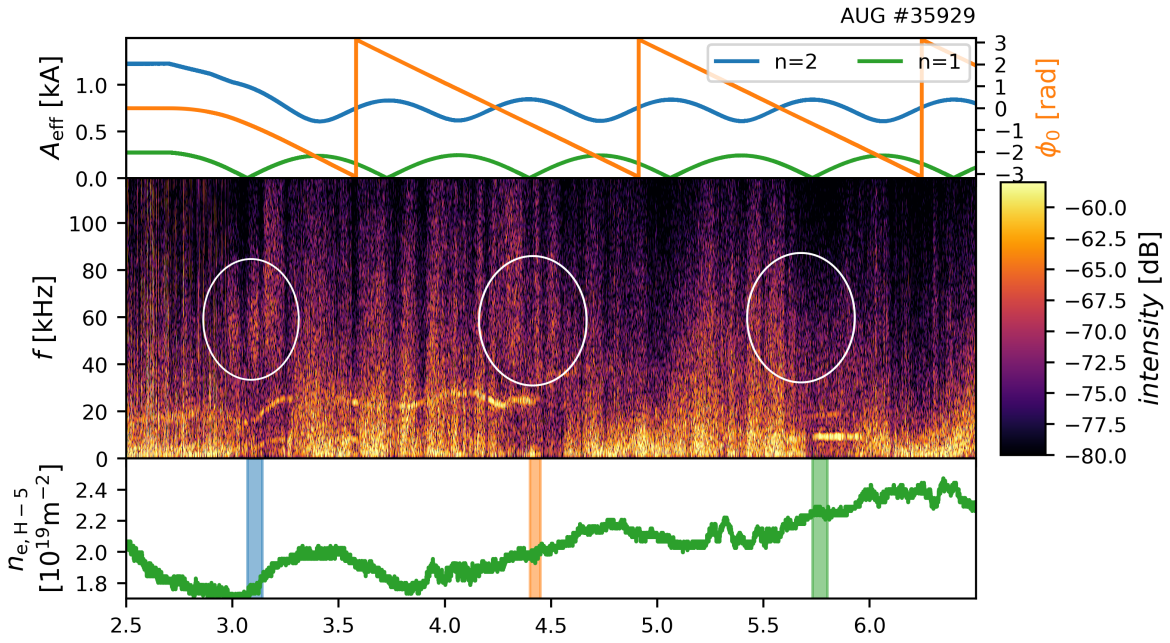

Figure 6.25: Time traces of the effective $n = 2$ and $n = 1$ MP coil current amplitudes A_{eff}, the phase of the upper row of coils ϕ_0, the spectrogram of the conventional reflectometry with a probing frequency of 36 GHz and the line-integrated density at the pedestal top $n_{\mathrm{e,H-5}}$ during a rigid rotation in #35929. The shaded regions in the density signal refer to the measurement times for figures 6.26 and 6.27. The white circles are a guide identifying the presence of the quasi-coherent mode.

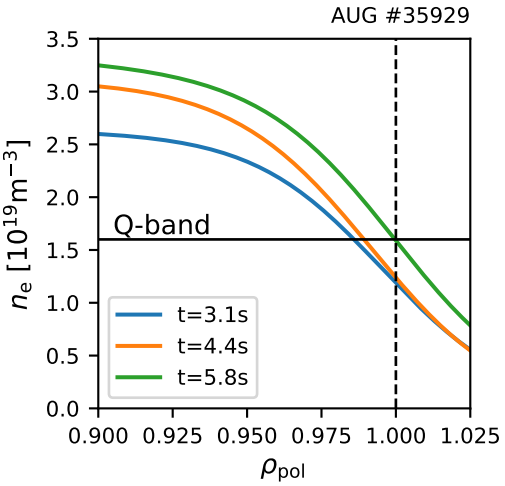

Figure 6.26: Fits of the electron density n_{e} profile as measured by Li-BES, Thomson scattering and interferometry at three different times during #35929. The colors refer to the shaded time intervals in figure 6.25. The horizontal line indicates the cut-off density for the Q-band reflectometry system at 36 GHz. The dashed line indicates the separatrix position.

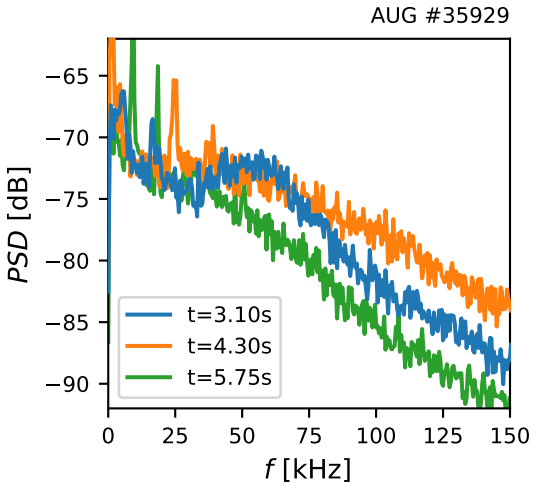

Figure 6.27: Power spectral density of the reflectometry measurements at 36 GHz for the three different time intervals highlighted in figure 6.25.

gap which can be identified best during the rigid rotation by the absence of low frequency $f < 20\,\mathrm{kHz}$ fluctuations at roughly $t = 3.05 - 3.25\,\mathrm{s}$. At the beginning of the time period, in which the quasi-coherent mode is observed, at $t = 2.98 - 3.05\,\mathrm{s}$ and at the end of that period at $t = 3.25\,\mathrm{s}$, both, the quasi-coherent mode and the low frequency fluctuations can be observed. Around the second fluctuation gap, the quasi-coherent mode can not be observed directly anymore as a peak in the spectrum, but from $t = 4.25$ to $4.5\,\mathrm{s}$ the spectrum is significantly flattened. Around the third fluctuation gap at $t = 5.7 - 6.0\,\mathrm{s}$, no indications of the quasi-coherent mode can be seen anymore. Besides the movement of the measurement position, another difference between the time of the first and second fluctuation gap is, that the $n = 2$ amplitude is larger during the first fluctuation gap.

Due to the wrong wiring of the *Bl5* coil and its aforementioned consequences, an experimental evaluation of the surface displacement as well as a prediction by VMEC are not reasonable. However, a comparison between the effective coil currents in all MP coils of #35862 and #35929 can be done. The effective coil current pattern of #35862, during which the quasi-coherent mode was observed in the reflectometry, was reached in #35929 at $t = 3.25\,\mathrm{s}$, $4.24\,\mathrm{s}$ and $5.57\,\mathrm{s}$. This is in fairly good agreement with the times at which the quasi-coherent mode was observed in #35929.

6.4 Transitions between Broadband Fluctuations and the Quasi-Coherent Mode

On the one hand, toroidally asymmetric broadband density fluctuations have been observed during rigid rotations of the MP field in discharges with full ELM suppression (see section 6.2). On the other hand, a quasi-coherent mode has been observed at a certain toroidal angle when the MP field was static and at full amplitude (see section 6.3). In this section, transitions between these two regimes are described in two different cases.

6.4.1 Scan of the Magnetic Perturbation Field Amplitude

In order to study the amplitude dependence of both phenomena, the amplitude of the perturbation field was varied in #35943 at fixed $n = 2$, $\Delta\phi = 90\,^\circ$ and $\phi_0 = 0\,^\circ$, which is the toroidal orientation at which the reflectometry can observe the quasi-coherent mode. Figure 6.28 gives an overview of this discharge. In the time from $t = 3$ to 7.5 s, the amplitude of the MP field is reduced step-wise every 0.5 s from 1.26 to 0.96 kA. During this period, full ELM suppression is always sustained, while the line-integrated density measured close to the pedestal top increases continuously. During each step of the MP field amplitude, the K- and Q-band systems of the conventional reflectometry hopped through multiple probing wave frequencies. This ensures that measurements at the location of the quasi-coherent mode, i. e. in the steep gradient region and up to the pedestal top, are available during the whole discharge as the density and, therefore, measurement position of the reflectometry alter. Fitted density profiles and markers for the occurrence of the quasi-coherent mode are presented in figure 6.29 for three different times. The left plot is related to the phase at highest effective $n = 2$ MP coil current amplitude $A_{\text{eff}} = 1.26$ kA at $t = 3.0$ – 3.5 s, and here the quasi-coherent mode can be observed at the pedestal top and in the upper range of the steep gradient region. The middle plot corresponds to the phase at $t = 5.5$ – 6.0 s with $A_{\text{eff}} = 1.075$ kA. There, the quasi-coherent mode can just be observed at one reflectometer frequency which probes in the upper part of the steep gradient region close to the pedestal top. At lower A_{eff}, the quasi-coherent mode can not be observed anymore. The right plot shows such a case with $A_{\text{eff}} = 0.96$ kA at $t = 7.0$ – 7.5 s.

6.4.2 Modulation of the Magnetic Perturbation Field Amplitude

In #35521, an $n = 2$, $\Delta\phi = 90\,^\circ$ and $\phi_0 = 0\,^\circ$ MP field was used to fully suppress ELMs. In the time between $t = 5.2$ and 7.3 s, full ELM suppression was achieved and the current in the MP coils has been modulated with 2 Hz. The applied modulation results in a magnetic perturbation with an $n = 2$ component, whose amplitude is modulated sinusoidally between roughly 0.9 and 1.17 kA. During this modulation experiment, transitions between the quasi-coherent mode and broadband density fluctuations can be observed with the conventional reflectometry, while ELM suppression was maintained throughout. Figure

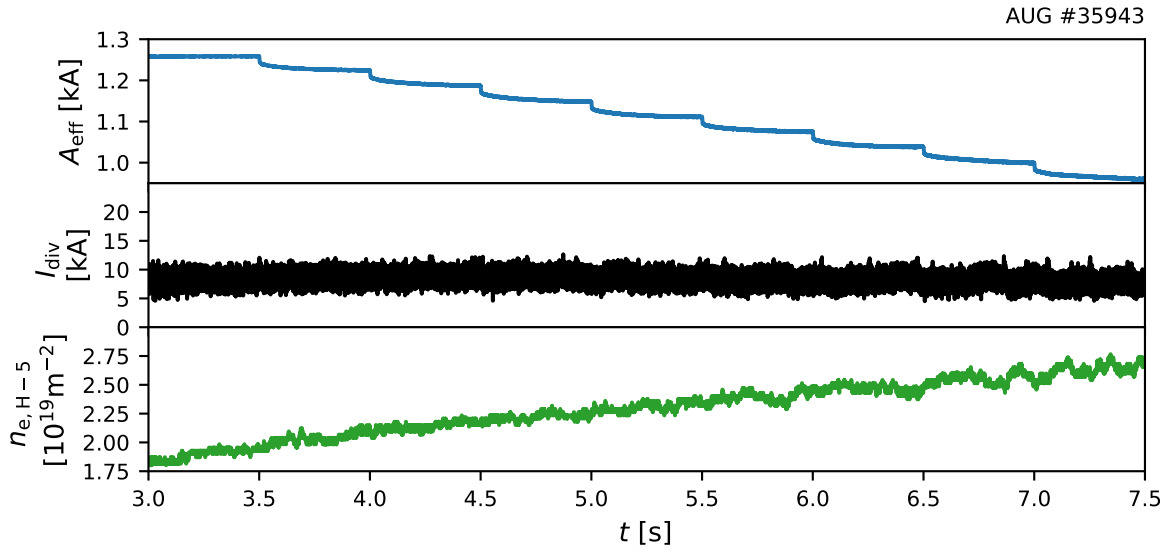

Figure 6.28: Time traces of the effective $n = 2$ MP coil current amplitude A_{eff}, the divertor shunt current I_{div} and the line-integrated electron density at the pedestal top $n_{\mathrm{e,H-5}}$ for #35943.

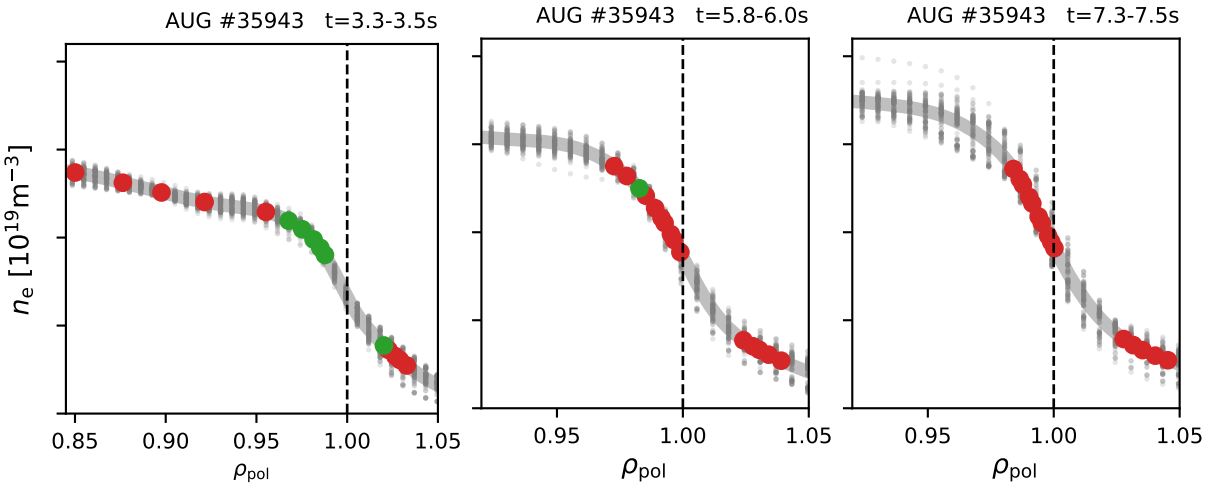

Figure 6.29: Electron density n_{e} profiles as calculated by IDA (blue dots) and their fit (blue line). The colored points within the fit indicate the measurement positions of the conventional reflectometry systems. Green indicates an observation of the mode, while red refers to the mode not being detected. The dashed lines indicate the separatrix positions.

6.30 shows a time trace of the line-integrated density at the pedestal top $n_{e,H-5}$ as well as a spectrogram of the Ka-band reflectometry measurement from the LFS. The modulated $n = 2$ effective MP coil current amplitude is shown as an overlay. Due to the MP field modulation also the electron density is modulated consequently. Shown in figure 6.31 are two density profiles for the density extremes: one at the maximum (blue) and one at the minimum (orange) of the modulated density (colors correspond to shaded areas in figure 6.30). It can be seen that the measurement positions of the different reflectometry bands stay approximately constant around the separatrix and in the scrape-off layer. The quasi-coherent mode can be observed on the LFS in all three bands, though, just transiently as seen in figure 6.30 for the Ka-band, which was operated at a fixed frequency of 35 GHz. Phases where the quasi-coherent mode can be observed are interrupted by phases in which only broadband fluctuations are present. A comparison of the reflectometry spectra in these phases is shown in figure 6.32. The frequency of the quasi-coherent mode is centered around 40 – 60 kHz (not to be confused with the tearing mode seen at 20 – 30 kHz). In the phases where the quasi-coherent mode is absent, broadband fluctuations increase especially at frequencies below approximately 15 kHz. Transitions from the state with a quasi-coherent mode to broadband turbulence and back occur with the same frequency

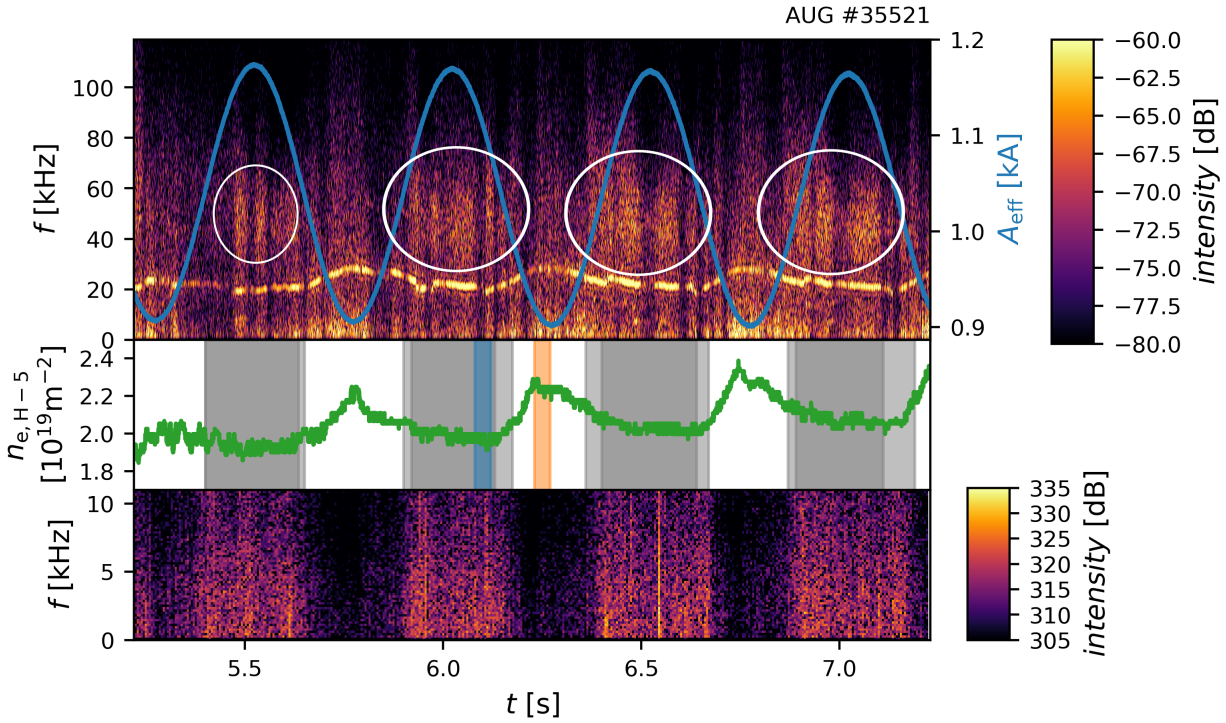

Figure 6.30: Spectrogram of the Ka-band reflectometry measurement at a fixed probing frequency of 35 GHz (top) and time trace of the line-integrated electron density at the pedestal top $n_{e,H-5}$. The spectrogram is overlayed by the modulated effective $n = 2$ MP coil current amplitude. The dark grey shaded region on the electron density time trace indicates the presence of the quasi-coherent mode, the light grey region its uncertainty. The spectrogram at the bottom is taken from the density measurement of the divertor Langmuir probe *8ua9*. The quasi-coherent mode is encircled in white.

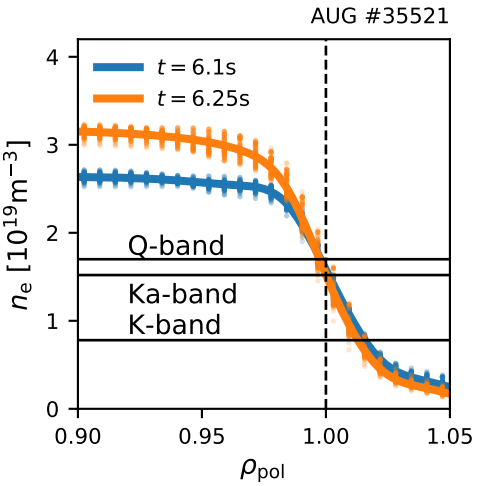

Figure 6.31: Electron density n_e profiles as calculated by IDA (dots) and their fit (line) at the minimum and maximum of the density modulation as indicated by the shaded areas in figure 6.30. The horizontal lines represent the cut-off densities of the various reflectometry measurement frequencies used in this discharge. The dashed line indicates the separatrix position.

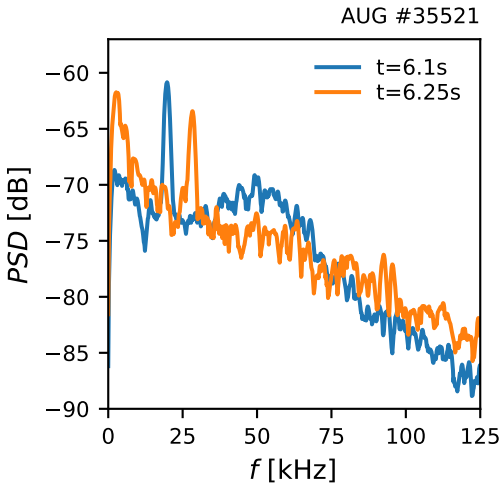

Figure 6.32: Spectra of the Ka-band reflectometry measurement of #35521 at two different times. At $t = 6.1$ s the quasi-coherent mode can be observed, while it is absent at $t = 6.25$ s. These times correspond to a maximum and minimum of the modulated $n = 2$ perturbation field amplitude, respectively.

as the MP field amplitude modulation, i. e. with 2 Hz. The effective coil current amplitude of the $n = 2$ magnetic perturbation field at the time of each back and forth transition is shown in figure 6.33. It varies slightly in the range of 1.0 to 1.06 kA, which agrees well with the observed disappearance of the quasi-coherent mode at an amplitude between 1.04 and 1.075 kA in the previous MP field amplitude scan. In the time trace of the electron density in figure 6.30, the grey shaded region indicates the presence of the quasi-coherent mode and the light grey edges the uncertainty in the identification of the mode. The modulation of the density deviates from a single frequency sinusoidal modulation, but rather shows plateaus which are followed by sudden increases of the density. The onsets of the sudden increases are approximately simultaneous to the disappearance of the quasi-coherent mode. This indicates that additional outward directed particle transport is associated with the presence of the quasi-coherent mode. Furthermore, when the quasi-coherent mode is present, density fluctuations in some of the divertor Langmuir probes are increased as shown in figure 6.30.

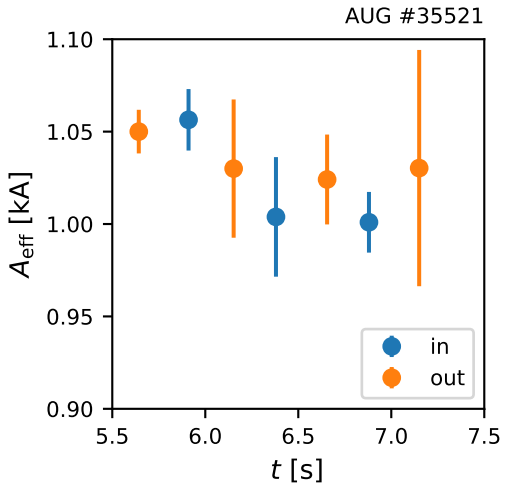

Figure 6.33: Effective $n = 2$ MP coil current amplitude at the times of the transitions into and out of the phases with the quasi-coherent mode.

6.5 Critical Parameters for Turbulence Drive and Suppression

In this section, we examine parameters which are generally thought to be relevant for stabilizing and destabilizing turbulence during ELM suppression. With non-axisymmetric perturbations, these parameters will in general depend on the toroidal angle. We will compare these parameters to a reference case without magnetic perturbations and discuss their possible relationship with the toroidally localized turbulence.

Figure 6.34 gives an overview over the reference discharge #33998 (blue) as compared to the discharge with a rigid rotation #34548 (orange), in which the toroidal asymmetry has been studied during ELM suppression in the section before. Both discharges have similar control parameters such as heating power, toroidal magnetic field, plasma current, plasma shape and plasma fueling. The only difference are the magnetic perturbations, which have been switched on in #34548 at $t = 1.5\,\mathrm{s}$ and were not applied in #33998. Hence, #33998 stayed in ELMy H-mode throughout the discharge and also no pump-out effect can be observed. Consequently, the density traces of these discharges start to deviate at $t = 1.5\,\mathrm{s}$. While the electron and ion temperatures remain comparable even after the MP coils had been turned on in #34548 ($t = 1.5 - 2.2\,\mathrm{s}$), both temperatures increase in the ELM suppression phase above the reference. As the reference case we choose the time interval from $t = 2.8$ to $3.1\,\mathrm{s}$ in #33998.

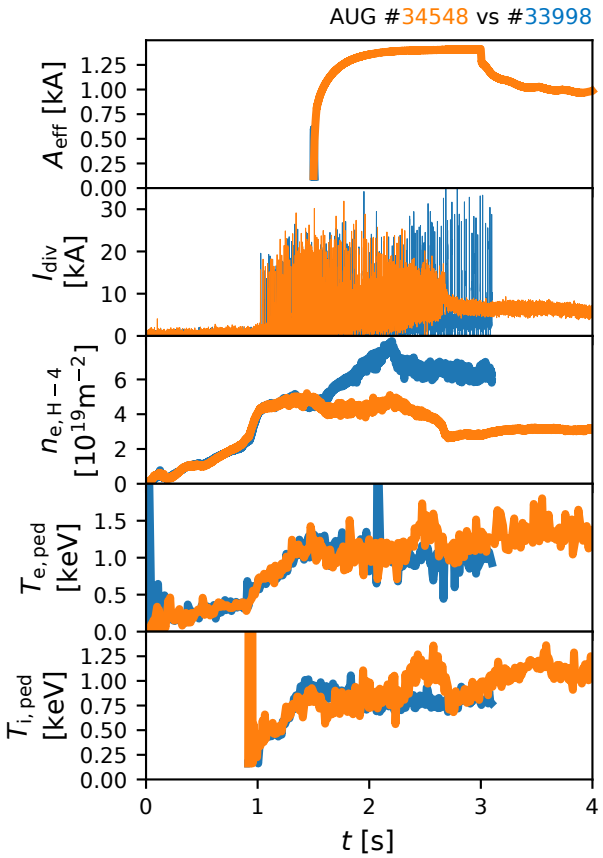

Figure 6.34: Time traces of the effective $n = 2$ MP coil current amplitude A_{eff}, the divertor shunt current measurement I_{div} as well as the line-integrated electron density $n_{\mathrm{e,H-4}}$, electron temperature $T_{\mathrm{e,ped}}$ and ion temperature $T_{\mathrm{i,ped}}$ close at the pedestal top.

6.5.1 Density and Temperature Gradients

A set of important parameters for driving turbulence are the normalized inverse gradient lengths of electron density and ion temperature. In figure 6.35, the inverse normalized gradient lengths R/L_x with $L_x = x/\nabla x$ of the electron density (blue) and ion temperature (orange) are shown for the reference case as measured by Li-BES and CXRS, respectively. They reach about the same

maximum of $-R/L_x \approx 150$ in both cases. With the application of a magnetic perturbation, the confining magnetic field is perturbed in a kink-like manner creating regions of compressed and expanded poloidal flux. Assuming constant temperature and density on a flux surface, this leads to varying gradients in real space, which now depend on the helical phase of the non-axisymmetric perturbation α. During the rigid rotation of the magnetic perturbation field in #34548, the gradients can be measured in ELM suppression over the whole toroidal range. Figure 6.36 shows contour plots of the electron density gradient and its inverse normalized gradient length as a function of the radial position R and field-line label α. The density gradient is steepest roughly around $\alpha = 0.4\,\pi$ and $0.8\,\pi$, while $-R/L_{n_e}$ has its minimum at $\alpha = 0.45\,\pi$ to $0.6\,\pi$. The reason for the localization of the $-R/L_{n_e}$ maximum to be localized in this range is the absence of the density shoulder, which leads to the strong density gradient persisting at the foot of the pedestal at low absolute density. In the case of the ion temperature (see figure 6.37), both, the steepest gradient as well as the maximum in $-R/L_{T_i}$ are found at around $\alpha = 0.5\,\pi$. The inverse normalized electron density gradient length is comparable with the reference case except for a short phase where it is increased by a factor of up to 1.8 at around $\alpha = 0.45\,\pi$ to $0.6\,\pi$. The difference is more significant in the case of the ion temperature. Here, the maximum of the inverse normalized gradient length is at least slightly increased everywhere, peaking with an increase by a factor of roughly 4.5 to 5 at $\alpha \approx 0.5\,\pi$.

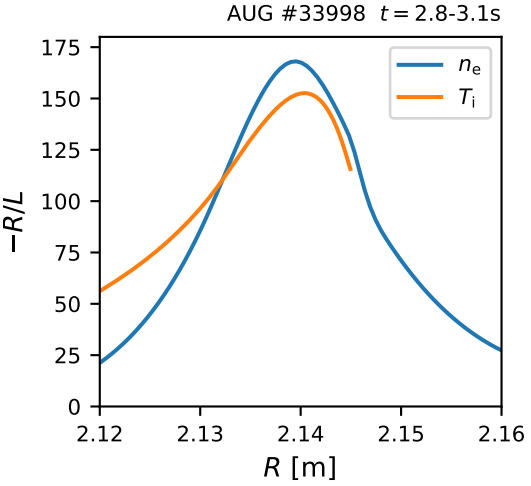

Figure 6.35: Radial profiles of the inverse normalized gradient lengths of electron density (blue) and ion temperature (orange) for the reference case without magnetic perturbations.

6.5.2 Radial Electric Field

In section 1.1, a possible mechanism for turbulence suppression is introduced emphasizing the importance of the radial electric field E_r. The radial E_r profile measured by CXRS is shown in figure 6.38 for the reference case. There, also the separate terms included in the radial ion force balance equation (see equation 2.6) used for the calculation of the radial electric field are plotted. The E_r well has a minimum of roughly 25 kV/m and its contributions from the poloidal and diamagnetic terms are about the same, while the contribution of the toroidal term is relatively small. The radial electric field measured during ELM suppression with magnetic perturbations is plotted in figure 6.39. The strongest E_r well is located in the same phase as the steepest ion temperature gradient, which is around $\alpha = 0.4\,\pi$ to $0.65\,\pi$. Due to the variation of the ion temperature gradient in the 3D geometry, also the diamagnetic term contributing to the radial electric field via the ion force balance equation is varying significantly. At the same time, the contributions

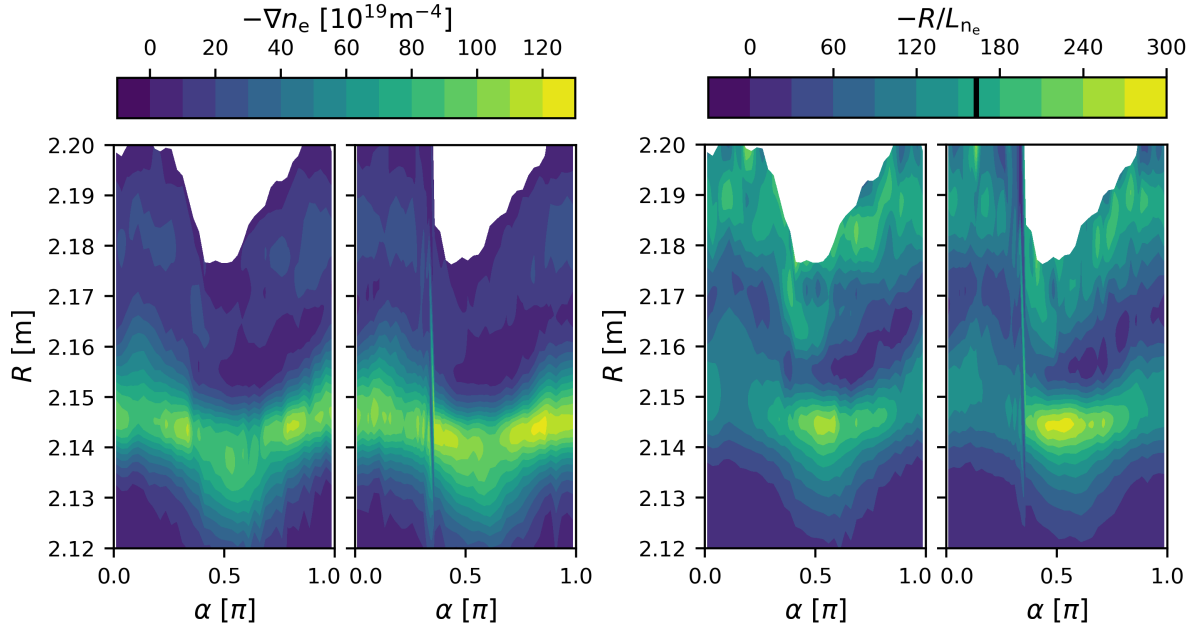

Figure 6.36: Contour plots of the electron density gradient and its inverse normalized gradient length for the two rotation periods of #34548 plotted as a function of the radial position and the field-line label α. The black bar in the color map indicates the value without MP field. Here, α is always calculated just inside the separatrix.

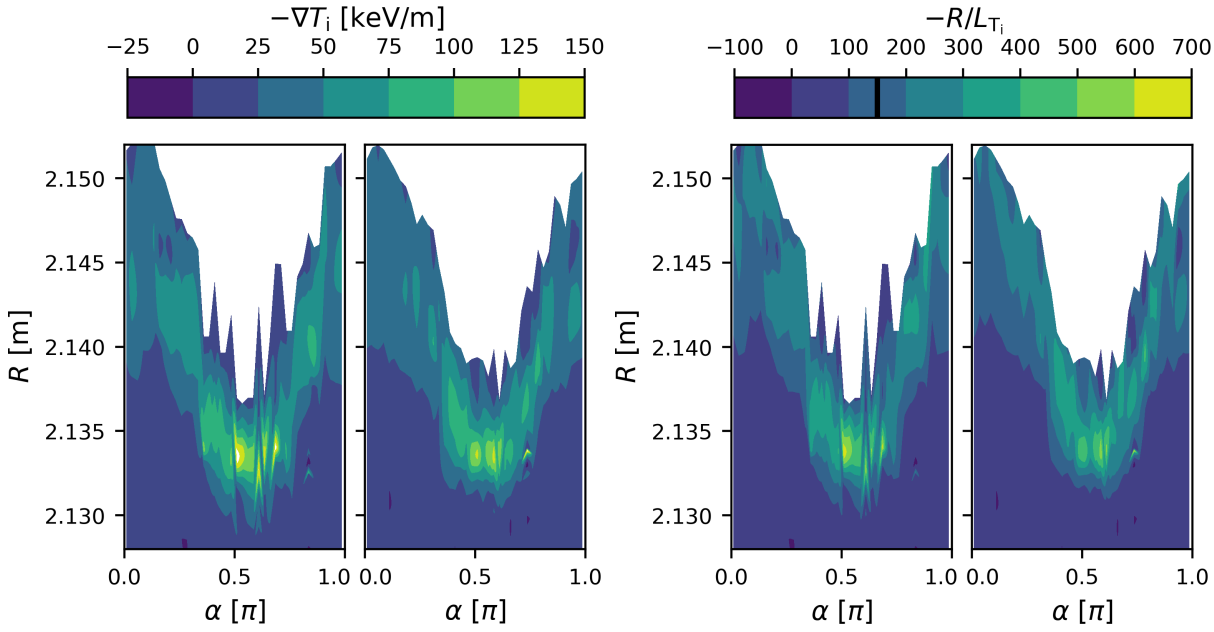

Figure 6.37: Contour plots of the ion temperature gradient and its inverse normalized gradient length for the two rotation periods of #34548 plotted as a function of the radial position and the field-line label α. The black bar in the color map indicates the value without MP field. Here, α is always calculated just inside the separatrix.

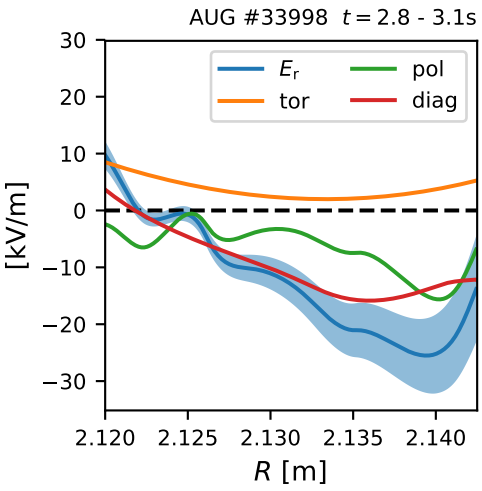

Figure 6.38: Radial profile of the radial electric field in the edge of the plasma for the reference case without magnetic perturbations. Here, the different profiles refer to the toroidal (tor), poloidal (pol) and diamagnetic (diag) terms in the force balance equation as introduced in section 2.2.2.

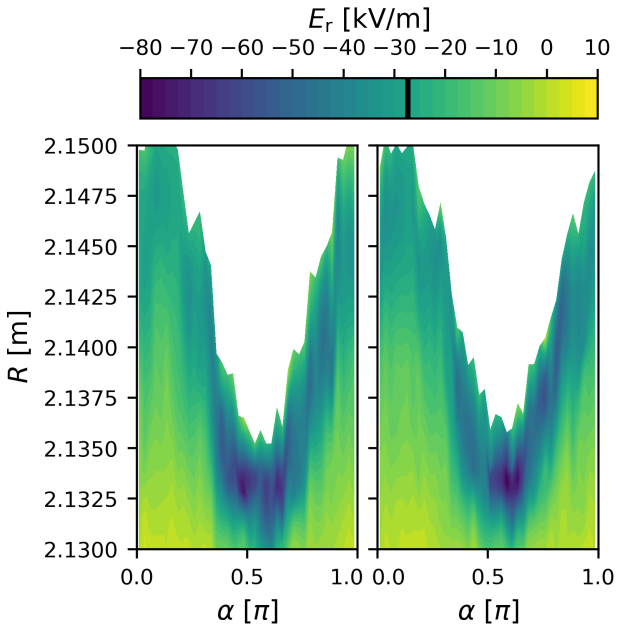

Figure 6.39: Contour plot of the radial electric field for the two rotation periods of #34548 plotted as a function of the radial position and the field-line label α. The black bar in the color map indicates the value without MP field. Here, α is always calculated just inside the separatrix.

from the toroidal and poloidal rotation velocities hardly change. This leads to a maximum depth of the E_r well of roughly $80\,\mathrm{kV/m}$ at $\alpha \approx 0.5\,\pi$. At $\alpha \approx 0$ or $1\,\pi$, the E_r well is comparable with the reference case with a maximum depth of roughly $30\,\mathrm{kV/m}$.

6.6 Summary & Discussion

In the previous sections, phenomena related to turbulence in the edge of the plasma and their relation to radial transport have been studied experimentally. The measurements suggest that at least two mechanisms play a role in the enhanced radial transport due to magnetic perturbations in ELM suppression. The first effect correlates with the fast initial decay of the magnetic perturbation field and might be related to neoclassical phenomena. The second effect sets in when the magnetic perturbation amplitude has already dropped significantly and density fluctuations, which are present during ELM suppression, are vanishing. In this section, the second effect related to turbulence is discussed with regard to the observation of broadband turbulence at reduced amplitude of the magnetic perturbation field. Possible micro-instabilities driving the broadband turbulence are identified. Towards the maximum amplitude of the magnetic perturbation field, the governing turbulence changes its characteristics from a broadband structure to a quasi-coherent mode, which is described afterwards also with regards to radial transport.

6.6.1 Broadband Turbulence

Toroidal and LFS-HFS Asymmetry

With the application of a magnetic perturbation field, the toroidal symmetry of a tokamak gets broken and, consequently, toroidal asymmetries may emerge. While diagnostics measure at fixed positions, the magnetic perturbation coil system at ASDEX Upgrade (see section 2.1) allows for rigid rotations of the perturbation field in toroidal direction in order produce toroidal scans in each diagnostic. In a discharge with a long ELM suppression phase (#34548), such a rigid rotation was performed (see figure 6.2) with the goal to investigate the toroidal symmetry properties of the edge turbulence observed with MPs. The surface corrugation due to the MP field was measured by density and temperature profile diagnostics (e. g. Li-BES, see figure 6.3) and, after a correction for the additional movement induced by the plasma control system, is compared to the corrugation as predicted by the 3-dimensional equilibrium code VMEC in figure 6.4. A good agreement is found for both, amplitude and phase of the corrugation pattern. In order to map measurements into the phase of the corrugation pattern, the toroidal angle ϕ is not sufficient, due to the helical structure of the corrugation. Therefore, the coordinate α as introduced in section 6.1 is used for the mapping.

Previous density fluctuation measurements with beam emission spectroscopy at DIII-D showed increased density fluctuations during ELM suppressed H-modes [89]. Also, a toroidal asymmetry was found [90], however, only two different toroidal angles have been investigated by switching the polarization of the MP field coil currents. Recently at EAST, a turbulent mode localized in an $n = 1$ helical perturbation field in an ELM suppressed discharge has been observed during rigid rotations of the MP field [91, 92]. However, evidence for the observed broadband fluctuations and the mode to cause radial transport has not been given. At ASDEX Upgrade, the reflectometry measurements during the

toroidal scan in #34548 (see figure 6.10) also reveal a toroidal asymmetry, which has the same toroidal mode number as the MP field. While broadband density fluctuations can be observed over most of the toroidal range, the fluctuation level is reduced in a narrow range in both periods at around $\alpha = 0.4\,\pi$ to $0.47\,\pi$ in the Ka-band on the LFS, which measured in the steep gradient region just inside the separatrix. This phase of reduced density fluctuation level in the MP induced surface corrugation pattern is dubbed the 'fluctuation gap'. In this fluctuation gap, the integrated power spectral density is minimal in both periods at $\alpha \approx 0.46\,\pi$. A way more narrow fluctuation gap is also observed in the K-band measurement probing the fluctuations in the scrape-off layer, which centers also around $\alpha = 0.46\,\pi$. As shown in figure 6.11, in the fluctuation gap the fluctuation level is reduced for frequencies of up to 150 kHz. In this frequency range, the difference in fluctuation power as compared between inside and outside the fluctuation gap increases towards lower frequencies. At frequencies above 150 kHz, no toroidal asymmetry can be seen. Although the fluctuation gap does not exist on the HFS (see figure 6.12), the fluctuations there also change slightly in time. However, both rotation periods are not comparable and, hence, these changes cannot be attributed to the phase of the magnetic perturbation field. On the LFS, the magnetic field curvature is in the direction of the pressure gradient and, therefore, can become ballooning unstable. The observed HFS-LFS asymmetry indicates that the micro-instability driving the turbulence is sensitive to ballooning stability.

Radial Transport

Even though the observed broadband density fluctuations are known to exist only in the presence of the magnetic perturbation field, their observation by itself is not a proof that they cause net radial transport and, therefore, possibly contribute to the pump-out effect. The average electrostatic radial particle flux in particular depends on the phase between density fluctuations and electric potential fluctuations. However, fluctuations of the electric potential cannot be measured in the confined region at ASDEX Upgrade. In order to investigate whether or not the observed density fluctuations cause actual net radial transport, a comparison with scrape-off layer properties is done. In the scrape-off layer, a density shoulder can be observed by Li-BES during the ELM suppressed phase in #34548 (see figure 6.13). Density shoulders can be described as a flattening of the density profile in the scrape-off layer as a consequence of increased convective cross-field transport due to filaments [93, 94, 95, 96, 97, 98]. Filaments, which are generated at the separatrix during nonlinear saturation processes of edge turbulence, e. g. broadband turbulence due to interchange instabilities [99]. In #34548, the height of the density shoulder depends on the helical field-line label α, whereas the density shoulder completely vanishes in the fluctuation gap. Accordingly, this is an indication for a connection between turbulence in the steep gradient region and cross-field transport in the scrape-off layer. Furthermore, Langmuir probes were used on the outer divertor in order to measure density and temperature fluctuations in the scrape-off layer. In the time traces of electron temperature and density measured by the different probes (e. g. *8ua7* in figure 6.14) one can see intermittent structures during the two rigid rotation

periods from $t = 3$ to 7 s. This supports the hypothesis that filamentary transport forms the density shoulder in the scrape-off layer as observed by Li-BES. Furthermore, in both periods a phase with reduced filament frequency and amplitude can be observed indicating a toroidal asymmetry. Comparing this pattern between all the available Langmuir probes on the outer divertor (see left plots in figures 6.15 and 6.16) shows that the phase of reduced filament frequency and amplitude can be observed in all probes in the scrape-off layer (not in the private flux region, probe *8ua1*), though, in each probe with a different time shift. This can be explained by the fact that Langmuir probes mounted at different radial positions are connected via the open field lines with different toroidal positions on the midplane. Field lines in contact with each Langmuir probe can be traced up until they intersect with the horizontal plane on which the reflectometry data was taken, which observed the toroidally asymmetric density fluctuations (see figure 6.18). The Langmuir probe data was then mapped onto α at this intersection point on the right-hand plots of figures 6.15 and 6.16. Plotted against α, the reduced intermittency occurs at approximately the same phase at around $\alpha = 0.5\,\pi$. However, the width of the phase with reduced intermittency is not constant in all probes and also not always exactly centered around $\alpha = 0.5\,\pi$. Furthermore, this comparison can just be made for fluctuations of up to 11 kHz due to measurement constraints of the Langmuir probes. Nevertheless, the toroidal asymmetry was strongest at low frequencies making a comparison reasonable. In addition to the toroidal asymmetry, a sudden drop in density fluctuation amplitude can be observed between probe *8ua8* and *8ua9*. These probes are approximately separated by the magnetic flux surface with $\rho_{\mathrm{pol}} = 1.075$ (see figure 6.17), which is about where the density shoulder ends (see figure 6.13). Hence, the filaments creating the density shoulder might be responsible for the intermittent density and fluctuations measured with Langmuir probes on the divertor. These measurements suggest a causal relationship between particle flux events (e. g. filaments) observed at different radial positions on the divertor target, the formation of a toroidally asymmetric density shoulder in the scrape-off layer and density fluctuations at corresponding toroidal positions in the steep gradient region. Therefore, these observations demonstrate how particle transport is associated with the observed toroidally asymmetric density fluctuations related to the magnetic perturbation field.

Density and Temperature Gradients

A comparison between the gradients of electron density and ion temperature during the ELM suppressed rigid rotation of #34548 and the gradients in the ELMy reference discharge #33998 was done in section 6.5. During ELM suppression, the inverse normalized density gradient length $R/L_{\mathrm{n_e}}$ is comparable to the ELMy reference except for a short interval around $\alpha \approx 0.5\,\pi$, which is where the density shoulder disappears (see figure 6.35 and 6.36) allowing for steeper profiles at the foot of the pedestal. In this phase the inverse normalized density gradient length is about a factor of 1.6 larger than in the reference case. On the other hand, the inverse normalized ion temperature gradient length $R/L_{\mathrm{T_i}}$ during ELM suppression is increased over the whole toroidal range peaking also at around $\alpha \approx 0.5\,\pi$ with a factor of 4 to 5 higher than in the ELMy reference case (see figure 6.35 and 6.37).

While the pedestal top temperatures and density are constant during the rigid rotation, the variation of their gradients is produced by a variation of the width of the pedestal. As a consequence of the steepening of the electron density and ion temperature gradients in ELM suppression, also the pressure gradient is increased. Strong pressure gradients in the plasma are a source of free energy which can drive micro-instabilities responsible for turbulence in the plasma. Since the turbulence gap is observed at the position of the largest inverse normalized gradient length of both, the electron density and ion temperature, these gradients cannot be the cause for the toroidal asymmetry of the turbulence. However, the gradients - especially the ion temperature gradient - are significantly increased over the whole toroidal range as compared to the reference case without magnetic perturbations and can act as a drive for turbulence. The fact that the gradients are largest inside the fluctuation gap can be a consequence of the reduced turbulent transport in this phase, which in turn allows for the gradients to steepen.

ExB Shear Suppression

In addition, due to the narrow ion temperature pedestal and the accompanied strong ion temperature gradient, the radial electric field has the deepest well in the very same phase of $\alpha \approx 0.5\,\pi$ due to its ion diamagnetic term $-\frac{\nabla p_\mathrm{i}}{Z_\mathrm{i} n_\mathrm{i}}$ as shown in figure 6.39. Figure 6.40(a) compares the radial electric field profile at $\alpha \approx 0.0$ and $0.46\,\pi$ as measured by CXRS. Not only is the E_r well deeper at $0.46\,\pi$ by a factor of roughly 2, but also the profile is narrower in the lab frame. As a consequence, the difference in the ExB shearing rate [100]

$$\omega_\mathrm{ExB} = \frac{r}{q}\frac{\partial}{\partial r}\left(\frac{q}{r}\frac{E_\mathrm{r}}{B}\right) \tag{6.4}$$

is even more significant as it can be seen in figure 6.40(b). Both, the negative ExB shearing rate before the E_r minimum and the positive rate after the minimum, are larger by a factor of up to 5 at $\alpha \approx 0.46\,\pi$ as compared to $\alpha \approx 0$. As introduced in section 1.1, a possible mechanism for turbulence suppression is the decorrelation of turbulent eddies through ExB shearing. Hence, the aforementioned local variations of the ExB shearing rate within the magnetic perturbation pattern are a possible explanation for the fluctuation gap, in which turbulence is suppressed.

Phase Velocity

From the radial electric field E_r as measured by CXRS and the magnetic field as obtained from the magnetic equilibrium, the accompanied drift velocity v_ExB can be calculated. Furthermore, measurements of the perpendicular propagation velocity $v_\perp$ of turbulent structures are obtained from Doppler reflectometry (DRFL, introduced in section 2.2.1). This velocity can be divided into two contributions $v_\perp = v_\mathrm{ExB} + v_\mathrm{ph}$ with the phase velocity of turbulent structures v_ph, which is often assumed to be negligible. However, when v_ph contributes a significant fraction to $v_\perp$, it can be calculated as the difference between the ExB velocity and perpendicular velocity as measured by CXRS and Doppler reflectometry,

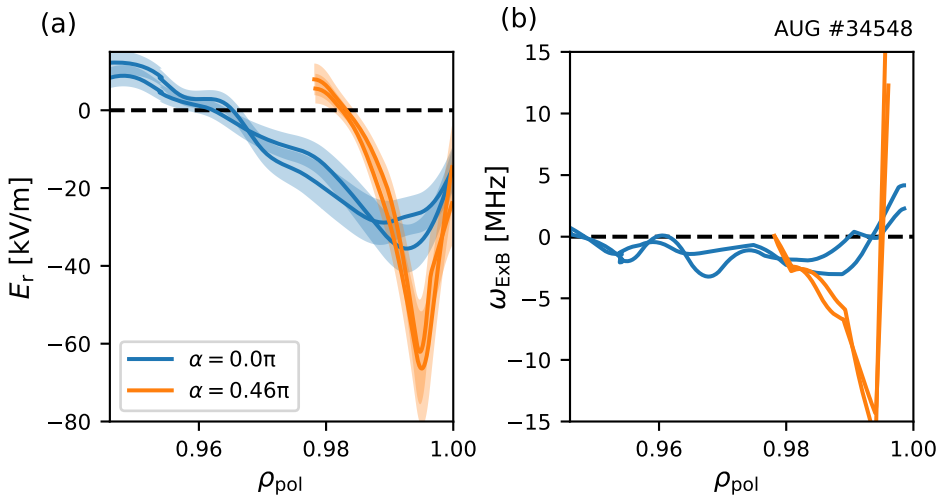

Figure 6.40: (a) Comparison of radial electric field profiles measured with CXRS at the phase of the fluctuation gap ($\alpha = 0.5\,\pi$) and a phase outside the fluctuation gap ($\alpha = 0$). (b) The corresponding ExB shearing rates.

respectively. In figure 6.41, the ExB velocity as calculated from CXRS measurements and the perpendicular velocity obtained from DRFL measurements are compared for two different phases in the magnetic perturbation pattern. For this comparison, both, the CXRS and DRFL measurements are mapped on the midplane, since at varying poloidal angles the magnetic flux surface compression varies leading to differences in the radial electric field. At $\alpha \approx 0.85\,\pi$ good agreement between both velocities can be found, suggesting a negligible phase velocity in this case. However, at $\alpha \approx 0.55\,\pi$ the $v_\perp$ profile flattens throughout the steep gradient region, while the v_{ExB} profile maintains its peaked shape. In this case, also the minimum of the ExB velocity shows a significant deviation from the minimum of the perpendicular velocity. The minima of the ExB velocity as well as the perpendicular velocity at the radial position of the corresponding ExB velocity minimum are shown in figure 6.42(a) as a function of α. In the phase from $\alpha \approx 0.7\,\pi$ to $0.9\,\pi$ the ExB and perpendicular velocity are approximately equal. Outside this phase, a significant offset between both velocities can be observed. Consequently, in this case the phase velocity is not negligible but amounts significantly to the measured perpendicular velocity. The calculated phase velocity is plotted in figure 6.42(b) as a function of α. Outside the phase of good agreement from $\alpha \approx 0.7\,\pi$ to $0.9\,\pi$, the phase velocity is not constant but varies between 10 to 30 km/s. In the v_{ExB} frame moving with this plasma, this phase velocity is pointing in the ion diamagnetic direction. For the α range from approximately 0 to $0.7\,\pi$ and $0.9\,\pi$ to $1.0\,\pi$ where CXRS and DRFL measurements differ, the Doppler shifted back-scattered signal measured with DRFL is very pronounced and forms a distinct peak at $f \approx 1.3$ MHz as it can be seen in the blue spectrum in figure 6.43 for $\alpha \approx 0.5\,\pi$. In this case, a Gaussian fit to the asymmetric component of the spectrum is very precise. However, for the phase with measurements in agreement (orange spectrum), the Doppler shifted back-scattered signal is very weak

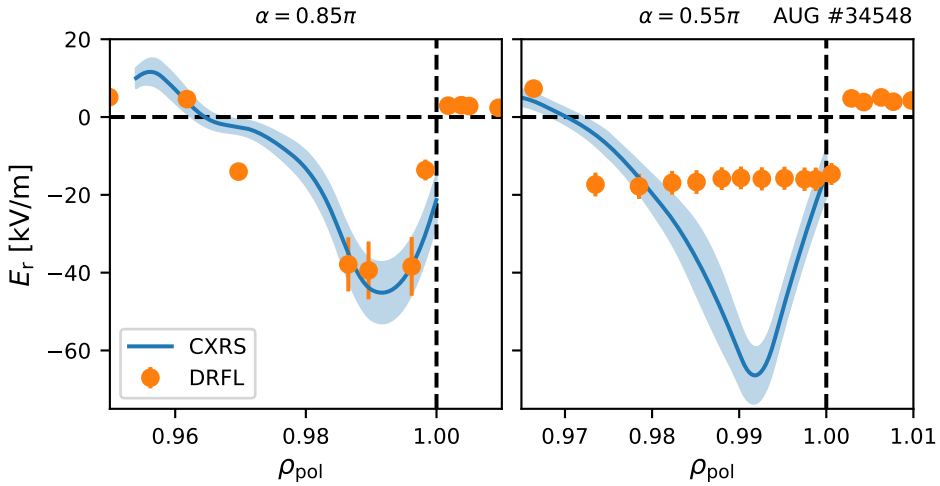

Figure 6.41: Comparison of the radial electric field calculated from CXRS measurements with the radial electric field as approximated from DRFL measurements. A phase with good ($\alpha = 0.85\,\pi$) and a phase with bad agreement ($\alpha = 0.55\,\pi$) between both velocities is shown.

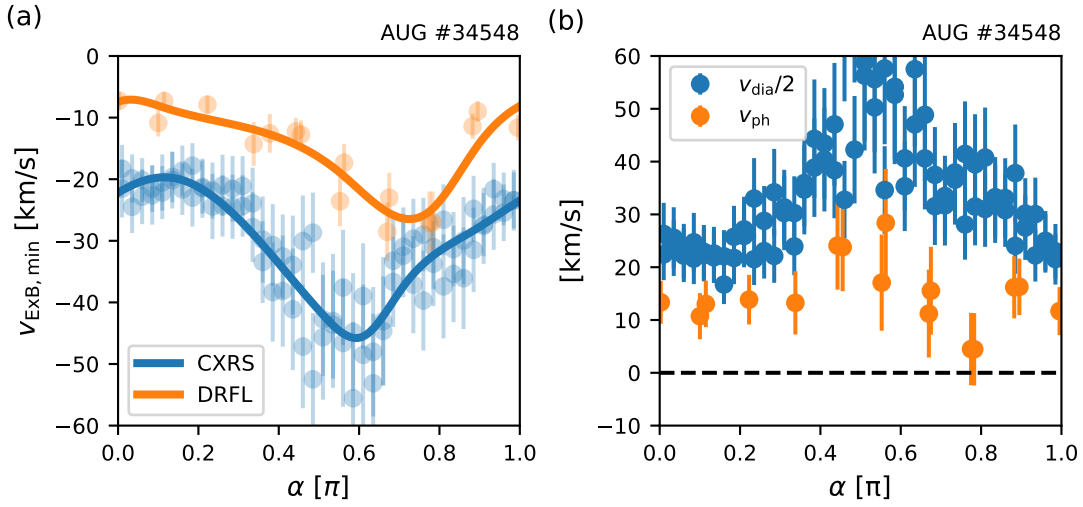

Figure 6.42: (a) Comparison between the minimum of the ExB velocity and perpendicular velocity profiles as a function of α. (b) Calculated phase velocity and half main ion diamagnetic velocity as a function of α. Here, α is always calculated just inside the separatrix.

and no distinct peak can be seen in the spectrum. Rather a plateau is formed at around $f \approx 3.0\,\mathrm{MHz}$ and the Gaussian fit is, hence, less precise leading to larger uncertainties in the calculated $v_\perp$ or v_{ExB} (as it can be seen in figure 6.41). A second shoulder-like signal structure can be seen at about $f \approx 0.6\,\mathrm{MHz}$, which could be picked up on the path of the probing beam through the turbulent plasma edge to the cut-off layer. Nevertheless, this does not appear in all Doppler reflectometry measurements in this radial range and phase of magnetic perturbation, while the plateau at $f \approx 3.0\,\mathrm{MHz}$ does. This gives us confidence, that the latter one is the real Doppler shifted back-scattered signal at the cut-off layer. If the difference between CXRS and DRFL is indeed due to an underlying turbulent mode with the calculated phase velocity, then it would be conclusive if the intensity of the Doppler-shifted peak at the phase of vanishing phase velocity, i. e. absence of the turbulent mode, is lower since the back-scattered intensity depends on the density fluctuation level at the cut-off layer.

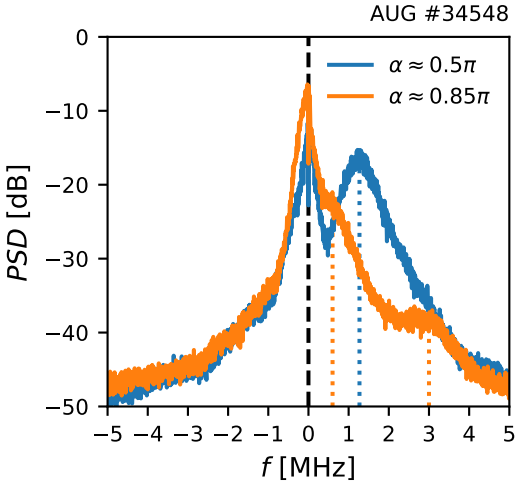

Figure 6.43: Power spectral density of the Doppler reflectometry in a phase with good ($\alpha = 0.85\,\pi$) and a phase with bad agreement ($\alpha = 0.5\,\pi$) with CXRS measurements.

Identification of Micro-Instabilities

Broadband plasma turbulence is induced by non-linearly saturated micro-instabilities, which can be distinguished by their properties such as their transport characteristics, drive, phase velocity, parity and scale. In [101, 102] a condensed list of such micro-instabilities is given together with their important fingerprints, which can be measured in the plasma (summarized in table 6.1). In figure 6.42(b) the measured phase velocity is plotted together with a calculation of half the main ion diamagnetic velocity v_{dia}. For the calculation of the main ion diamagnetic velocity the assumption is made that the electron and main ion densities are equal. While the uncertainties in both quantities are rather large, it can be seen that the phase velocity can approach half the main ion diamagnetic velocity within the errorbars. Also the the same trend, i. e. increase in both velocities from $\alpha \approx 0$ to $0.5\,\pi$, can be seen. Typical micro-instabilities traveling into the ion diamagnetic direction are MHD-like modes such as the kinetic ballooning mode (KBM) and the ion temperature gradient (ITG) mode, both of which are driven by strong ion temperature gradients. While the gradient of the electron density is just increased slightly with the application of magnetic perturbations, the ion temperature gradient increases very significantly (see section 6.5). While the phase velocity of ITGs are rather low, KBMs can reach phase velocities of around $0.5 \cdot v_{\mathrm{i,dia}}$. Within the errorbars, this could not be distinguished from the measurements. Both, ITG and KBM have a ballooning character

Mode	KBM	MTM	ETG	ITG	TEM
Drive	$\nabla T_{\mathrm{e,i}}$	∇T_{e}	∇T_{e}	∇T_{i}	∇T_{e}, ∇n
Direction	i	e	e	i	e
Frequency	$\omega \approx \omega_{\mathrm{i,dia}}/2$	$\omega \approx \omega_{\mathrm{e,dia}}$		$\omega \ll \omega_{\mathrm{i,dia}}/2$	$\omega \ll \omega_{\mathrm{e,dia}}$
Scale	$k_\theta \rho_{\mathrm{s}} \approx 0.1$	$k_\theta \rho_{\mathrm{s}} \approx 0.1$	$k_\theta \rho_{\mathrm{s}} > 1$	$0.1 < k_\theta \rho_{\mathrm{s}} < 1$	$k_\theta \rho_{\mathrm{s}} > 0.1$
Parity	ball.	tear.	ball.	ball.	ball.
$\chi_{\mathrm{i}}/\chi_{\mathrm{e}}$	≈ 1	$\approx 1/10$	$\approx 1/10$	≈ 1 to 4	

Table 6.1: Characteristics of relevant micro-instabilities including the kinetic ballooning mode (KBM), micro tearing mode (MTM), electron/ion temperature gradient mods (ETG/ITG) and trapped electron mode (TEM). This table includes the drive (by which gradient), direction (in electron or ion direction), frequency (as compared to the electron/ion diamagnetic frequency $\omega_{\mathrm{e/i,dia}}$), scale (wave number in poloidal direction times $\rho_{\mathrm{s}} = \sqrt{T_{\mathrm{e}} m_{\mathrm{i}}}/eB$), parity (tearing or ballooning) and ion to electron temperature heat conductivity ratio $\chi_{\mathrm{i}}/\chi_{\mathrm{e}}$). Values are taken from [101, 102].

which can explain the observation that the toroidally asymmetric density fluctuations have been measured on the LFS, but not on the HFS. In the region of the E_{r} well, the Doppler reflectometry measured at scales of $k_\theta \rho_{\mathrm{s}} \approx 0.5$ to 1.5 with $\rho_{\mathrm{s}} = \sqrt{T_{\mathrm{e}} m_{\mathrm{i}}}/eB$, which is rather in the range of ITG modes ($0.1 < k_\theta \rho_{\mathrm{s}} < 1$) than KBMs ($k_\theta \rho_{\mathrm{s}} \approx 0.1$). Nevertheless, large scale turbulence (i. e. small $k_\theta \rho_{\mathrm{s}}$) is expected to transfer energy into smaller scales making it possible that turbulence due to KBMs can be observed when measured at higher $k_\theta \rho_{\mathrm{s}}$. The ratio of ion χ_{i} to electron χ_{e} heat conductivity in the case of the edge region of #34548 is calculated from the power balance and is plotted in figure 6.44. In the radial region of the E_{r} well ($\rho_{\mathrm{pol}} > 0.96$), this ratio is below unity going down to about 0.7. This is the order of the KBM or lower end of the ITG mode turbulence. KBMs generally cause significant particle as well as impurity particle transport, which could explain the density pump-out as well as the absence of significant impurity accumulations. The effect of ITG turbulence on the particle diffusivity is smaller, however, in the ELM suppression scenario hardly any gas is puffed (0 to $1 \cdot 10^{21}$particles/s) and in the presence of such small particle sources small changes in the diffusivity can already have strong effects on the density.

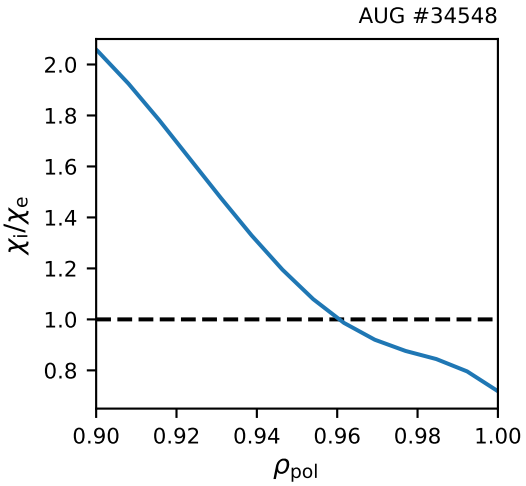

Figure 6.44: Radial profile of the ion χ_{i} to electron χ_{e} heat conductivity ratio obtained from the power balance.

In summary it can be said, therefore, that experimental fingerprints point strongly into the direction of a kinetic ballooning mode or ion temperature gradient mode to be governing edge turbulence during ELM suppression with magnetic perturbations.

6.6.2 Quasi-Coherent Mode

In section 6.3 it was shown that a quasi-coherent mode appears when the plasma transitions into an ELM suppressed regime with magnetic perturbations at a sufficiently high amplitude. The appearance of this mode coincides with the onset of an additional decrease of the electron density, indicating its possible influence on particle confinement. Also, when the magnetic perturbation is switched off during ELM suppression, the quasi-coherent mode disappears just before the density starts to increase. The mode itself is localized in the steep gradient region inside the confined plasma up to the top of the pedestal on the low-field side of the torus. However, it can also be observed in the scrape-off layer when steep gradients are present there. Its expansion in radial direction becomes smaller, the lower the amplitude of the perturbation is. Ultimately, it narrows down to a small region close to the pedestal top before it then completely vanishes at even lower amplitude. When the perturbation field amplitude was modulated in such a range that the quasi-coherent mode periodically appears and disappears, it was found that the presence of this mode leads to increased density fluctuations in the divertor region and the density becomes stationary. Due to its dependence on the perturbation field amplitude, this mode was not observed consistently during discharges with rigid rotations of the perturbation field, since these have intrinsically smaller amplitudes. Nevertheless, in #35929 a rigid rotation of the perturbation field was performed and the quasi-coherent mode was observed in the first of the three rotation periods. In the second period, just a flattening of the spectrum was seen while no mode or flattening was observed in the third period. This difference between the rotation periods might result from the fact that the measurement position was moving further away from the pedestal top during the discharge due to the steadily increasing density. Furthermore, the $n = 2$ amplitude was higher during the first rotation period as compared to the two following rotation periods, which could be the reason why the quasi-coherent mode was observed there. Due to the wrong wiring, a calculation of the surface corrugation was not possible, however, the toroidal location of the quasi-coherent mode can be determined by comparing it to the broadband turbulence. Here it was found, that the mode is localized at the same phase in the surface corrugation pattern like the broadband fluctuation gap, which was found previously to be located at the helical field-line label $\alpha \approx 0.35\,\pi$ to $0.55\,\pi$.

The observation suggests that a quasi-coherent mode located in the steep gradient region and in a certain phase of the MP induced surface corrugation could be responsible for the additional density decrease during the transition from ELM mitigation into ELM suppression.

Chapter 7

Summary & Outlook

At ITER-like low collisionality, the application of a radial magnetic perturbation (MP) field can mitigate or even suppress Edge Localized Modes (ELMs). These magnetic perturbations also cause a reduction of particle and energy confinement, leading to a strong decrease of density in the plasma: the density pump-out effect. The physical mechanisms for enhanced particle transport and suppression of the ELM instability by small non-axisymmetric magnetic perturbations of tokamak plasmas are investigated in this thesis.

The plasma density reduction by a magnetic perturbation can be described by an increase of the diffusion coefficient at the plasma edge, in the H-mode pedestal and steep gradient region. This is demonstrated by magnetic perturbation strength modulations causing a density perturbation, which travels inward from the edge into the core plasma (see chapter 4). The propagation of the density waves induced at the edge towards the plasma core can be reproduced in a transport simulation with ASTRA, in which the MP field enters as a modulation of the electron diffusion coefficient at the pedestal top. This suggests that the rearrangement of the core density is a mere reaction to the altered pedestal top density.

For neoclassical transport, i. e. collisional transport in presence of enhanced radial particle orbit width in toroidal geometry, a strongly enhanced radial diffusivity is expected if gyrocenter motion is resonant with an applied non-axisymmetric magnetic perturbation. This is tested experimentally in chapter 5 by shifting resonant surfaces (locations of largest plasma displacement) radially relative to the location of $ExB = 0$ (gyrocenter motion in resonance with the static magnetic perturbation). No dependence of particle transport is found if these positions overlap, indicating that neoclassical transport is not the dominant transport effect by magnetic perturbations.

The decisive hint for the transport mechanism is given by the observation of turbulence in the steep gradient region which occurs whenever the particle transport is increased and ELMs are suppressed in H-mode (see chapter 6). In the presence of the MP field with an amplitude below a certain threshold, broadband density fluctuations can be observed in the steep gradient region on the low-field side close to the midplane. A toroidal asymmetry appears as these fluctuations can be observed over a wide toroidal range and a narrow gap,

in which the fluctuations are absent, can be identified. This gap is dubbed the fluctuation gap. The fluctuation gap is localized within the surface corrugation in a phase where the absolute value and shear of the radial electric field in the steep gradient region are largest. At toroidal angles where the density fluctuations are present, the density profile in the near scrape-off layer features a shoulder form, which is indicative for filamentary transport. Furthermore, at locations on the divertor, which are connected via field lines with the very same toroidal angles, strong density and temperature fluctuations can be observed. In contrast, at the toroidal range of the fluctuation gap the density profile shows no signs of a shoulder and the fluctuations at the corresponding locations on the divertor plates are significantly weaker. The measured phase velocity is in ion diamagnetic drift direction, which narrows down the range of candidates for the underlying micro-instabilities to, e. g. kinetic ballooning modes or the ion temperature gradient mode. When the amplitude of the MP field exceeds a certain threshold, a quasi-coherent mode can be seen in measurements of the density fluctuations in the steep gradient region on the low-field side close to the midplane. Its phase within the surface corrugation pattern overlaps with the position of the fluctuation gap at reduced amplitude. When this mode is present, enhanced intermittency can be observed in the divertor region and the electron density is completely stationary, while in the absence of the mode, the electron density slightly increases throughout a discharge. These results suggest that turbulence in the edge increases with the application of radial magnetic perturbations and contributes significantly to the density pump-out.

Based on the observation on turbulent transport during the suppression of ELMs, a new hypothesis for the mechanism of their suppression with radial magnetic perturbations can be formulated. ELMs will be suppressed, if the edge pedestal pressure and current profiles can be clamped by an alternative transport mechanism to below the critical values for ELM destabilization. The observed edge turbulence is seen to cause transport across the pedestal and may take on this role. Depending on the underlying micro-turbulence mechanism, it may provide profile stiffness, i. e. clamp edge pressure profiles for a wider range of heating power, as observed in the experiment.

Outlook

Further work has to be done in order to test the hypothesis for the suppression of ELMs based on turbulent transport made in this thesis. A first step would be to find out whether the here presented turbulence features are a general characteristic of ELM suppressed H-modes by investigating their occurrence in different devices and different MP field geometries (such as toroidal mode number $n \neq 2$). While [75] suggests that ELM suppressed H-modes operate at reduced pressure as compared to ELMy H-modes, 3-D stability calculations (e. g. with PB3D [103]) could help to clarify whether the observed turbulence really establishes H-mode pedestals, which are below the stability boundary of ELMs, or not. Furthermore, the general observation of the q_{95} windows as a criterion for ELM suppression has to be investigated with regards to its connection to turbulence in the steep gradient region and pedestal top. The identification of the type of instability and its

interaction with q_{95} could be supported by gyro-kinetic simulations with GENE-3D [104] once it includes electro-magnetic effects.

Appendix A

List of abbreviations

ASDEX AxiSymmetric Divertor EXperiment
ASTRA Automated System for TRansport Analysis
AUG AxiSymmetric Divertor EXperiment Upgrade
CLISTE CompLete Interpretive Suite for Tokamak Equilibria
CXRS Charge eXchange Recombination Spectroscopy
DCN Deuterium CyaNide interferometry
ECE Electron Cyclotron Emission Radiometry
ECRH Electron Cyclotron Resonance Heating
ELM Edge Localized Mode
ETB Edge Transport Barrier
He-BES Helium Beam Emission Spectroscopy
HFS High Field Side
H-mode High confinement mode
ICRH Ion Cyclotron Resonance Heating
IDA Integrated Data Analysis
LFS Low Field Side
Li-BES Lithium Beam Emission Spectroscopy
L-mode Low confinement mode
MP Magnetic Perturbation
NBI Neutral Beam Injection
OH Ohmic Heating
PSL Passive Stabilization Loop
TS Thomson Scattering
VMEC Variational Moments Equilibrium Code

Appendix B

General Information on the ASTRA Simulations

The 1-dimensional transport code ASTRA [80] is used in this thesis in two ways. Firstly, it is used interpretative in order to determine the electron and ion power balance heat conductivity. Secondly, it is used predictive in order to simulate the density evolution in the core of the plasma. In both cases, the code solves a set of transport equations (see Chapters 3.6 and 4.2 in [80]) using thermodynamic forces for the expression of the fluxes. For the closure of the transport equations, time dependent metric coefficients are provided by coupling of ASTRA to the equilibrium code SPIDER [105, 106] and initial conditions for the electron density, electron temperature, ion temperature and toroidal rotation have to be given as well as general plasma and device parameters.

The neutral particle source and the source from the neutral beam injection heating system are given by the NEUT and NBI modules, respectively. The NBI module also calculates the power deposition profiles for electrons and ions. Power exchange between electrons and ions based on coulomb collisions is also included. The power deposition profile of the electron cyclotron resonance heating system is calculated by the TORBEAM code and put into ASTRA. Furthermore, the ohmic heating power is calculated by ASTRA. The radiated power due to electron Bremsstrahlung is included as well as an approximation of the radiation by tungsten impurities. Knowing the power sources and sinks, the power balance heat conductivity for electrons and ions is calculated.

Bibliography

[1] IAEA. https://www-nds.iaea.org/exfor/exfor.htm (data taken on the 27th of December 2019).

[2] J. D. Lawson, "Some criteria for a power producing thermonuclear reactor," in *Proceedings of the Physical Society, Section B*, vol. 70, 1957.

[3] M. Greenwald, J. Terry, S. Wolfe, S. Ejima, M. Bell, S. Kaye, and G. Neilson, "A new look at density limits in tokamaks," *Nucl. Fusion*, vol. 28, no. 12, 1988.

[4] M. Greenwald, "Density limits in toroidal plasmas," *Plasma Phys. Control. Fusion*, vol. 44, pp. R27 – R80, 2002.

[5] B. Zohuri, *Inertial Confinement Fusion Driven Thermonuclear Energy*, ch. 3.5 Lawson criterion. Springer International Publishing, 2017.

[6] ITER Physics Expert Group on Confinement and Transport, "Chapter 2: Plasma confinement and transport," *Nucl. Fusion*, vol. 39, no. 12, 1999.

[7] H. Zohm, "On the minimum size of DEMO," *Fusion Science and Technology*, vol. 58, pp. 613 – 624, 2010.

[8] H. Zohm, "On the size of tokamak fusion power plants," *Phil. Trans. R. Soc. A*, vol. 377, no. 20170437, 2019.

[9] C. W. Horton and S. Benkadda, *ITER Physics*. World Scientific, 2015.

[10] ITER. https://www.iter.org/.

[11] EUROfusion. https://www.euro-fusion.org/fileadmin/user_upload/Archive/wp-content/uploads/2011/09/JG05.537-1c.jpg (taken on the 17th of December 2019).

[12] K. Miyamoto, *Plasma Physics and Controlled Nuclear Fusion*. Springer, 2005.

[13] International Atomic Energy Agency, *FUSION PHYSICS*. 2012.

[14] K. C. Shaing and E. C. C. Jr, "Bifurcation theory of poloidal rotation in tokamaks: A model for the L-H transition," *Phys. Rev. Lett.*, vol. 63, no. 21, 1989.

[15] H. Biglari, P. H. Diamond, and P. W. Terry, "Influence of sheared poloidal rotation on edge turbulence," *Phys. Fluids B*, vol. 2, no. 1, 1990.

[16] F. Wagner, G. Becker, K. Behringer, D. Campbell, A. Eberhagen, W. Engelhardt, G. Fussmann, . Gehre, J. Gernhardt, G. v. Gierke, G. Haas, M. Huang, F. Karger, M. Keilhacker, Q. Klüber, M. Kornherr, K. Lackner, G. Lisitano, G. G. Lister, H. M. Mayer, D. Meisel, E. R. Müller, H. Murmann, H. Niedermeyer, W. Poschenrieder, H. Rapp, H. Röhr, F. Schneider, G. Siller, E. Speth, A. Stabler, K. H. Steuer,

G. Venus, O. Vollmer, and Z. Yü, "Regime of improved confinement and high beta in neutral-beam-heated divertor discharges of the ASDEX tokamak," *Phys. Rev. Lett.*, vol. 49, no. 19, 1982.

[17] A. Team, "The H-Mode of ASDEX," *Nucl. Fusion*, vol. 29, no. 11, 1989.

[18] R. Groebner, K. H. Burrell, and R. P. Seraydarian, "Role of edge electric field and poloidal rotation in the l-h transition," *Phys. Rev. Let.*, vol. 64, no. 25, 1990.

[19] K. H. Burrell, "Effects of exb velocity shear and magnetic shear on turbulence and transport in magnetic confinement devices," *Phys. Plasmas*, vol. 4, no. 5, 1997.

[20] P. Sauter, T. Pütterich, F. Ryter, E. Viezzer, E. Wolfrum, G. Conway, R. Fischer, B. Kurzan, R. McDermott, S. Rathgeber, and the ASDEX Upgrade Team, "L- to H-mode transitions at low density in ASDEX Upgrade," *Nucl. Fusion*, vol. 52, no. 012001, 2012.

[21] E. Viezzer, T. Pütterich, G. Conway, R. Dux, T. Happel, J. Fuchs, R. McDermott, F. Ryter, B. Sieglin, W. Suttrop, M. Willensdorfer, E. Wolfrum, and the ASDEX Upgrade Team, "High-accuracy characterization of the edge radial electric field at ASDEX Upgrade," *Nucl. Fusion*, vol. 53, no. 053005, 2013.

[22] F. Ryter, M. Cavedon, T. Happel, R. M. McDermott, E. Viezzer, G. D. Conway, R. Fischer, B. Kurzan, T. Pütterich, G. Tardini, M. Willensdorfer, and the ASDEX Upgrade Team, "L-H transition physics in hydrogen and deuterium: key role of the edge radial electric field and ion heat flux," *Plasma Phys. Control. Fusion*, vol. 58, no. 014007, 2016.

[23] M. Cavedon, *The role of the radial electric field in the development of the edge transport barrier in the ASDEX Upgrade tokamak*. PhD thesis, Technical University of Munich, 2016.

[24] J. Schirmer, G. D. Conway, H. Zohm, W. Suttrop, and the ASDEX Upgrade Team, "The radial electric field and its associated shear in the ASDEX Upgrade tokamak," *Nucl. Fusion*, vol. 46, no. 9, 2006.

[25] H. Zohm, "Edge localized modes (elms)," *Plasma Phys. Control. Fusion*, vol. 38, no. 105, 1996.

[26] A. W. Leonard, "Edge-localized-modes in tokamaks," *Phys. Plasmas*, vol. 21, no. 090501, 2014.

[27] J. W. Connor, R. J. Hastie, H. R. Wilson, and R. L. Miller, "Magnetohydrodynamic stability of tokamak edge plasmas," *Phys. Plasmas*, vol. 5, no. 2687, 1998.

[28] H. R. Wilson, J. W. Connor, A. R. Field, S. J. Fielding, R. L. Miller, L. L. Lao, J. R. Ferron, and A. D. Turnbull, "Ideal magnetohydrodynamic stability of the tokamak high-confinement-mode edge region," *Phys. Plasmas*, vol. 6, no. 1925, 1999.

[29] P. B. Snyder, H. R. Wilson, J. R. Ferron, L. L. Lao, A. W. Leonard, T. H. Osborne, A. D. Turnbull, D. Mossessian, M. Murakami, and X. Q. Xu, "Edge localized modes and the pedestal: A model based on coupled peeling-ballooning modes," *Phys. Plasmas*, vol. 9, no. 2037, 2002.

[30] A. Loarte, G. Saibene, R. Sartori, D. Campbell, M. Becoulet, L. Horton, T. Eich, A. Herrmann, G. Matthews, N. Asakura, A. Chankin, A. Leonard, G. Porter, G. Federici, G. Janeschitz, M. Shimada, and M. Sugihara, "Characteristics of type I ELM energy and particle losses in existing devices and their extrapolation to ITER," *Plasma Phys. Control. Fusion*, vol. 45, pp. 1549–1569, 2003.

[31] T. Eich, B. Sieglin, A. Thornton, M. Faitsch, A. Kirk, A. Herrmann, W. Suttrop, JET contributors, MST contributors, ASDEX Upgrade, and MAST teams, "ELM divertor peak energy fluence scaling to ITER with data from JET, MAST and ASDEX upgrade," *J. Nucl. Mater.*, vol. 12, pp. 84–90, 2017.

[32] T. Hender, R. Fitzpatrick, A. Morris, P. Carolan, R. Durst, T. Edlington, J. Ferreira, S. Fielding, P. Haynes, J. Hugill, I. Jenkins, R. L. Haye, B. Parham, D. Robinson, T. Todd, M. Valovič, and G. Vayakis, "Effect of resonant magnetic perturbations on COMPASS-C tokamak discharges," *Nucl. Fusion*, vol. 32, no. 12, 1992.

[33] T. E. Evans, R. A. Moyer, P. R. Thomas, J. G.Watkins, T. H. Osborne, J. A. Boedo, E. J. Doyle, M. E. Fenstermacher, K. H. Finken, R. J. Groebner, M. Groth, J. H. Harris, R. J. L. Haye, C. J. Lasnier, S. Masuzaki, N. Ohyabu, D. G. Pretty, T. L. Rhodes, H. Reimerdes, D. L. Rudakov, M. J. Schaffer, G.Wang, and L. Zeng, "Suppression of large edge-localized modes in high-confinement DIII-D plasmas with a stochastic magnetic boundary," *Phys. Rev. Lett*, vol. 92, no. 23, 2004.

[34] Y. Liang, H. R. Koslowski, P. R. Thomas, E. Nardon, B. Alper, P. Andrew, Y. Andrew, G. Arnoux, Y. Baranov, M. Bécoulet, M. Beurskens, T. Biewer, M. Bigi, K. Crombe, E. D. L. Luna, P. de Vries, W. Fundamenski, S. Gerasimov, C. Giroud, M. P. Gryaznevich, N. Hawkes, S. Hotchin, D. Howell, S. Jachmich, V. Kiptily, L. Moreira, V. Parail, S. D. Pinches, E. Rachlew, and O. Zimmermann, "Active control of Type-I edge-localized modes with n=1 perturbation fields in the JET tokamak," *Phys. Rev. Lett.*, vol. 98, no. 265004, 2007.

[35] A. Kirk, E. Nardon, R. Akers, M. Bécoulet, G. D. Temmerman, B. Dudson, B. Hnat, Y. Liu, R. Martin, P. Tamain, D. Taylor, and the MAST team, "Resonant magnetic perturbation experiments on MAST using external and internal coils for ELM control," *Nucl. Fusion*, vol. 50, no. 034008, 2010.

[36] W. Suttrop, T. Eich, J. Fuchs, S. Günter, A. Janzer, A. Herrmann, A. Kallenbach, P. Lang, T. Lunt, M. Maraschek, R. McDermott, A. Mlynek, T. Pütterich, M. Rott, T. Vierle, E. Wolfrum, Q. Yu, I. Zammuto, H. Zohm, and the ASDEX Upgrade Team, "First observation of edge localized modes mitigation with resonant and nonresonant magnetic perturbations in ASDEX Upgrade," *Phys. Rev. Lett.*, vol. 106, no. 225004, p. 235003, 2011.

[37] Y. M. Jeon, J.-K. Park, S. Yoon, W. H. Ko, S. G. Lee, K. D. Lee, G. S. Yun, Y. U. Nam, W. C. Kim, J.-G. Kwak, K. S. Lee, H. K. Kim, , and H. L. Yang, "Suppression of edge localized modes in high-confinement KSTAR plasmas by nonaxisymmetric magnetic perturbations," *Phys. Rev. Lett*, vol. 109, no. 3, p. 034004, 2012.

[38] M. Jakubowski, P. Drewelow, S. Masuzaki, K. Tanaka, T. Pedersen, T. Akiyama, S. Bozhenkov, A. Dinklage, M. Kobayashi, Y. Narushima, S. Sakakibara, Y. Suzuki, R. Wolf, H. Yamada, and the LHD Experimental Group, "Influence of the resonant magnetic perturbations on transport in the Large Helical Device," *Nucl. Fusion*, 2013.

[39] N. Leuthold, W. Suttrop, R. Fischer, A. Kappatou, A. Kirk, R. McDermott, A. Mlynek, M. Valovič, M. Willensdorfer, the ASDEX Upgrade Team, and the EUROfusion MST1 Team, "Parameter dependence of ELM loss reduction by magnetic perturbations at low pedestal density and collisionality in ASDEX Upgrade," *Plasma Phys. Control. Fusion*, vol. 59, no. 055004, 2017.

[40] W. Suttrop, M. Rott, T. Vierle, B. Streibl, A. Herrmann, V. Rohde, U. Seidel, D. Yadikin, O. Neubauer, B. Unterberg, E. Gaio, V. Toigo, P. Brunsell, and ASDEX Upgrade Team, "Design of in-vessel saddle coils for MHD control in ASDEX Upgrade," in *35th EPS Conference on Plasma Physics*, vol. 32D, 2008.

[41] W. Suttrop, O. Gruber, S. Günter, D. Hahn, A. Herrmann, M. Rott, T. Vierle, U. Seidel, M. Sempf, B. Streibl, E. Strumberger, D. Yadikin, O. Neubauer, B. Unterberg, E. Gaio, V. Toigo, P. Brunsell, and the ASDEX Upgrade Team, "In-vessel saddle coils for MHD control in ASDEX Upgrade," *Fus. Eng. Design*, vol. 84, pp. 290–294, 2009.

[42] W. Suttrop, L. Barrera, A. Herrmann, R. McDermott, T. Eich, R. Fischer, B. Kurzan, P. Lang, A. Mlynek, T. Pütterich, S. Rathgeber, M. Rott, T. Vierle, E. Viezzer, M. Willensdorfer, E. Wolfrum, I. Zammuto, and the ASDEX Upgrade Team, "Studies of edge localized mode mitigation with new active in-vessel saddle coils in ASDEX Upgrade," *Plasma Phys. Control. Fusion*, vol. 53, no. 124014, 2011.

[43] D. A. Ryan, Y. Q. Liu, A. Kirk, W. Suttrop, B. Dudson, M. Dunne, M. Willensdorfer, the ASDEX Upgrade team, and the EUROfusion MST1 team, "Experimental validation of coil phase parametrisation on ASDEX Upgrade, and extension to iter," *Plasma Phys. Control. Fusion*, vol. 60, no. 065005, 2018.

[44] J. Wesson, *Tokamaks*. Oxford University Press, 1997.

[45] I. H. Hutchinson, *Principles of Plasma Diagnostics*. Cambridge University Press, 2002.

[46] A. Silva, M. E. Manso, L. Cupido, M. Albrecht, F. Serra, P. Varela, J. Santos, S. Vergamota, F. E. bio, J. Fernandes, T. Grossmann, A. Kallenbach, B. Kurzan, C. Loureiro, L. Meneses, I. Nunes, F. Silva, W. Suttrop, , and the ASDEX Upgrade, "Ultrafast broadband frequency modulation of a continuous wave reflectometry system to measure density profiles on ASDEX Upgrade," *Rev. Sci. Instrum.*, vol. 67, no. 12, pp. 4138–14145, 1996.

[47] A. Silva, *The ASDEX Upgrade broadband microwave reflectometry system*. PhD thesis, Instituto Superior Técnico, 2006.

[48] E. Poli, A. Peeters, and G. Pereverzev, "TORBEAM, a beam tracing code for electron-cyclotron waves in tokamak plasmas," *Comp. Phys. Comm.*, vol. 136, p. 9, 2001.

[49] G. D. Conway, J. Schirmer, S. Klenge, W. Suttrop, E. Holzhauer, and the ASDEX Upgrade Team, "Plasma rotation profile measurements using Doppler reflectometry," *Plasma Phys. Control. Fusion*, vol. 56, pp. 951–970, 2004.

[50] E. Viezzer, T. Pütterich, R. Dux, R. M. McDermott, and ASDEX Upgrade Team, "High-resolution charge exchange measurements at ASDEX Upgrade," *Rev. Sci. Instrum.*, vol. 83, no. 103501, 2012.

[51] R. M. McDermott, A. Lebschy, B. Geiger, C. Bruhn, M. Cavedon, M. Dunne, R. Dux, R. Fischer, A. Kappatou, T. Pütterich, E. Viezzer, and ASDEX Upgrade Team, "Extensions to the charge exchange recombination spectroscopy diagnostic suite at ASDEX Upgrade," *Rev. Sci. Instrum.*, vol. 88, no. 073508, 2017.

[52] M. Cavedon, T. Pütterich, E. Viezzer, R. Dux, B. Geiger, R. M. McDermott, H. Meyer, U. Stroth, and ASDEX Upgrade Team, "A fast edge charge exchange recombination spectroscopy system at the ASDEX Upgrade tokamak," *Rev. Sci. Instrum.*, vol. 88, no. 043103, 2017.

[53] J. Schweinzer, E. Wolfrum, F. Aumayr, M. Pöckl, H. Winter, R. P. Schorn, E. Hintz, and A. Unterreiter, "Reconstruction of plasma edge density profiles from li i (2s-2p) emission profiles," *Plasma Phys. Control. Fusion*, vol. 34, no. 7, pp. 1173–1183, 1992.

[54] R. Fischer, E. Wolfrum, J. Schweinzer, and the ASDEX Upgrade Team, "Probabilistic lithium beam data analysis," *Plasma Phys. Control. Fusion*, vol. 50, no. 085009, 2008.

[55] K. McCormick and ASDEX Team, "Measurement of the scrape-off layer density profile on ASDEX via an energetic neutral lithium beam," *Rev. Sci. Instrum.*, vol. 56, no. 5, pp. 1063–1065, 1985.

[56] M. Willensdorfer, E. Wolfrum, R. Fischer, J. Schweinzer, M. Sertoli, B. Sieglin, G. Veres, F. Aumayr, and the ASDEX Upgrade Team, "Improved chopping of a lithium beam for plasma edge diagnostic at ASDEX Upgrade," *Rev. Sci. Instrum.*, 2012.

[57] W. Suttrop and A. G. Peeters, "Practical limits of the ece diagnostics," ipp report, 1997.

[58] B. Kurzan and H. D. Murmann, "Edge and core Thomson scattering systems and their calibration on the ASDEX Upgrade tokamak," *Rev. Sci. Instrum.*, vol. 82, no. 103501, 2011.

[59] A. Mlynek, G. Schramm, H. Eixenberger, G. Sips, K. McCormick, M. Zilker, K. Behler, J. Eheberg, and ASDEX Upgrade Team, "Design of a digital multiradian phase detector and its application in fusion plasma interferometry," *Rev. Sci. Instrum*, vol. 81, no. 033507, 2010.

[60] M. Weinlich and A. Carlson, "Flush mounted Langmuir probes in an oblique magnetic field," *Phys. Plasmas*, vol. 4, no. 2151, 1997.

[61] R. Fischer, C. J. Fuchs, B. Kurzan, W. Suttrop, E. Wolfrum, and ASDEX Upgrade team, "Integrated data analysis of profile diagnostics at ASDEX Upgrade," *Fusion Science and Technology*, vol. 58, pp. 675–684, 2010.

[62] P. J. Mc Carthy, "Analytical solutions to the grad-shafranov equation for tokamak equilibrium with dissimilar source functions," *Phys. Plasmas*, vol. 6, no. 3554, 1999.

[63] E. Strumberger and E. Schwarz, "Vacfield code: Computation of the vacuum magnetic field and its first derivatives for various coil types," tech. rep., Max-Planck-Institut for Plasma Physics (IPP report), 2005.

[64] M. Wade, "Physics and engineering issues associated with edge localized mode control in ITER," *Fusion Engineering and Design*, 2009.

[65] B. Streibl, P. T. Lang, F. Leuterer, J.-M. Noterdaeme, and A. Stäbler, "Machine design, fueling, and heating in asdex upgrade," *Fusion Science and Technology*, vol. 44, pp. 578–592, 2003.

[66] W. Suttrop, L. B. Orte, R. Fischer, J. Fuchs, R. McDermott, H. Müller, T. Pütterich, S. Rathgeber, E. Viezzer, E. Wolfrum, and the ASDEX Upgrade Team, "Access conditions for ELM mitigation with non-axisymmetric magnetic perturbations in ASDEX Upgrade," in *39th EPS Conference & 16th Int. Congress on Plasma Physics*, no. P2.092, 2012.

[67] W. Suttrop, L. B. Orte, T. Eich, R. Fischer, J. Fuchs, L. Giannone, M. Kočan, P. Lang, T. Lunt, M.Maraschek, R. McDermott, H. Müller, T. Pütterich, S. Rathgeber, M. Rott, F. Ryter, T. Vierle, E. Viezzer, E. Wolfrum, and A. U. Team, "Mitigation of edge localised modes with small non-axisymmetric magnetic perturbations in ASDEX Upgrade," in *24th IAEA Fusion Energy Conference*, no. EX/3-4, 2012.

[68] W. Suttrop, L. B. Orte, R. Fischer, J. Fuchs, R. McDermott, A. Mlynek, T.Pütterich, S. Rathgeber, E. Viezzer, E. Wolfrum, and the ASDEX Upgrade Team, "Search for an ELM suppression regime with non-axisymmetric magnetic perturbations at low edge collisionality in ASDEX Upgrade," in *40th EPS Conference on Plasma Physics*, 2013.

[69] W. Suttrop, J. Fuchs, R. Fischer, L. Giannone, A. Herrmann, R. McDermott, M. Maraschek, A. Mlynek, H. Müller, P. Lang, T. Pütterich, M. Rott, T. Vierle, E. Viezzer, E. Wolfrum, and the ASDEX Upgrade Team, "Mitigation of edge localised modes with magnetic perturbations in ASDEX Upgrade," *Fusion Engineering and Design*, vol. 88, pp. 446–453, 2013.

[70] W. Suttrop, A. Kirk, L. B. Orte, M. Cavedon, M. Dunne, R. Fischer, S. Fietz, J. Fuchs, Y. Liu, R. McDermott, D. Ryan, J. Stober, E. Viezzer, M.Willensdorfer, E. Wolfrum, and the ASDEX Upgrade Team, "Studies of magnetic perturbations in high-confinement mode plasmas in ASDEX Upgrade," in *25th IAEA Fusion Energy Conference*, no. EX/P1-23, 2014.

[71] A. Kirk, W. Suttrop, I. Chapman, Y. Liu, R. Scannell, A. Thornton, L. B. Orte, P. Cahyna, T. Eich, R. Fischer, C. Fuchs, C. Ham, J. Harrison, M. Jakubowski, B. Kurzan, S. Pamela, M. Peterka, D. Ryan, S. Saarelma, B. Sieglin, M. Valovic, M. Willensdorfer, MAST, and A. U. Teams, "Effect of resonant magnetic perturbations on low collisionality discharges in MAST and a comparison with ASDEX Upgrade," *Nucl. Fusion*, vol. 55, no. 043011, 2015.

[72] W. Suttrop, A. Kirk, R. Nazikian, N. Leuthold, E. Strumberger, M. Willensdorfer, M. Cavedon, M. Dunne, R. Fischer, S. Fietz, J. Fuchs, Y. Liu, R. McDermott, F. Orain, D. Ryan, E. Viezzer, the ASDEX Upgrade Team, the DIII-D Team, and the Eurofusion MST1 Team, "Experimental studies of high-confinement mode plasma response to non-axisymmetric magnetic perturbations in ASDEX Upgrade," *Plasma Phys. Control. Fusion*, vol. 59, no. 014049, 2017.

[73] T. Evans, M. Fenstermacher, R. Moyer, T. Osborne, J.G.Watkins, P. Gohil, I. Joseph, M. Schaffer, L. Baylor, M. Bécoulet, J. Boedo, K. Burrell, J. deGrassie, K. Finken, T. Jernigan, M. Jakubowski, C. Lasnier, M. Lehnen, A. Leonard, J. Lonnroth, E. Nardon, V. Parail, O. Schmitz, B. Unterberg, and W. West, "RMP ELM suppression in DIII-D plasmas with ITER similar shapes and collisionalities," *Nucl. Fusion*, vol. 48, no. 024002, 2008.

[74] R. A. Moyer, C. Paz-Soldan, R. Nazikian, D. M. Orlov, N. M. Ferraro, B. A. Grierson, M. Knölker, B. C. Lyons, G. R. McKee, T. H. Osborne, T. L. Rhodes, O. Meneghini, S. Smith, T. E. Evans, M. E. Fenstermacher, R. J. Groebner, J. M. Hanson, R. J. L. Haye, T. C. Luce, S. Mordijck, W. M. Solomon, F. Turco, Z. Yan, L. Zeng, and DIII-D Team, "Validation of the model for ELM suppression with 3D magnetic fields using low torque ITER baseline scenario discharges in DIII-D," *Phys. Plasmas*, vol. 24, no. 102501, 2017.

[75] W. Suttrop, A. Kirk, V. Bobkov, M. Cavedon, M. Dunne, R. McDermott, H. Meyer, R. Nazikian, C. Paz-Soldan, D. Ryan, E. Viezzer, M. Willensdorfer, and The ASDEX Upgrade and MST1 Teams, "Experimental conditions to suppress edge localised modes by magnetic perturbations in the ASDEX Upgrade tokamak," *Nucl. Fusion*, vol. 58, no. 096031, 2018.

[76] R. Nazikian, W. Suttrop, A. Kirk, M. Cavedon, T. E. Evans, B. Grierson, A. Hyatt, M. Knolker, Y. Q. Liu, B. Lyons, R. M. McDermott, C. Paz-Soldan, D. Orlov, T. Osborne, D. A. Ryan, E. Viezzer, Z. Wang, M. Willensdorfer, A. Wingen, and the AUG, DIII-D and EUROfusion MST-1 teams, "First observation of ELM suppression by magnetic perturbations in ASDEX Upgrade and comparison to DIII-D matched-shape plasmas," in *26^{th} IAEA Fusion Energy Conference*, no. PD/1-1, 2016.

[77] W. Suttrop, A. Kirk, R. Nazikian, V. Bobkov, M. Cavedon, M. Dunne, N. Leuthold, Y. Q. Liu, R. McDermott, H. Meyer, T. Odstrčil, D. Ryan, M. Valovič, E. Viezzer, M. Willensdorfer, and the ASDEX Upgrade and MST1 Teams, "Full suppression of edge localised modes with non-axisymmetric magnetic perturbations at low plasma edge collisionality in ASDEX Upgrade," in *44^{th} EPS Conference on Plasma Physics*, no. P5.127, 2017.

[78] M. Valovič, P. Lang, A. Kirk, W. Suttrop, M. Cavedon, G. Cseh, M. Dunne, L. Fischer, L. Garzotti, L. Guimarais, G. Kocsis, A. Mlynek, B. Plöckl, R. Scannell, T. Szepesi, G. Tardini, A. Thornton, E. Viezzer, E. Wolfrum, the ASDEX Upgrade Team, and the EUROfusion MST1 Team, "Pellet refuelling of particle loss due to ELM mitigation with RMPs in the ASDEX Upgrade tokamak at low collisionality," *Nucl. Fusion*, vol. 56, no. 066009, 2016.

[79] M. Valovič, P. Lang, A. Kirk, W. Suttrop, M. Cavedon, M. Dunne, R. Fischer, L. Garzotti, L. Guimarais, N. Leuthold, P. McCarthy, H. Meyer, A. Mlynek, B. Plöckl, E. Poli, G. Tardini, E. Viezzer, E. Wolfrum, the ASDEX Upgrade team, and the EUROfusion MST1 team, "Density control by pellets in plasmas with ELM mitigation by RMPs in the ASDEX Upgrade tokamak," *Plasma Phys. Control. Fusion*, 2018.

[80] G. V. Pereverzev and P. N. Yushmanov, "ASTRA: Automated system for transport analysis," tech. rep., Max-Planck-Institut for Plasma Physics (IPP report), 1991.

[81] M. Heyn, I. Ivanov, S. Kasilov, W. Kernbichler, P. Leitner, V. Nemov, W. Suttrop, and the ASDEX Upgrade Team, "Quasilinear modelling of RMP interaction with a tokamak plasma: application to ASDEX Upgrade ELM mitigation experiments," *Nucl. Fusion*, vol. 54, no. 064005, 2014.

[82] M. F. Heyn, I. B. Ivanov, S. V. Kasilov, and W. Kernbichler, "Kinetic modelling of the interaction of rotating magnetic fields with a radially inhomogeneous plasma," *Nucl. Fusion*, vol. 46, pp. 159–169, 2006.

[83] M. F. Heyn, I. B. Ivanov, S. V. Kasilov, W. Kernbichler, I. Joseph, R. A. Moyer, and A. M. Runov, "Kinetic estimate of the shielding of resonant magnetic field perturbations by the plasma in DIII-D," *Nucl. Fusion*, vol. 48, no. 024005, 2008.

[84] M. Becoulet, P. M. F. Orain and, N. Mellet, X. Garbet, E. Nardon, G. Huysmans, T. Casper, A. Loarte, P. Cahyna, A. Smolyakov, F. Waelbroeck, M. Schaffer, T. Evans, Y. Liang, O. Schmitz, M. Beurskens, V. Rozhansky, and E. Kaveeva, "Screening of resonant magnetic perturbations by flows in tokamaks," *Nucl. Fusion*, vol. 52, no. 054003, 2012.

[85] M. Willensdorfer, T. B. Cote, C. C. Hegna, W. Suttrop, H. Zohm, M. Dunne, E. Strumberger, G. Birkenmeier, S. S. Denk, F. Mink, B. Vanovac, L. C. Luhmann, and the ASDEX Upgrade Team, "Field-line localized destabilization of ballooning modes in three-dimensional tokamaks," *Phys. Rev. Lett.*, vol. 119, no. 085002, 2017.

[86] T. Cote, C. Hegna, M. Willensdorfer, E. Strumberger, W. Suttrop, H. Zohm, and the ASDEX Upgrade team, "Helically localized ballooning instabilities in three-dimensional tokamak pedestals," *Nucl. Fusion*, vol. 69, no. 016015, 2018.

[87] M. Willensdorfer, E. S. S S Denk and, W. Suttrop, B. Vanovac, I. C. D Brida and, M Cavedon and, M. Dunne, S. Fietz, R. Fischer, A. Kirk, F. M. Laggner, Y. Q. Liu, T. Odstrčil, D. A. Ryan, E. Viezzer, H. Zohm, I. C. Luhmann, The ASDEX Upgrade Team, and The EUROfusion MST1 Team, "Plasma response measurements of external magnetic perturbations using electron cyclotron emission and comparisons to 3D ideal MHD equilibrium," *Plasma Phys. Control. Fusion*, vol. 58, no. 114004, 2016.

[88] M. Willensdorfer, E. Strumberger, W. Suttrop, M. Dunne, R. Fischer, G. Birkenmeier, D. Brida, M. Cavedon, S. Denk, V. Igochine, L. Giannone, A. Kirk, J. Kirschner, A. Medvedeva, T. Odstrčil, D. Ryan, The ASDEX Upgrade Team, and The EUROfusion MST1 Team, "Three dimensional boundary displacement due to stable ideal kink modes excited by external n = 2 magnetic perturbations," *Nucl. Fusion*, vol. 57, no. 116047, 2017.

[89] G. McKee, Z. Yan, C. Holland, R. Buttery, T. Evans, R. Moyer, S. Mordijck, R. Nazikian, T. Rhodes, O. Schmitz, and M. Wade, "Increase of turbulence and

transport with resonant magnetic perturbations in elm-suppressed plasmas on DIII-D," *Nucl. Fusion*, vol. 53, no. 113011, 2013.

[90] R. S. Wilcox, T. L. Rhodes, M. W. Shafer, L. E. Sugiyama, N. M. Ferraro, B. C. Lyons, G. R. McKee, C. Paz-Soldan, A. Wingen, and L. Zeng, "Helical variation of density profiles and fluctuations in the tokamak pedestal with applied 3D fields and implications for confinement," *Phys. Plasmas*, vol. 25, no. 056108, 2018.

[91] T. Zhang, H. Q. Liu, H. M. Xiang, Y. M. Wang, Y. Sun, K. N. Geng, F. Wen, G. S. Li, K. X. Ye, M. F. Wu, F. B. Zhong, J. Huang, S. B. Zhang, X. Gao, and EAST Team, "Poloidally localized edge density fluctuation with applied and spontaneous 3-d fields in experimental advanced superconducting tokamak (EAST)," *Phys. Plasmas*, vol. 26, no. 092504, 2019.

[92] G. H. Hu, R. Chen, G. S. Xu, H. Y. Guo, Y. W. Sun, Y. F. Liang, J. L. Xie, C. Zhou, X. L. Jin, S. Gu, M. N. Jia, Y. F. Wang, L. Wang, J. C. Xu, Q. Q. Yang, S. C. Liu, X. Q. Wu, T. Zhang, Q. Zang, L. Chen, N. Yan, L. M. Shao, Y. Ye, S. Y. Ding, B. N. Wan, and EAST Team, "Non-axisymmetric E×B shear inducing toroidally localized turbulence with applied magnetic perturbation field in EAST," *Nucl. Fusion*, vol. accepted, 2019.

[93] B. LaBombard, R. L. Boivin, M. Greenwald, J. Hughes, B. Lipschultz, D. Mossessian, C. S. Pitcher, J. L. Terry, S. J. Zweben, and A. Group, "Particle transport in the scrape-off layer and its relationship to discharge density limit in Alcator C-Mod," *Phys. Plasmas*, vol. 8, no. 2107, 2001.

[94] D. A. D'Ippolito, J. R. Myra, , and S. I. Krasheninnikov, "Cross-field blob transport in tokamak scrape-off-layer plasmas," *Phys. Plasmas*, vol. 9, no. 222, 2002.

[95] O. E. Garcia, N. H. Bian, and W. Fundamenski, "Radial interchange motions of plasma filaments," *Phys. Plasmas*, vol. 13, no. 082309, 2006.

[96] B. Lipschultz, X. Bonnin, G. Counsell, A. Kallenbach, A. Kukushkin, K. Krieger, A. Leonard, A. Loarte, R. Neu, R. Pitts, T. Rognlien, J. Roth, C. Skinner, J. Terry, E. Tsitrone, D. Whyte, S. Zweben, N. Asakura, D. Coster, R. Doerner, R. Dux, G. Federici, M. Fenstermacher, W. Fundamenski, P. Ghendrih, A. Herrmann, J. Huv, S. Krasheninnikov, G. Kirnev, A. Kreter, V. Kurnaev, B. LaBombard, S. Lisgo, T. Nakano, N. Ohno, H. Pacher, J. Paley, Y. Pan, G. Pautasso, V. Philipps, V. Rohde, D. Rudakov, P. Stangeby, S. Takamura, T. Tanabe, Y. Yang, and S. Zhu, "Plasma–surface interaction, scrape-off layer and divertor physics: implications for iter," *Nucl. Fusion*, vol. 47, no. 9, 2007.

[97] D. Carralero, G. Birkenmeier, H. Müller, P. Manz, P. deMarne, S. Müller, F. Reimold, U. Stroth, M. Wischmeier, E. Wolfrum, and The ASDEX Upgrade Team, "An experimental investigation of the high density transition of the scrape-off layer transport in ASDEX Upgrade," *Nucl. Fusion*, vol. 54, no. 123005, 2014.

[98] D. Carralero, M. Siccinio, M. Komm, S. Artene, F. D'Isa, J. Adamek, L. Aho-Mantila, G. Birkenmeier, M. Brix, G. Fuchert, M. Groth, T. Lunt, P. Manz, J. Madsen, S. Marsen, H. Müller, U. Stroth, H. Sun, N. Vianello, M. Wischmeier, E. Wolfrum, ASDEX Upgrade Team, COMPASS Team, JET Contributors, and The EUROfusion MST Team, "Recent progress towards a quantitative description of filamentary SOL transport," *Nucl. Fusion*, vol. 57, no. 056044, 2017.

[99] D. A. D'Ippolito, J. R. Myra, and S. J. Zweben, "Convective transport by intermittent blob-filaments: Comparison of theory and experiment," *Phys. Plasmas*, vol. 18, no. 060501, 2011.

[100] T. S. Hahm and K. H. Burrell, "Flow shear induced fluctuation suppression in finite aspect ratio shaped tokamak plasma," *Phys. Plasmas*, vol. 2, no. 5, 1995.

[101] P. Manz, J. E. Boom, E. Wolfrum, G. Birkenmeier, I. G. J. Classen, N. C. L. Jr, U. Stroth, , and the ASDEX Upgrade Team, "Velocimetry analysis of type-I edge localized mode precursors in ASDEX Upgrade," *Plasma Phys. Control. Fusion*, vol. 56, no. 035010, 2014.

[102] M. Kotschenreuther, X. Liu, D. Hatch, S. Mahajan, L. Zheng, A. Diallo, R. Groebner, the DIII-D TEAM, J. Hillesheim, C. Maggi, C. Giroud, F. Koechl, V. Parail, S. Saarelma, E. Solano, A. Chankin, and JET Contributors, "Gyrokinetic analysis and simulation of pedestals to identify the culprits for energy losses using 'fingerprints'," *Nucl. Fusion*, vol. 59, no. 096001, 2019.

[103] T. Weyens, R. Sánchez, G. Huijsmans, A. Loarte, and L. García, "PB3D: a new code for edge 3-d ideal linear peeling-ballooning stability," *J. Comput. Phys.*, vol. 330, pp. 997–1009, 2017.

[104] M. Maurer, A. Bañón Navarro, T. Dannert, M. Restelli, F. Hindenlang, T. Görler, D. Told, D. Jarema, G. Merlo, and F. J. and, "GENE-3D: a global gyrokinetic turbulence code for stellarators," submitted to *J. Comput. Phys.*, 2020.

[105] A. Ivanov, R. Khayrutdinov, S. Medvedev, and Y. Poshekhonov, "New adaptive grid plasma evolution code SPIDER," in *32nd EPS Conference on Plasma Physics*, no. P5.063, 2005.

[106] E. Fable, C. Angioni, F. J. Casson, D. Told, A. A. Ivanov, F. Jenko, R. M. McDermott, S. Y. Medvedev, G. V. Pereverzev, F. Ryter, W. Treutterer, E. Viezzer, and the ASDEX Upgrade Team, "Novel free-boundary equilibrium and transport solver with theory-based models and its validation against ASDEX Upgrade current ramp scenarios," *Plasma Phys. Control. Fusion*, vol. 55, no. 124028, 2013.

Acknowledgment

First of all I would like to thank the whole ASDEX Upgrade team, which assured that ASDEX Upgrade ran smoothly even at times when the machine was a bit petulant.

I want to thank my academic supervisor Hartmut Zohm not only for giving me the opportunity to work on this thesis, but also for his valuable input and patience.

I would like to particularly thank my direct supervisor Wolfgang Suttrop. His lectures at the University of Bayreuth sparked my interest and enthusiasm for nuclear fusion. This lead to my master thesis at the IPP and, finally, this PhD thesis. Throughout all this time he supported me with help and advice, for which I am very thankful. Also in times when I was struggling with something or was progressing only slowly, he stayed patient and was never bugged when he had to explain things twice. Without him this thesis would not have been possible.

Furthermore, I want to thank Matthias Willensdorfer for his help and advice throughout the years.

During the PhD thesis I met only nice colleagues, which made the work at IPP a pleasure. Since it would be embarrassing for me to forget to name someone, I would like to thank everyone I met at IPP and spent time with.

Last but not least I would like to thank my family for their endless support and paving the way for my studies.